Anatomic Dead Space Washout and Flow Effects during Breathing with Nasal High Flow Therapy

A thesis submitted in partial fulfilment of the requirements for the
Degree of Master of Engineering in Mechanical Engineering
at the University of Canterbury

Karla M. Dey
University of Canterbury
2014

Acknowledgements

Firstly, I would like express my gratitude to the numerous people whose insight, help and support have aided me throughout this research.

Foremost I would like to thank my supervisor Dr Mark Jermy and mentor Dr Callum Spence with whom I have had the great privilege of working throughout this research. For their constant support and advice I am truly grateful as without it this research would not have been possible.

Special thanks to the mechanical engineering department, in particular the assistance given by Eric Cox, Gerry Kirk, Dr Patrick Geoghegan, Julian Phillips and Graeme Harris. Thanks also to the Final Year Project and summer students who have worked alongside and aided me. To Fisher & Paykel Healthcare Ltd for their kind and valuable support.

For the funding provided by Fisher & Paykel Healthcare Ltd and the Ministry of Science and Innovation through which I was able to pursue this endeavour to higher education.

To my family and friends I give my sincerest thanks. To my parents, for their unwavering confidence in me and encouragement in all my endeavours. You instilled in me an appreciation for knowledge and taught me the means to attain it, for which I am truly grateful.

Finally, to Hamish I give my most heartfelt gratitude. For supporting and motivating me throughout this journey so that we may embark upon a greater future together.

Abstract

Nasal high flow (NHF) therapy is a recent form of non-invasive respiratory support for patients suffering from respiratory distress that supplies high flows of heated and humidified air, oxygen or a mix via a nasal cannula. A number of in vivo studies have proven its effectiveness at improving blood oxygenation; however, its mechanisms of action remain widely unproven. Two proposed mechanisms of action, the CO_2 washout of anatomic dead space and the production of positive airway pressure, are investigated in this thesis for the use of the Fisher & Paykel Healthcare Ltd (FPH) Optiflow™ adult nasal cannula through a range of experiments.

Five anatomically correct upper airway models produced from computed tomography (CT) scan data via 3D printing were employed during in vitro experiments and two live subjects participated in in vivo measurements. The human respiratory system was faithfully replicated for CO_2 washout experiments with physiological CO_2 diffusion into the lung replicated by a constant flow of CO_2 into the lung pump. In vivo measurement of a natural breathing flow pattern was scaled to an average population tidal volume and respiratory rate for in vitro use.

In vitro measurements of static pressure during natural breathing found similar flow resistances across the nasal passage for inspiratory and expiratory flow directions; however, across the entire upper airway greater resistance was seen for inspiration. Introduction of NHF therapy produced significant increases in all mean and peak airway pressures within the upper airway with a flow rate of 30 LPM fulfilling the inspiratory work requirements presented by the upper airway resistance.

In vivo and in vitro hot wire anemometry measurements at the exterior nares indicated low velocity and turbulence intensity flows at peak inspiration and a high velocity jet with high turbulence during peak expiration. At natural breathing an in vitro anterior-posterior velopharynx traverse captured low turbulence intensities during peak inspiration and high turbulence intensities during peak expiration. Introduction of NHF therapy had little influence on the turbulence intensity profile of peak expiration yet did cause significant increases in the turbulence intensities during peak inspiration.

Measurements of the CO_2 concentration near the lung volume over many breath cycles were used to find time-averaged CO_2 concentrations. For the standard airway model an average CO_2 concentration of 4.88 ± 0.07 %V/V was determined during natural breathing. Implementation of increasing levels of NHF therapy generated significant washout of CO_2 reducing this average concentration to a minimum of 3.81 ± 0.11 %V/V at a flow rate of 80 LPM. It was determined that airway geometry significantly affected the efficacy of the NHF therapy though CO_2 washout was observed in all five airway models.

Table of Contents

Table of Figures

Table of Tables

1 Introduction

Nasal high flow (NHF) is a relatively new therapy employed by clinicians to aid patients suffering from mild to moderate respiratory distress as an alternative to face mask oxygen therapy and other non-invasive therapies. NHF describes the method of supplying high flows of warmed and humidified air, oxygen or an air-oxygen mix to a patient via a nasal cannula as a means of increasing the fraction of oxygen in the inspired gas (FiO_2) and subsequently the oxygen saturation of the patient's blood. The Optiflow™ nasal cannula is designed specifically for the delivery of NHF therapy by Fisher & Paykel Healthcare Ltd (FPH).

1.1 NHF Therapy Mechanisms of Action

Most previous research into the use of NHF therapy has been focused on monitoring patient outcomes during therapy and comparing these to the outcomes from more established therapies such as high flow face mask oxygen therapy. NHF has been demonstrated to improve blood oxygenation in critical care patients (Chatila et al., 2004, Nicolet et al., 2011, Parke et al., 2011b, Rello et al., 2012, Sztrymf et al., 2011, Tiruvoipati et al., 2010) but as it is still a relatively new therapy the means by which it does so are still uncertain. It has been proposed by Dysart et al. (2009) that there are five major mechanisms of action which make NHF an effective therapy. These five mechanisms are described as:

1. Nasopharyngeal dead space washout due to flushing effect of high flow;
2. Work of breathing reduction during inspiration due to positive flow pressure;
3. Improved pulmonary conductance due to warmed and humidified air being supplied in comparison to the cold, dry air used in other therapies;
4. Reduced metabolic effort due to warmed and humidified air supplied;
5. Improved lung recruitment due to positive pressure provided by high flow.

Investigation of the first two of these mechanisms is undertaken in this research.

1.2 Optiflow™ Nasal Cannula

The Optiflow™ nasal cannula is manufactured by Fisher & Paykel Healthcare Ltd, Auckland, New Zealand, and was first introduced to the market in 2006. It is available in three different sizes to suit a range of adults. Many factors of the original Optiflow™ Nasal cannula design were chosen to

optimise patient comfort rather than therapy efficacy and since its release the design has not been altered. The Optiflow™ nasal cannula is recommended for delivery of NHF therapy flow rates from 10 to 60 LPM.

1.3 Research Objectives

This research focused predominantly on confirming the first mechanism of action proposed by Dysart et al. (2009), nasopharyngeal dead space washout, but was expanded to include washout of the entire anatomic dead space. To this effect the primary objective of this study was to quantify the level of CO_2 washout achieved by the current Optiflow™ nasal cannula design for a number of NHF flow rates through in vitro experimentation. In addition, the influence of variations in upper airway geometry on the therapy efficacy was examined. Local static pressure, velocity and turbulence effects within the upper airway are also investigated to compliment the washout investigations as well as feeding into knowledge for the second mechanism.

1.4 Thesis Structure

This thesis encompasses the development of experimental methods and systems through to the experimental results and implications and is structured as follows. Chapter 2 provides background on the respiratory system anatomy and physiology, the use of NHF therapy and the Optiflow™ nasal cannula to provide respiratory support and the theories supporting the first of the two proposed mechanisms of action. A review of the current literature related to the objectives of this study is given in Chapter 3. Chapters 4, 5 and 6 detail the development and evolution of the upper airway models, experimental systems and breath patterns employed in the various experiments throughout this research. Chapters 7, 8 and 9 are dedicated to the three major areas experimentally examined; that is the upper airway static pressures, upper airway velocities and turbulence intensities, and anatomic dead space washout; with each containing the experimental methods, results, analyses and implications. A final chapter 10 details the key research conclusions and suggestions for future work.

2 Background Theory

2.1 Anatomy of the Respiratory System

In human anatomy specific terms are used to describe locations and directions without reference to the body's orientation in space; that is, independent of whether the person is standing, sitting or lying, and independent of which way they are facing. A brief description, with reference to the illustration of Figure 1, of these definitions is necessary so that some of the terms used in this research can be understood. Firstly, from a person's centre, the direction toward their front is referred to as anterior while posterior describes the opposite direction, toward the persons back. A plane which intersects the person normal to a line running anterior to posterior is referred to as a coronal or frontal plane. Again from the persons centre, the direction toward the head is superior and the direction toward the feet is inferior. A plane intersecting the person normal to a line running superior to inferior is known as a transverse plane. A line drawn down the centre of a person's front from head to toe is known as the midline. As either side of the midline is almost a mirror image the other, slightly different directional terms are used for this third axis. Toward the midline is considered medial, whilst the directions away from the midline are lateral. A plane intersecting a person normal to medial-lateral axis is known as a sagittal plane. A sagittal plane which runs directly through the midline of a person is considered a midsagittal plane.

The respiratory system as illustrated in Figure 2 is comprised of two major regions, designated as the conducting airways and the respiratory zone. The conducting airways are all regions of the airway from the nostrils down to the terminal bronchioles. These conducting airways serve the purpose of filtering, heating and humidifying the inspired air and directing it into the respiratory zone within the lungs. The respiratory zone is comprised of the respiratory bronchioles, alveolar ducts, alveolar sacs and the alveoli. It is within the respiratory zone that the process of pulmonary respiration occurs, that is the gas exchange of oxygen into and carbon dioxide out of the blood passing through the pulmonary capillaries.

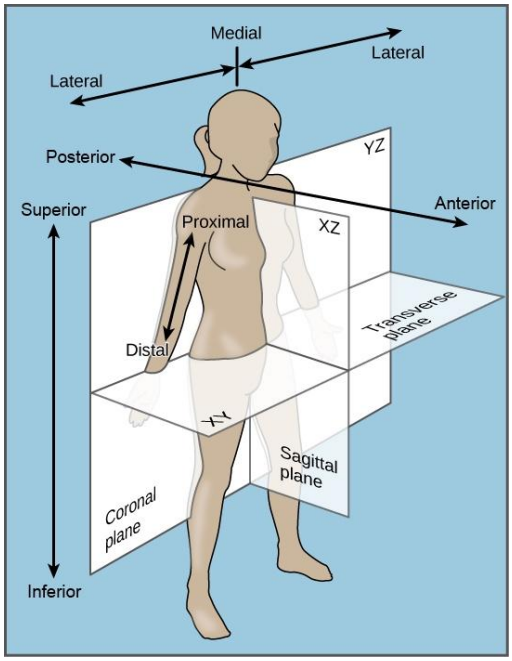

Figure 1: Illustration of the anatomical planes and directions employed (adapted from cnx.org).

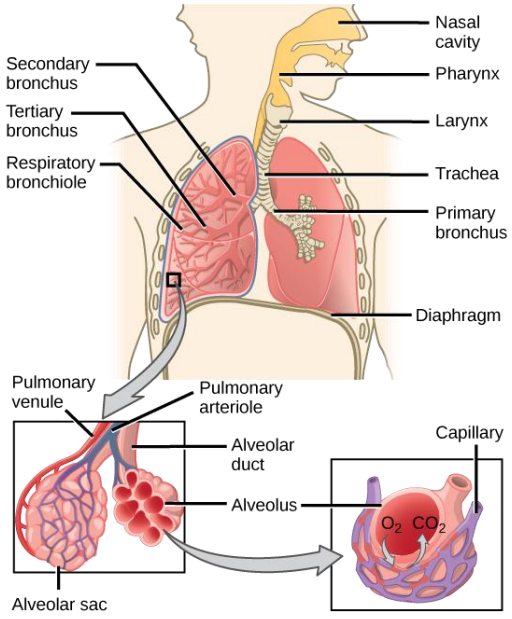

Figure 2: Illustration of the human respiratory system identifying major features (adapted from cnx.org).

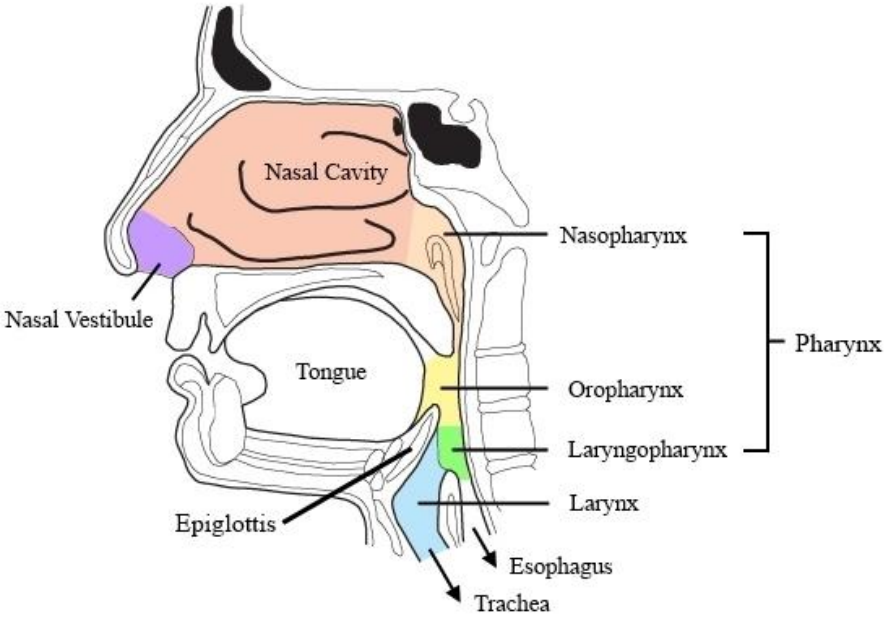

Figure 3: Illustration of the regions of the upper airway (adapted from www.gru.edu).

The upper region of the conducting airways is a combination of complex structures which include the nasal vestibules, nasal cavity, nasopharynx, oropharynx and laryngopharynx as shown in Figure 3. The nose is a cartilaginous structure which forms the entrance to the upper airways via the nostrils, or nares. Within each side of the nose there is a small volume known as the nasal vestibule, each of which are lined with fine hairs, vibrissae, which aid in filtering inspired air. At their posterior, the passage through each nasal vestibule contracts to a minimum cross section known as the nasal valve, followed by a sudden expansion into the nasal cavity. The nasal cavity is separated into right and left sides by the nasal septum. The nasal septum is composed of both cartilage and bone, beginning within the nose and extending to just anterior of the nasopharynx. Each left and right volume of the nasal cavity is divided into superior, middle and inferior regions known as meatuses by three bone structures, the turbinates or conchae. These three turbinates are, like the meatuses, referred to as superior, middle and inferior and protrude from the lateral nasal cavity walls, stopping short of the nasal septum. The turbinates, which increase the internal surface area of the nasal cavity, are covered in a highly vascularised, thin mucous membrane which serves to heat and humidify air on inspiration and recover heat and humidity from the air on expiration (Elad et al., 2008, Ritter, 1970). A cross section of the left and right nasal cavities, showing the turbinates and meatuses is given in Figure 4. The upper most surface of each nasal cavity side contains the olfactory receptors, the structures responsible for sensing smell, within the olfactory region.

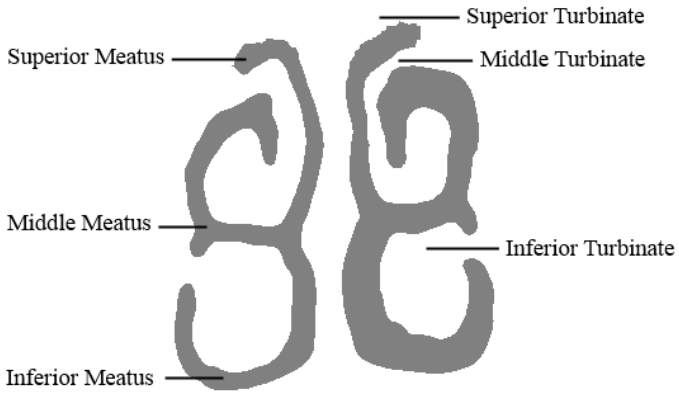

Figure 4: Cross section of airway 06B left and right nasal cavities.

The nasopharynx is the first and most superior of the four sections which constitute the pharynx as shown in Figure 3. The nasopharynx connects to the posterior of the nasal cavity and extends down to the most inferior location of the uvula, or soft palate. A transition from the nasopharynx into the oropharynx occurs at this location of the soft palate, a region referred to as the velopharynx. The velopharynx is significant as, aside from the nasal valves, it is the point in the upper airway with the smallest cross-sectional area (hence the region of highest velocity in the pharynx during mouth-closed breathing). The oropharynx continues down until the epiglottis is reached. The oral cavity connects to the anterior of the oropharynx; however, during nasal breathing the oral cavity is most often cut off from the pharynx as the tongue rests against the palate, isolating it from the rest of the upper airway (Lumb, 2010). At the epiglottis the oropharynx merges into the laryngopharynx, the third and most inferior of the three pharynx regions. The laryngopharynx is the most inferior region of the airway which also acts as a digestive pathway, with the oesophagus and larynx both branching off at its most inferior opening. It is at this point of bifurcation that the epiglottis has an active role, moving down to close off the larynx from the laryngopharynx during the act of swallowing to prevent the entry of any food or liquids into the lungs. In its natural position the epiglottis is orientated in an superior direction, lying close to the posterior of the tongue, but on swallowing the pharynx moves upwards and the epiglottis downwards to occlude the entrance to the larynx. The larynx connects the laryngopharynx with the trachea and is the region of voice production, containing the vocal chords. The trachea is a long, circular passage with a diameter of approximately 25 mm which runs along the anterior of the neck and into the thoracic cavity where it bifurcates into the left and right bronchi at a position just below the top of the two lungs. These bronchi then enter into the respective left and right lungs and further branch into secondary and tertiary bronchi, bronchioles and terminal bronchioles, providing passageways to all areas of the lungs. The many branches from the bronchi to the terminal bronchioles are collectively known as the bronchial tree. It is after the terminal bronchioles that the volumes become active, with respiration occurring within the many alveoli. Respiratory gases fill the alveoli which are surrounded by pulmonary capillaries on the other side of the alveolar walls. Where the wall

of a capillary meets an alveolar wall a respiratory membrane is formed. It is across this membrane that the exchange of oxygen into and carbon dioxide out of the pulmonary blood occurs. This process is driven by partial pressure gradients across the membrane which induce passive diffusion of the two gasses.

2.2 Respiratory Physiology

Respiratory ventilation is the process of gas exchange into and out of the lungs, facilitated by the act of breathing. The breathing response can be controlled either consciously or subconsciously, the latter of which is the primary mechanism. There are two parts to a breath cycle, the active inspiration and the passive expiration. During inspiration the contraction of the diaphragm muscle and other thoracic muscles causes an increase in the volume of the thoracic cavity. This results in a pressure decrease within the lungs and an influx of air through the airways to equalise the pressure between the lungs and the external environment. On expiration these muscles relax and the lungs shrink back to their original volume, expelling the inspired volume of air. The contraction of muscles during inspiration requires physical effort which contributes to the work of breathing; however, this effort is stored in the elastic muscles and on expiration is released to return the lungs to their original condition. The conducting airways also contribute to the work of breathing as wall friction causes a resistance to flow which results in viscous pressure losses along its length in both inspiratory and expiratory flow directions. Expiration can also be forced with the active use of abdominal and internal intercostal muscles when the resistance to flow is too high to be overcome by the elastic forces.

The volume of air exchanged within a breath cycle is known as the tidal volume, and the frequency of breaths is the respiratory rate measured in breaths per minute. The minute volume or minute ventilation is the volume of air exchanged by the lungs within a minute and is the product of the tidal volume and respiratory rate. Average adult tidal volume and respiratory rate are often stated as 500 ml and 12 breaths per minute respectively, equating to a minute volume of 6 litres per minute (Tortora and Derrickson, 2006, Widmaier et al., 2011). Even at the end of expiration the lungs retain some residual volume of gas to maintain patency of the lung structures allowing continuous gas exchange. The volume of air which remains in the lungs at the transition between expiration and inspiration is the functional residual capacity (FRC) which, for an average adult, has a value of 2.4 litres(Tortora and Derrickson, 2006). This volume can be further divided into two more which are the expiratory reserve volume, the maximum volume that can be forcefully expired, and the residual volume, what remains of the FRC following a forced expiration. The inspiratory capacity is the maximum volume in excess of the FRC that can be inspired and is the sum of the tidal volume and the inspiratory reserve. The vital capacity of the lungs is the total volume of air that can be exchanged when inhaling the

maximum amount after a forced expiration. When this is summed with the residual volume you have the total lung capacity. Figure 5 provides an overview of all lung volumes and capacities.

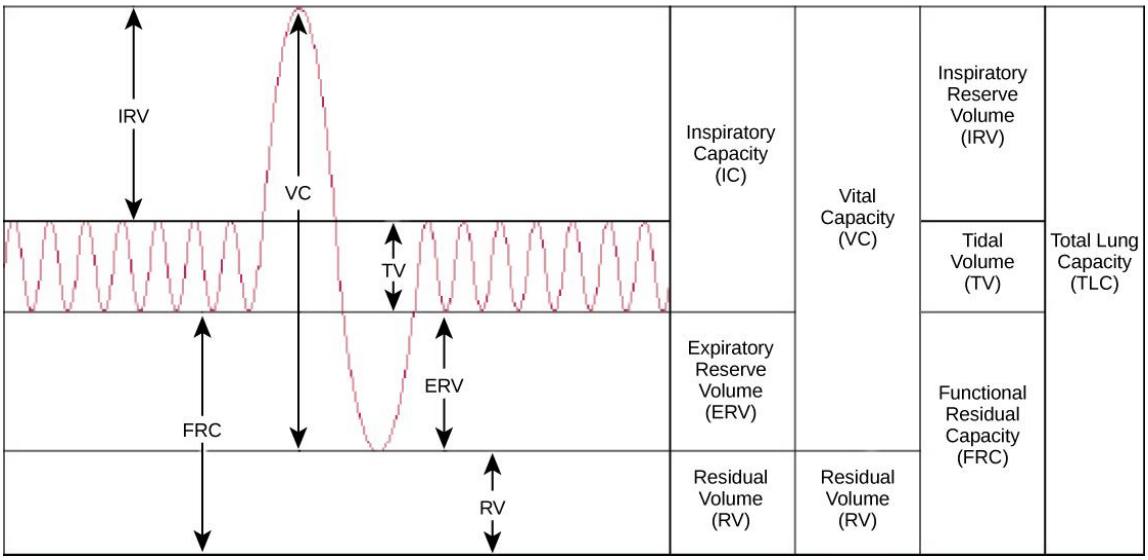

Figure 5: Illustration of lung volumes and capacities (adapted from cnx.org).

As pulmonary respiration only occurs within the respiratory zone, the volume of air contained within the conducting airways does not participate in the gas exchange process. The conducting airways can therefore also be referred as the anatomic dead space, a volume which at the end of expiration contains lung gases high in CO_2 and at the end of inspiration contains fresh air. Because the dead space is filled with these high CO_2 concentration gases at the end of expiration, this volume is re-breathed into the lungs at the beginning of the subsequent inspiration and the same volume of fresh air remains in the dead space at its conclusion, not reaching the lungs. This means that the tidal volume drawn into the lungs is comprised of both expiratory gases and fresh air. The rate at which fresh air is delivered to the respiratory zone is referred to as the alveolar ventilation which, though similar to the minute ventilation, subtracts the dead space volume from the tidal volume prior to multiplication with the respiratory rate. When a person is suffering from respiratory distress, their tidal volume often decreases. To account for this decrease in tidal volume, the respiratory rate must increase so that equilibrium of pulmonary respiration can be maintained within the lungs. Because of the expiratory gas retention within the dead space the respiratory rate must increase so that the minute volume is actually larger than it would be during normal breathing, as a larger percentage of each breath is made up of the re-breathed dead space gases. To obtain this higher minute volume requires extra metabolic effort which in turn can be detrimental to the health and recovery of the sufferer. The use of NHF therapy is aimed to reduce stress on the respiratory system by introducing a continuous high flow of heated and humidified air, oxygen or a mix of the two into the airway through the nares.

2.3 Nasal High Flow Therapy and the Optiflow™ Nasal Cannula

NHF therapy is a relatively new breathing therapy with the first adult NHF cannulae introduced in 2000 (Ward, 2013). Since introduction, NHF has proven to be an effective method of delivering oxygen to critical care patients and improving blood oxygen saturation (Chatila et al., 2004, Nicolet et al., 2011, Parke et al., 2011b, Rello et al., 2012, Sztrymf et al., 2011, Tiruvoipati et al., 2010). NHF therapy has also been shown to provide improved patient comfort when compared to full face mask therapy methods, which in turn promotes better patient compliance to the therapy regime (Nicolet et al., 2011, Spentzas et al., 2009, Tiruvoipati et al., 2010). The Optiflow™ nasal cannula is designed and manufactured by FPH specifically for delivery of NHF therapy.

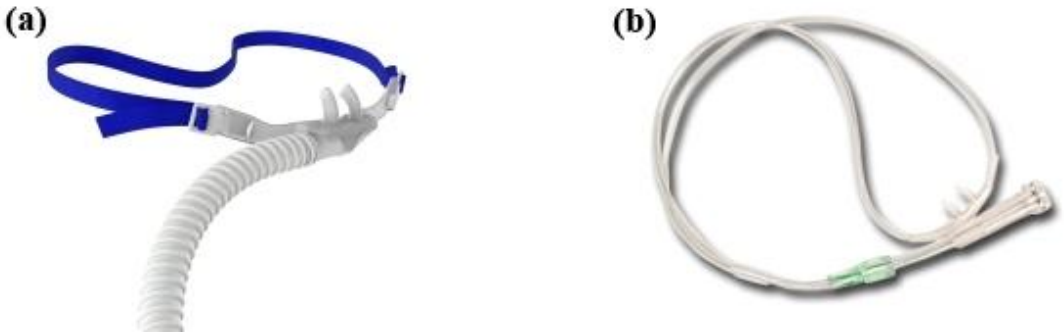

Figure 6:Comparison of the cannula design differences between the (a) FPH Optiflow™ nasal cannula; and (b) Vapotherm High Flow Therapy Interface (adapted from www.vtherm.com).

NHF therapy is the name used to describe the delivery of high flows of either air, oxygen or an air-oxygen mix into the airway via a nasal cannula. Therapy delivery via a nasal cannula provides greater comfort and freedom to the wearer in comparison to mask administered therapies as it allows them to move, talk, eat and drink without disturbing the interface. While most other cannulae have a basic form similar to low flow nasal cannulae the Optiflow™ nasal cannula is uniquely designed to maximise patient comfort. The soft, flexible Optiflow™ cannula manifold is made to rest on the patient's upper lip with the prongs extending into the nasal vestibules and is secured in place by an over-the-ears elastic band. The flow is delivered to the cannula via a single flexible tube as depicted in Figure 6 (a). A competitor's product, designed to be worn with the flow delivery tubes passing over the ears for cannula location, is pictured in Figure 6 (b). The Optiflow™ cannula is currently used to deliver therapy flows ranging from 10 to 60 litres per minute, well above the minute volume of the average person of approximately 6 litres per minute (Tortora and Derrickson, 2006). Before the flow is delivered to the patient, it is heated to an optimal temperature of 37°C and humidified to 100% relative humidity (44 mg/l). This pre-conditioning is advantageous as gases entering the respiratory system must be heated and humidified in the upper airway to prevent dehydration of the lungs and airways. If the additional air provided at these high flow rates is not preconditioned, the upper airway

is unable to condition it adequately and the airways quickly become stripped of moisture causing the wearer great discomfort and, if used for long periods, damage to the airway tissues.

Mechanisms of Action

The mechanisms by which NHF therapy is able to effectively improve blood oxygenation are still relatively un-researched, though five main mechanisms of action have been put forward by Dysart et al. (2009) as previously stated. The first of these two proposed mechanism, dead space washout of CO_2 and reduction of inspiratory work due to generation of positive airway pressure (PAP), have been investigated through this research and their theories are further explained below.

The first of the five mechanisms is the washout of CO_2 from the anatomic dead space. Dysart et al. (2009) proposed that the introduction of high flow rates of air into the airway via NHF produces a continuous flushing effect, forcing respiratory gases high in CO_2 out of the airway. The flushed volumes would then be filled with the NHF gases which have very low CO_2 concentrations and, in the case of delivery of oxygen or an air-oxygen mix, a high concentration of O_2. This could effectively be considered to constitute a reduction in the dead space volume, as a portion of the volume which would be filled with high CO_2 gases during expiration while breathing naturally is instead flushed out and filled with NHF gases. Subsequently, when NHF therapy is in use the NHF gases (air, pure oxygen or an air-oxygen mix) are nearer the lungs at the beginning of each inspiratory breath and therefore represent a higher percentage of the tidal volume. For patients suffering from respiratory distress while breathing unassisted, implementation of this therapy is believed to aid in increasing the respiratory ventilation and thus blood oxygenation. This is thought to lead to beneficial reductions in both the respiratory rate and stress on the respiratory system, supporting patient recovery.

The second mechanism of action proposed by Dysart et al. (2009) is the generation of PAP leading to a reduction in inspiratory work. The generation of PAP is the basis of another non-invasive ventilation therapy known as continuous positive airway pressure (CPAP). PAP is generated with CPAP by supplying high pressure flows to the airways via a sealed mask. By providing PAP the physical effort required to overcome the airway resistance during inspiration is reduced, lung recruitment is improved and the risk of airway collapse decreased. Dysart et al. (2009) suggests that NHF therapy also generates some level of PAP, thus providing the user with beneficial pressure effects similar to those experienced during CPAP.

3 Literature Review

This chapter provides a review of literature in the field of in vivo, in vitro and computational fluid dynamics (CFD) studies of flows within nasal passage and upper airway geometries as relates to the objectives of the current research. It is structured in the same manner as the rest of this thesis such that the methods of modelling the airway geometry and defining and delivering the flows are first reviewed; followed by consecutive examinations of the in vivo, in vitro and CFD studies carried out for upper airway pressures, upper airway flow patterns and turbulence, and the use of NHF therapy and CO_2 washout of anatomic dead space.

3.1 Nasal Cavity and Airway Modelling for In Vitro and CFD Studies

In the many previous in vitro and CFD studies of flows within the nasal cavity and upper airways numerous approaches have been taken to produce or define the desired flow domain. In the case of in vitro experiments replication of a physiologically accurate nasal cavity or upper airway is challenging and is often accomplished by first extracting the desired geometry from MRI (Grgic et al., 2004, Häußermann et al., 2002, Schreck et al., 1993) or CT (Doorly et al., 2008a, Grgic et al., 2004, Hahn et al., 1993, Hopkins et al., 2000, Janssens et al., 2001, Kelly et al., 2000, Kim and Chung, 2004, Kook Kim et al., 2006, Mylavarapu et al., 2009, Spence et al., 2012) scan data. Airway meshes used to carry out CFD simulations are almost exclusively derived from MRI or CT scan data (Croce et al., 2006, Gambaruto et al., 2009, Ishikawa et al., 2006, Jeong et al., 2007, Pantle et al., 2010, Stringer et al., 2010, Tan et al., 2012, Wen et al., 2007). Once a digital airway surface has been extracted and extraneous geometrical features have been removed it can be modified or simplified if desired as in the cases of Doorly et al. (2008a), Grgic et al. (2004), Hörschler et al. (2006) and Kook Kim et al. (2006). CFD meshes and physical models can subsequently be derived from the digital airway surface. The use of scan data to produce meshes and physical models is associated with some issues. In some cases the scan data used is low resolution with scan planes 1 to 5 mm apart which can result in inadvertent simplification of the intricate airway geometry. Care must be also taken during airway surface extraction from the scan data as it is possible for the anatomy to be incorrectly defined as seems to be the case for the airway of Jeong et al. (2007) in which the superior regions of the left and right sides of the nasal cavity are connected. As CT and MRI scans are employed to identify the presence of disease it is uncommon for an entire, healthy upper airway to be captured which can limit the flow domain available.

Physical models developed for in vitro experiments by Hahn et al. (1993) and Schreck et al. (1993) used equally spaced cross-sections of the airway scans as templates from which sections of the airway

were cut out of plates of Styrofoam and acrylic, respectively, then assembled in order to form the full volume. Recently it has become more common to use 3D printing methods to form physical models from the digital airway surfaces, either by direct printing (Grgic et al., 2004, Janssens et al., 2001, Mylavarapu et al., 2009) or by printing the airway as a dissolvable solid, or 'negative', that is cast in silicone and then dissolved (Doorly et al., 2008a, Hopkins et al., 2000, Hörschler et al., 2006, Kelly et al., 2000, Kim and Chung, 2004, Kook Kim et al., 2006, Spence et al., 2012). The use of cadavers to form airway models has become rare in recent years as post-mortem the airway surface loses moisture, particularly in the highly vascular mucous membrane covering the nasal cavity walls, causing an increase in patency. Nevertheless an airway model was produced by the plastination of a cadaver head for the work of Croce et al. (2006) whilst Churchill et al. (2004) made acrylic models from the casts of one side of the nasal passages of ten different cadavers.

In the literature reviewed few of the physical models replicated the full upper airway from the nares to the trachea-larynx interface (Mylavarapu et al., 2009, Spence et al., 2012) with most instead encompassing only the nasal passageways from the nares to some region of the nasopharynx (Churchill et al., 2004, Croce et al., 2006, Doorly et al., 2008a, Hahn et al., 1993, Hörschler et al., 2006, Janssens et al., 2001, Kim and Chung, 2004, Kook Kim et al., 2006, Schreck et al., 1993). This latter case could affect flow patterns observed during expiratory flows as it has been shown that the contraction of the velopharynx produces a jet-like flow into the nasopharynx (Jeong et al., 2007, Spence et al., 2012, Stringer et al., 2010). Models are sometimes further simplified to include only one side of the nasal cavity and no nasopharynx (Hahn et al., 1993, Kelly et al., 2000), the septum wall extended into the nasopharynx (Churchill et al., 2004, Kim and Haw, 2004) or the full-width nasopharynx (Doorly et al., 2008a, Schreck et al., 1993). Due to the asymmetrical nature of the airways these simplifications do not faithfully replicate the conditions and could reasonably alter the flow characteristics observed. In particular the unilateral model used by Hahn et al. (1993) was truncated just posterior to the nasal septum and the flow-driving fan was mounted in line with the nasal cavity via a duct. A consequence of this is that expiratory flow characteristics produced by the expansion and change of flow direction which occur through the nasopharynx would not be observed. With the exceptions of Croce et al. (2006), Janssens et al. (2001) and Spence et al. (2012) the in vitro studies reviewed excluded the geometry of the face surrounding the nares, opting for a flat cross-section of the naris on an external model face or a tube lofted to the naris. As air is drawn from a hemispherical region around the nares the facial geometry may affect the flow profile entering the nostrils and should ideally be included (Doorly et al., 2008b). The inclusion of vibrissae was found in only the model by Hahn et al. (1993), who concluded their inclusion to have little effect on the flow within the main nasal cavity. No in vitro study replicated the natural and variable compliance of the airway or the temperature and humidity exchanges which naturally occur within it.

In the reviewed CFD studies the airway meshes employed had similar simplifications to the physical models with some encompassing the whole upper airway (Jeong et al., 2007, Stringer et al., 2010) and others just the nasal passages, with either one side of the nasal cavity included (Gambaruto et al., 2009, Hörschler et al., 2006, Pantle et al., 2010) or both (Croce et al., 2006, Ishikawa et al., 2006, Mylavarapu et al., 2009, Pantle et al., 2010, Wen et al., 2007). As with the in vitro models most airways excluded the facial geometry and began at a flat cross-section to the nares or naris, except in the cases of the airways employed by Croce et al. (2006), Taylor et al. (2010) and Stringer et al. (2010). At the pharyngeal end of the airway models the flow boundary was most often defined as a flat cross section of the nasopharynx (Gambaruto et al., 2009, Ishikawa et al., 2006, Pantle et al., 2010, Tan et al., 2012, Taylor et al., 2010) or the trachea-larynx interface (Mylavarapu et al., 2009) though some models included a lofted extension from either the nasopharynx cross section (Croce et al., 2006, Hörschler et al., 2006, Wen et al., 2007) or the trachea-larynx interface (Stringer et al., 2010) to allow for flow profile development. The compliance of the airways and presence of vibrissae were excluded in all reviewed CFD studies. The temperature and humidity exchange between the airway and the airflow was investigated only by Naftali et al. (1998) in a highly simplified model of one side of the nasal cavity.

3.2 Replication of Respiratory Flows for In Vitro and CFD Studies

Steady-state flow conditions were most commonly employed for in vitro experiments and CFD simulations, with inspiration and expiration flows supplied at one or more constant rates usually in the range of those found in vivo during natural breathing. Unsteady flow in vitro experiments performed by Naito et al. (1989) employed a live subject to provide the flow by mouth-breathing directly through the posterior access to the model nasopharynx. Though this method provides physiologically realistic flows accurate repetition would be difficult. A piston pump was used by two further in vitro studies to provide the unsteady flow (Janssens et al., 2001, Spence et al., 2012) which, in the case of Spence et al. (2012), was driven by a Fourier series derived from in vivo measurements. Unsteady CFD simulations were carried out by applying an oscillatory equation derived from in vivo breathing measurements (Naftali et al., 1998, Stringer et al., 2010) or a simple sinusoidal wave scaled to represent an average adult tidal volume and respiratory rate (Ishikawa et al., 2006).

An important component of simulating flow using CFD is the definition of boundary conditions and inflows and outflows. In the CFD study by Taylor et al. (2010) the influence of the inspiratory entrance condition to the nares was investigated and it was found that the form of the surrounding face affected the velocity profile entering the nares. This was not accurately replicated by applying a uniform velocity profile to the nares cross section, yielding significantly different flow patterns within the nasal passages. By extending the entrance to the nares with a convergent pipe and applying a

uniform or parabolic velocity profile to the inlet Taylor et al. (2010) obtained flow predictions much closer to those found when the face was included. A number of inflow and outflow boundary conditions were employed in the reviewed CFD studies including a uniform (Gambaruto et al., 2009, Ishikawa et al., 2006) and non-uniform (Hörschler et al., 2006) velocity profile at the nares, constant mass flux at the pharynx (Mylavarapu et al., 2009, Tan et al., 2012) and nares (Pantle et al., 2010), and, in the case of models which included the facial geometry, a uniform pressure at the pharynx flow boundary and a uniform ambient pressure at the open surface of a box surrounding the face (Croce et al., 2006, Stringer et al., 2010, Taylor et al., 2010).

3.3 Studies of Pressure

In Vivo

The conducting airways provide a path from the exterior to the lungs with the nasal cavity further acting to condition incoming air and recover heat and humidity during air expulsion. This passageway provides a resistance to the flow of air resulting in a loss of pressure along the flow path. The magnitude of this resistance depends on the form of the airways with the nasal cavity attributing approximately one half of the overall resistance during nasal breathing (Swift and Proctor, 1977). In most people the nasal mucosa which lines each nasal cavity alternately swell and shrink over a period of 3 – 7 hours known as the nasal cycle, causing changes in resistance within each cavity (Baraniuk and Kim, 2007, Hasegawa and Kern, 1978). The total resistance across the entire nasal cavity remains approximately the same throughout this cycle (Hasegawa and Kern, 1978). Verin et al. (2002) found that obstructive sleep apnoea (OSA) sufferers presented higher median upper airway resistance than their healthy counterparts whilst in a study of 1,000 rhinological patients by McCaffrey and Kern (1979) it was found that perceived nasal obstruction correlated well with increased resistance. While some pathologies increase the airway resistance which can lead to a predisposition to airway collapse, as is the case for OSA, others cause a reduction in the breathing effort a sufferer can exert as in the case of chronic obstructive pulmonary disease (COPD) (Chatila et al., 2004, Verin et al., 2002).

The fifth mechanism of action of NHF therapy proposed by Dysart et al. (2009) is the creation of PAP leading to improved lung recruitment. Mechanical ventilation by CPAP is commonly used as a means of providing PAP to increase lung recruitment and reduce the occurrence of apnoeas for patients ranging from neonates to adults (Campbell et al., 2006, Saslow et al., 2006, Shoemaker et al., 2007, Smith et al., 2003, McKiernan et al., 2010). CPAP therapy generates PAP by administration of positive pressure flow to the user via a sealed nasal or full-face mask. As this type of therapy can be poorly tolerated due to the restrictive nature of the mask it is sometimes necessary for escalation to invasive respiratory support such as intubation (Groves and Tobin, 2007, McKiernan et al., 2010). An

alternative non-invasive method of generating PAP without the use of a restrictive mask is provided by NHF therapy.

NHF therapy has become a widely accepted treatment for term and preterm infants (de Klerk, 2008, Shoemaker et al., 2007) and has been the focus of much recent research with many in vivo studies finding significant levels of PAP generated within the upper airway during use (Kubicka et al., 2008, Milési et al., 2013, Spence et al., 2007, Wilkinson et al., 2007). The use of NHF therapy as an alternative to CPAP in adults is less common; however, adult in vivo studies have found PAP generation by NHF therapy. In a study of 10 healthy adults Groves and Tobin (2007) found increased expiratory pharyngeal pressures occurred during NHF therapy with pressure related to the rate of flow for both open and closed mouth positions. The closed mouth position produced significantly higher pressures while significant differences were also seen as a result patient gender with females experiencing greater pressures. A similar study by Ritchie et al. (2011) also measured positive pressures in the laryngopharynx with an almost linear relation between NHF flow rate and pressure in 10 healthy adults during at rest nasal breathing. A positive linear relationship between NHF flow rate and pressure within the oropharynx was also reported by Parke et al. (2011a) for both mouth open and closed breathing in a study of 15 post-cardiac surgery patients. A recent study by Bräunlich et al. (2013) of the effects of NHF therapy on patients suffering from COPD and idiopathic pulmonary fibrosis (IPF) found an increase in both mean pressure and pressure amplitude in the nasopharynx with the use of NHF when compared to spontaneous breathing.

Measurements of nasal resistance and pressures in vivo provide useful physiological information but are limited in many ways such as accessibility. Rhinometry measurements capture the flow rate and pressure difference across the nasal cavity for anterior rhinometry and between the nares and the oral cavity for posterior rhinometry, allowing for the determination of resistance over these larger regions. Measurements of pressure at more specific positions within the airway are possible through the use of catheters, either with micro-transducers mounted within the catheter body or attached to external transducer systems (Akkermans, 1991), however use of catheters is invasive and placement approximate.

In Vitro

In vitro experimental methods provide an alternative to in vivo measurements allowing for greater airway access and greater control of the variables such as airway geometry and respiratory rate which vary widely across adult populations. In a 3:1 scale of a healthy, adult left nasal passage Schreck et al. (1993) measured the pressure drop across three regions; the nasal vestibule, nasal cavity and the nasopharynx; during a range of constant inspiratory and expiratory flows. It was found that for flows greater than 15 LPM the major contributor to pressure losses was the rapid contraction and expansion

at the nasal valve. This is similar to the in vivo findings of Swift and Proctor (1977) who found that the largest pressure change occurred within the first 1.5 cm of the nasal cavity for normal subjects. Moody plots made from the nasal valve measurements indicated a transition from laminar to turbulent flow regime at an approximate flow rate 15 LPM, the same flow rate at which the nasal valve became the highest contributor to pressure losses. Further pressure measurements by Schreck et al. (1993) showed that reduction of the cross-sectional area of the nasal valve, blocking of the upper and middle meatuses and increasing the size of the inferior turbinate all caused increased pressure losses.

Measurements of the pressure differential across the nasal cavity of a plastinated head at a range of constant inspiratory and expiratory flow rates by Croce et al. (2006) were used to derive Moody diagrams for the individual left and right sides and the nasal cavity overall. For each of the three regions the inspiration and expiration curves aligned inferring resistance and pressure losses within the nasal cavity were the same in both flow directions. Naito et al. (1989) investigated the influence of 18 nasal abnormalities on the resistance of a nasal passage model during natural breathing flows. Of the diseases replicated swelling of the inferior turbinate, either at the anterior portion or severe diffuse swelling, was found to generate the most significant resistance increase. This was further exacerbated when the severe diffuse swelling was simulated in conjunction with other minor abnormalities.

In vitro measurement of static pressures during a steady expiratory flow were made at 16 positions within a twice scale upper airway model in a study by Mylavarapu et al. (2009). Pressure ports were located along the length of the posterior pharynx, along the inferior lateral wall of the left nasal cavity, and around the perimeter of the velopharynx cross-section. It was stated that a constant peak flow rate of 200 LPM was used due to a lack of low-pressure sensing range, however it is not clear whether this value is that used in vitro or whether it has been scaled back by half to in vivo levels. In either case this flow rate is much higher that the peak flow rates seen in vivo during resting breathing. Nevertheless the use of a high concentration of static pressure measurement positions throughout the airway illustrated local pressure differences not seen in other in vitro or in vivo studies. A large reduction in pressure was observed as the expiratory flow passed from the oropharynx into the minimum cross section of the velopharynx followed by a pressure recovery during the expansion into the subsequent nasopharynx. A wide variation in static pressure was seen around the velopharynx circumference with a highly negative pressure at the anterior wall yet a positive pressure at the left wall. Measurements at the four equally-spaced points along the length of the nasal cavity showed an almost constant pressure until a large drop occurred at the most anterior point, again agreeing with the findings of Swift and Proctor (1977) that the majority of the nasal cavity losses occur within the anterior region.

CFD

The use of computational fluid dynamics (CFD) allows for comprehensive mapping of flow characteristics within complex geometries and as such has been employed in a number of studies to investigate flows in nasal cavities and upper airways. It has been proposed that CFD could be used by surgeons to validate modification strategies for correcting nasal pathologies prior to surgery to reduce the rate of unsuccessful procedures (Müller-Wittig et al., 2002, Pantle et al., 2010). Although CFD has the power to provide large amounts of information such investigations are computationally expensive and are in most cases only solved for constant flow conditions. Furthermore experimental replication in some part is required for validation of the model and results. In a flow study within a plastinated head by Croce et al. (2006) a CFD model of the airway was reconstructed from CT scan images of the head used for in vitro measurements. A linear model was used to simulate constant inspiratory flow rates of 6.54, 13.86 and 21.18 LPM. Mean total pressures within each side of the nasal cavity were extracted at numerous cross sections along its length from which it was determined that 48% of the total pressure losses occurred in the region of the nasal valve and 76% occurred before the beginning of the turbinates, agreeing well with the findings of Schreck et al. (1993). Similarly, Wen et al. (2007) found the greatest resistance to pressure occurred in the first 1.5 – 2.5 cm from the nasal inlet when simulating steady-state flows through a nasal cavity using a Reynolds-averaged Navier-Stokes based k-ω turbulent model. A study by Hörschler et al. (2006) investigated the impact of the inferior and middle turbinates on pressure losses through the nasal cavity by simulating constant flows through simplified and modified nasal passages. Through this they found that the presence of the lower turbinate had the greatest impact on the pressure losses through the nasal cavity. An evaluation of CFD modelling methods during steady state flows through an upper airway was carried out by Mylavarapu et al. (2009) and compared to experimentally determined pressures from which it was concluded that use of the standard *k-ω* model produced the most similar results.

3.4 Studies of Flow Patterns and Turbulence

In Vitro

Many in vitro experiments and CFD studies have been dedicated to determining the airflow patterns within the upper airways. Flow visualisation methods using tracer fluids have been used for decades to observe the flow patterns within the nasal passage and upper airway (Churchill et al., 2004, Doorly et al., 2008a, Müller-Wittig et al., 2002, Proetz, 1953). A study by Churchill et al. (2004) which used constant flows of water and tracer dyes to visualise the flows through ten acrylic adult nasal passage models found that not only did the flow regime vary significantly across the sample group, so too did

the path of major flow. No model exhibited truly laminar flow for any of the flow rates tested, with three models showing fully turbulent flow at the lowest in vivo flow rate (1.5 LPM), and two models persisting with transitional flow through to the highest in vivo flow rates (39 and 42 LPM). In a recent study by Doorly et al. (2008a) a number of recirculating flows were identified within a twice scale nasal cavity model with the use of dye visualisation and particle image velocimetry (PIV). PIV employs short exposure cameras to capture the movement of light-reflecting particles usually within a plane of the flow domain illuminated by a sheet of laser light. The movement of the particles between consecutive frames can be resolved by correlation techniques to provide both qualitative and quantitative flow data (Chung and Kim, 2008). This is performed computationally in the case of digital PIV (DPIV). In more recent years PIV has been employed to experimentally determine the flow patterns and velocities within realistic and idealised nasal and upper airway geometries (Doorly et al., 2008a, Hopkins et al., 2000, Kelly et al., 2000, Kim and Chung, 2004, Kim and Haw, 2004, Kook Kim et al., 2006, Spence et al., 2012, Versteeg and Hargrave, 2001).

Most PIV studies of nasal airway flows to date have employed steady state flows within the range of flow rates seen in vivo during at rest breathing. A number of these studies observed the occurrence of a recirculation zone at the anterior nasal cavity during inspiration, superior to the nasal valve (Doorly et al., 2008a, Hopkins et al., 2000, Hörschler et al., 2006, Kelly et al., 2000). Doorly et al. (2008a) reported the presence of further recirculation zones in the anterior of the middle meatus and at the posterior of the olfactory zone during inspiration. PIV measurements during expiration by Hörschler et al. (2006) displayed a jet-like flow projecting onto the roof of the nasopharynx from the pharynx and being directed toward the superior meatus, whilst during inspiration flow was said to be concentrated toward the middle meatus. Inspiratory acceleration through the nasal valve was observed in studies by both Doorly et al. (2008a) and Kelly et al. (2000). From their results Hörschler et al. (2006) and Kelly et al. (2000) suggested that the flow within the nasal airway was laminar.

A transient PIV study which employed a realistic at rest breathing pattern was undertaken by Spence et al. (2012) using a 1.55 scale model of the control airway employed for the current research identified as airway 06B. During the inspiratory phase a region of flow stagnation was seen in the anterior nasal cavity above the nasal valve, however the recirculating flow described in other steady state experiments (Doorly et al., 2008a, Hopkins et al., 2000, Hörschler et al., 2006, Kelly et al., 2000) was not present in this area. During peak expiration a jet-like flow from the pharynx was directed toward the roof of the nasopharynx and below this a vortex developed as the flow separated from the anterior pharynx wall as it curved forward to form the floor of the nasal cavity. During both expiration and inspiration the flow was seen to be concentrated to the middle airway with low flow in the olfactory zone and meatuses. Differences in the flow pattern were seen at similar instantaneous flow rates during the increase to and decrease from peak expiration, inferring that a quasi-steady assumption is inaccurate to describe the flow. Within the same study Spence et al. (2012) also

investigated the influence of Optiflow™ NHF therapy at a flow rate of 30 LPM on the upper airway flows during transient breathing. High velocities were observed at the nasal valve during expiration as the jet from the cannula entered the nasal cavity and was turned back on itself to exit through the nares with the expiratory flow from the lungs. Recirculation zones were mapped within the anterior nasal cavity both above and below the nasal cannula jet during this expiratory flow. As with the natural breathing condition expiratory flow from the pharynx was directed toward the nasopharynx roof; however, no vortex was seen below this. During inspiration the vortex in the anterior nasal cavity above the cannula jet persisted while the lower vortex had all but disappeared. The jet of flow exiting the cannula was directed toward the roof of the nasal cavity during inspiration and was the site of maximum velocity during both inspiration, 16.5 m/s, and expiration, 13.6 m/s. Contrary to the findings during natural breathing, the quasi-steady flow assumption was deemed applicable to the flows observed during the application of 30 LPM NHF therapy.

Velocity and turbulence profiles within a 20-times scale human nasal cavity at steady inspiratory and expiratory flow rates were investigated using hot wire anemometry during research by Hahn et al. (1993). Measurements were taken along 85 lateral-medial traverse lines distributed vertically within six coronal sections of the nasal cavity spanning the naris to the nasopharynx, allowing for velocity and turbulence mapping within the six sections. During an in vivo inspiratory flow rate of 10.8 LPM, representing an average breathing flow rate, flow was found to be most highly distributed within the lower and middle passages of the nasal cavity. Vibrissae were simulated in the nasal vestibule for some measurements and though it was found their presence did slightly increase inspiratory turbulence intensity near the nasal valve from 2.5% to 2.9% it had little effect on the downstream velocity profile. Turbulence intensities within the nasal cavity at natural inspiratory flows were found to be low with a maximum of 3.4% found at the superior entrance to the nasopharynx. Turbulence intensities for natural expiratory flows were not given. Hahn et al. (1993) described the flow regime during natural breathing flows to be disturbed laminar due to the presence of low turbulence intensities throughout the nasal cavity.

CFD

The complex flow patterns within the upper airway have been mapped with the use of CFD in a number of studies, most of which employ steady state conditions (Croce et al., 2006, Hörschler et al., 2006, Jeong et al., 2007, Stringer et al., 2010, Wen et al., 2007, Tan et al., 2012) and focus on the region spanning the nares to the nasopharynx (Croce et al., 2006, Hörschler et al., 2006, Ishikawa et al., 2006, Wen et al., 2007). The presence of a vortex above the nasal valve in a sagittal section of the anterior nasal cavity was reported in one or both sides by Croce et al. (2006), Hörschler et al. (2006), (Tan et al., 2012) and Wen et al. (2007) during steady inspiration whilst simulations by Stringer et al. (2010) found no vortices in this region in either side for similar steady-state conditions. This agrees

with the findings of PIV studies described in the previous section which have also shown the presence and absence of recirculation in this zone for different airway geometries during steady inspiratory flows. Further vortices were found in cross sections of the nasal valve (Wen et al., 2007) and within the anterior nasal cavity below the nasal valve (Croce et al., 2006) during steady inspiration. The path of mean inspiratory flow varied among studies though consistently low flows were seen in the superior region (Croce et al., 2006, Hörschler et al., 2006, Stringer et al., 2010, Wen et al., 2007). Simulations within the full upper airway region by Jeong et al. (2007) described the presence of a turbulent jet within the pharynx during steady state inspiration with high shear stresses acting upon the walls of the velopharynx increasing the chance of airway collapse. Stringer et al. (2010) also investigated flows within the pharynx and found the highest turbulent kinetic energy to be concentrated within the velopharynx and nasopharynx during the expiration phase. Further steady state simulations were performed by Stringer et al. (2010) with the inclusion of an Optiflow™ nasal cannula delivering 30 LPM NHF therapy at peak inspiration and expiration. From these simulations high velocities were seen in the region of the nasal valve and through the middle and superior airways while high vorticities were found in the anterior nasal cavity and near the anterior velopharynx. During expiration the cannula jet was observed to turn back on itself forming a clockwise vortex on the floor of the anterior nasal cavity. A transient analysis of the nasal passage flows performed by Ishikawa et al. (2006) found highest vorticities in the anterior nasal cavity and the posterior nasal cavity near the middle turbinate during peak inspiration whilst during peak expiration the former remained but the latter changed to near the posterior septum wall. Ishikawa et al. (2006) described the flow as laminar as the vortices were time-dependant but not random.

3.5 Studies of NHF Therapy and Carbon Dioxide Washout

A number of clinical studies have been undertaken to measure the rate of success of NHF therapy for respiratory support in comparison to more conventional non-invasive treatments such as low-flow nasal cannula (LFNC), high-flow face mask (HFFM) and CPAP. In these trials blood oxygen saturation and rate of intubation or reintubation are often used to measure therapy success, alongside other factors such as respiratory rate and therapy tolerance. A randomized trial of the use of NHF therapy for post-extubation preterm infants by Campbell et al. (2006) found that it was less effective than conventional CPAP therapy and resulted in a higher rate of reintubation and higher O_2 consumption; however, a retrospective study conducted by Shoemaker et al. (2007) of preterm infants who received either NHF therapy or CPAP within 96 hours of birth found that patients who received NHF therapy required fewer ventilator days whilst CPAP failure was more likely to result in intubation. In adult populations NHF therapy is more commonly used as a substitute for LFNC and HFFM therapies (Ward, 2013). Tiruvoipati et al. (2010) conducted a randomised cross-over trial to

compare the outcomes of HFFM and NHF therapy on 50 post-extubation adults and found that both provided a similar level of support with no significant differences in blood oxygenation, blood pressure, heart rate, or respiratory rate; however NHF therapy was found to be better tolerated by the patients. Two further studies compared ICU patients treated with NHF therapy to those treated with HFFM. A prospective open study by Nicolet et al. (2011) allocated 40 post-operative cardiac patients either to NHF therapy or HFFM mask based on equipment availability and determined no significant differences in the rates of hypoxemia or re-intubation but did find higher tolerance of NHF therapy. A more structured study by Parke et al. (2011b) assigned 60 ICU patients to either NHF therapy or HFFM in a randomised controlled trial and monitored their blood oxygenation and rate of escalation to non-invasive ventilation (NIV), concluding that NHF therapy success was significantly greater than HFFM with NHF patients having fewer blood oxygen desaturations and a lower rate of escalation to NIV. Chatila et al. (2004) investigated the effectiveness of NHF at providing support to COPD patients during rest and exercise in comparison to mouth-delivered low flow oxygen in a cross-over trial and found NHF enabled greater exercise time and increased blood oxygenation. Other studies have found that the use of NHF was able to increase the blood oxygenation in comparison to spontaneous breathing in ICU patients (Sztrymf et al., 2011) and patients suffering from severe acute respiratory infection (Rello et al., 2012). A further study by Bräunlich et al. (2013) measured reduced CO_2 partial pressures in the capillary blood of patients suffering from IPF and COPD during the use of NHF therapy inferring it provided a CO_2 washout effect.

The in vivo measurements have provided evidence of the effectiveness of NHF therapy in increasing blood oxygenation in a manner similar to or greater than currently used non-invasive therapies, supporting its use for those suffering mild to moderate respiratory distress. However, the occurrence of CO_2 washout cannot be confirmed from the blood gas measurements alone. The PIV mapping by Spence et al. (2012) of upper airway flows during transient breathing with NHF therapy implied some level of washout occurred due to a continuous flow of air exiting the nasal valves below the cannula jet during the entire breath cycle. To the knowledge of the author no studies of the CO_2 or O_2 concentrations within the conducting airways during breathing with NHF therapy have been conducted to date. Therefore it is the major objective of this research to measure these concentrations during transient breathing with and without the presence of NHF therapy to determine whether CO_2 dead space washout occurs and to what extent it is affected by therapy flow rate and airway geometry.

3.6 Conclusions

Though in vivo measurements of pressures within the upper airways have been performed at point locations, accessibility difficulties prohibit detailed pressure mapping throughout the region or measurement of other elements of interest such as flow velocities, turbulence and gas concentrations.

Simulations by CFD can be performed to determine flow characteristics which cannot be measured in vivo; however, these simulations are computationally expensive and as such are often restricted to steady state analysis and, furthermore, require some manner of experimental replication for validation. In vitro experiments within replica respiratory systems however provide a means of performing invasive measurements while maintaining close control of the system variables. It is for these reasons that the investigations carried out within this research were, in all but one case, performed in vitro.

Anatomically accurate airway models for in vitro experiments can be constructed using CT scan data providing scan resolution is high and the airway surface is correctly extracted. Models of airway geometry frequently contain only the complex anatomy of the nasal passage, omitting the significant features within the pharynx and often retaining only one side of the nasal cavity. In this research airway models containing the full upper airway from the face surrounding the nose to the trachea-larynx interface were 3D-printed from high resolution CT scan data so that all significant anatomical features were retained.

A large number of previous in vitro and CFD studies employed steady state flows when investigating flow characteristics within the airways. However, it has been suggested that the transient flows within the upper airway cannot be assumed quasi-steady. Thus to properly replicate the transient and oscillatory nature of the human breathing pattern, in all in vitro experiments within this research transient flows based on in vivo measurements are employed.

4 Airway Model Development

The airway models employed throughout this research to conduct the experimental testing were 1:1 scale replicas of human airways reproduced from CT scan data of various adults. A total of five different adult airway CT scans were developed into models, one of which was made three times via two different manufacturing methods. The first six models were developed in 2011 as a part of research carried out for a University of Canterbury Mechanical Engineering Final Year Project sponsored by FPH. These six included two models made from the same airway CT scan data, referred to as airway 06B. A second model, airway 06B[2], was produced from this airway after issues were found in the method of introducing pressure taps into the initial model, airway 06B[1], making it unusable for static pressure measurements though still useful for other experiments. The seventh model, a reproduction via a different printing method of the second airway 06B model with reduced material, was manufactured during the course of this research giving a total of three models from the airway 06B data. All models were manufactured using 3D printing methods. Table 1 lists the seven different airway models used over the course of this research, the names by which they will be referred to in this thesis and certain other important details pertaining to each.

Table 1: Details of the upper airway models used for this research.

Airway N^o	Reference Name	Age	Gender	Printing Method	Material	Volume [ml]
06B	Airway 06B[1]	44	M	FDM	ABS	53.84
	Airway 06B[2]			FDM	ABS	
	Airway 06B			Jetted Photopolymer	Acrylic	
07B	Airway 07B	43	M	FDM	ABS	60.16
09	Airway 09	41	F	FDM	ABS	48.27
10	Airway 10	51	M	FDM	ABS	57.57
16	Airway 16	17	M	FDM	ABS	43.70

4.1 Digital Airway Preparation

The first step to preparing the models for printing was to extract the airway surface from CT scan data. A CT scan takes multiple sequential two-dimensional images of the body density at each image

slice across the scan volume. The colour of each pixel, ranging in greyscale from black to white, denotes the density measured at the pixel position. Together, the collection of image slices forms a three-dimensional density map. Each of the five airway CT scan datasets chosen had an image slice separation of 0.6 mm, thus preserving a large amount of airway detail. To extract the airway surface from these images the process of segmentation was used. Segmentation is an operation which separates pixels into two groups either side of a nominated pixel density value, known as the threshold. The interface of these two sets of pixels is then extracted as a surface. The selection of the threshold value used to extract each airway was made by trial and error iterating the process until the surface extracted was as complete and correct as possible, when compared to the known upper airway anatomy, without omitting any significant features.

Before the airway surface was edited and developed into a physical model it was first scrutinised to ensure it met a number of important criteria. One of the criteria imposed was that the airway should be healthy and representative of the general population, free of any geometric defects which may adversely affect experimental results. A consequence of this is that most scans which contain the full upper airway are not likely usable as they are taken with the express purpose of mapping the airway to detect irregularities. As there are health risks associated with excess exposure to the CT scanning process, it is uncommon for the entire upper airway to be captured in scans taken of other anatomical features within the same area. These two factors made acquisition of appropriate scan data a difficult task and thus the first check of segmented airways was to ensure all relevant geometric features, from the nares to the top of the trachea, were present and not truncated during the scanning process. A total of five airways of the twelve unique available scans met these criteria.

It was necessary then to edit each extracted airway surface to remove certain extraneous features such as the paranasal sinuses, auditory tubes and the tear ducts (Tortora and Derrickson, 2006). As the sinuses and the auditory tubes are air reservoirs which are only open to the exterior via small ostium into the upper airway, they do not experience significant air movement but rather pressure equalisation. Although the tear ducts are open to the exterior at both ends, the opening of the tear ducts into the nasal cavity is protected by a thin mucous membrane, Hasner's membrane, which helps to prevent flow back into the duct (Müller et al., 1978). These features therefore do not participate in the flow of air through the upper airway during breathing and were removed to reduce the model size and allow greater access to the airway. Each feature was removed as close to the airway volume as possible, where the diameters of the connecting orifices were at minimum. The small holes which remained in the airway surface meshes were capped with domes to provide a smooth continuous surface which would not adversely affect the flow pattern.

Further editing was required to crop each surface so that only the upper airway and some of the facial geometry was present. A small region of the face around the nose was retained as during inhalation air is drawn from a hemispherical region around the nares, the flow profile within which may be affected

by the surrounding geometry (Doorly et al., 2008b). Additionally, a certain amount of the facial geometry below the nares had to be retained to allow the nasal cannulae to be properly fitted to the final models. The inferior portion of the airway surface was truncated so that the passage terminated at the transition from larynx to trachea. Each mesh was therefore an open surface encompassing only the complex upper airway and a portion of the face. The open mesh of the first upper airway, airway 06B, is shown in Figure 7.

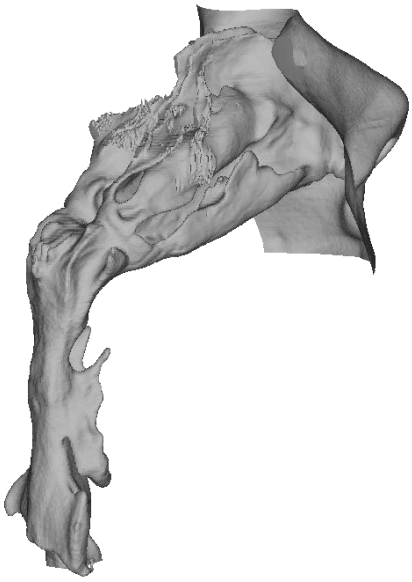

Figure 7: Open mesh of upper airway 06B.

Before these meshes could be materialised into physical models, the open surfaces had to be closed to provide a three dimensional volume. This took the form of an irregular box fitted to the shape of the airway, with the facial features forming one face and the inferior outlet of the upper airway exiting on another. The airway formed a cavity through the box which could be manufactured by 3D printing. As the trachea was to be represented in the experimental system as a circular tube with a 15 mm diameter, a smooth transition from the larynx-trachea cross section of the airway mesh was accomplished by forming a lofted surface to a 15 mm diameter orifice on the base of the box.

Because the airways were to be 3D printed it was deemed necessary to make each so the majority of the airway could be easily accessed for inspection and removal of any remaining support material deposited during printing. This lead to the sectioning of each airway model into three parts, a left and right side plus a small central piece containing the nasal septum. An example of these is shown in the form of airway $06B^2$ in Figure 8.

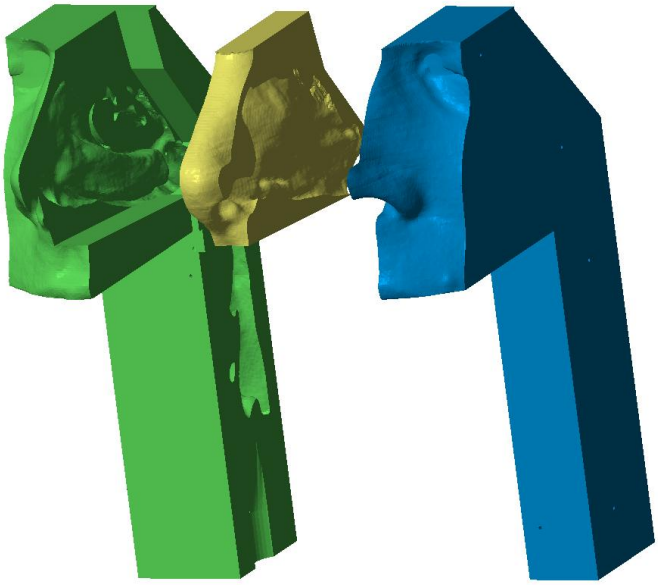

Figure 8: Three pieces of the airway 06B^2 model.

Prior to manufacture, each airway model mesh was prepared for the measurement of static pressures in various locations by the introduction of pilot holes for pressure taps. In the case of the first airway 06B^1 model pressure taps were drilled post manufacture without the use of pilot holes and, on inspection, it was found that a number of the taps did not enter the model normal to the airway surface. This introduced error to the static pressure measurements from dynamic pressure effects. Establishing pilot holes for the pressure taps in the model mesh allowed for accurate placement, ensuring each tap entered the correct anatomical region perpendicular to the airway surface. Five to six bolt holes for locating and securing the model pieces together were also introduced to each airway model at this stage.

Some of the later models to be manufactured underwent a final editing process before printing. As large portion of the production costs is for the print material, reduction of material volume was valuable. It was possible to achieve this by performing a shelling operation in which the solid volume was reduced to a shell with a minimum wall thickness of 3 mm. In the case of the airway 06B model further editing was carried out to remove as much of the non-functional material as possible. This left the airway surface, the lower face of the original box and circular bosses for the bolt and pressure tap holes. A comparison of this airway 06B model version to the earlier airway 06B^2 version is given in Figure 9 to show the volume reduction.

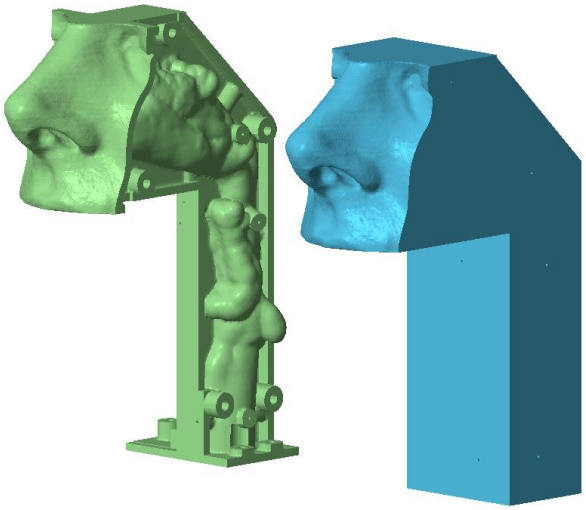

Figure 9: Reduced material airway 06B model compared to the earlier airway 06B[2] model.

4.2 Model Manufacture

The initial six airway models made in 2011 were manufactured using the fused deposition modelling (FDM) process. This produced models in ABS plastic by depositing heated layers of the plastic filament in 0.254 mm thicknesses. These models are highly cost effective but due to the method of manufacture are prone to a small level of porosity. This issue was addressed during model clean up. The duplicate airway 06B model was manufactured during the course of this research by the more refined process of jetted photopolymer printing, using the Projet HD 3000 Plus by 3D Systems. This produced non-porous model pieces out of an acrylic photopolymer, Visijet EX200, with a layer thickness of only 29 μm.

A few post-manufacture clean up and preparation tasks were required to make the models ready for experimental use. Support material deposited during the 3D printing process was removed. Pressure tap holes placed in the model before printing were drilled out to size with a hand drill. As previously remarked the FDM models suffered from a small level of porosity due to the manufacture method. To mitigate this issue the inner surfaces of the FDM models were sealed with multiple coatings of diluted PVA glue. As PVA is water soluble, this method of sealing allowed for future removal if desired. The sealing of the inner surface also provided a second benefit by smoothing the transitions between the layers of the model, reducing the surface roughness. During the process of support material removal; using hot water, detergent, sonication and scraping; the central piece of the acrylic airway 06B model became slightly bowed such that when assembled the model had a not insignificant gap between the central and right pieces. The warped central piece was straightened by reheating it in a bath of hot water just below the melting temperature of 65°C then bending it carefully back into shape so that it

lay level on a flat surface. Great care was taken to ensure the rest of the piece was undamaged during this process. Figure 10 shows the three pieces of the airway 06B model duplicate prior to assembly.

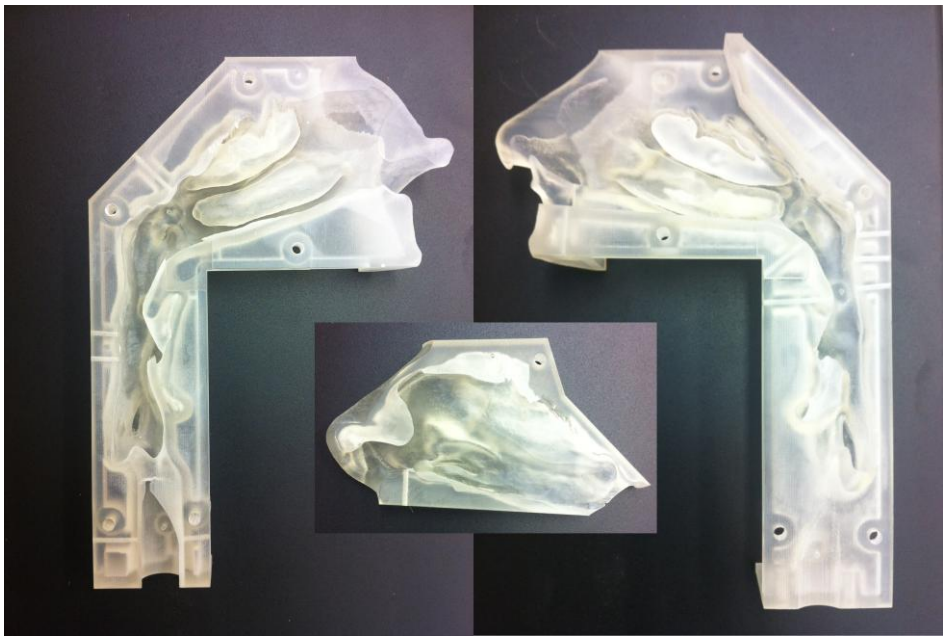

Figure 10: Three pieces of airway 06B model prior to assembly.

Assembly of the models required a sealant between the pieces to prevent leaks. Universal Blue™, a non-setting gasket sealant made by Hylomar™, was used for this purpose as it provided a seal without permanently binding the pieces together. A thin layer of Universal Blue was spread across all contacting surfaces of each model pieces before assembly. The pieces were then assembled with firm finger pressure and fastened together with bolts to provide a tight fit with no movement between the pieces. As the Universal Blue is a non-setting sealant tightening of the bolts caused excess product to move to the edges of the pieces. To mitigate this each model was unfastened and opened so all excess product which had migrated into the airway could be removed. Models were then reassembled and again fastened and tightened as before, ready for experimental use.

5 Experimental Respiratory System

Throughout the course of this research an experimental respiratory system designed to replicate that of an average human adult was developed and evolved for use in the in vitro experiments. This research was performed in vitro as it allowed for improved accessibility along with much greater control of respiratory parameters for the variety of measurements desired when compared to the much less accessible and varied nature of in vivo experiments. To gain meaningful information from this research it was then important to develop a system which faithfully replicated an average human respiratory system with which the experiments could be conducted. The experimental respiratory system which was developed and utilised took a number of different forms over the course of the research dependent on what measurements were being conducted, however the major components consistent throughout all variations were the pump, airway models and the Optiflow™ cannula system. This chapter described in detail all versions of the experimental respiratory system employed.

5.1 Permanent System Components

This section details the experimental system components which were employed in all of the experiments performed and described within this thesis.

5.1.1 Airway Models

As described in the previous chapter, seven different airway models derived from five unique airway geometries were used during the course of this research. Three of these airway models were slightly different versions of the same model, all containing the same airway geometry of airway 06B. This airway 06B geometry was chosen as the benchmark airway for all in vitro experiments, each employing one of the three duplicate models as stated in the method. The other four airway models were used only in experiments where the effect of airway geometry on turbulence intensity and Optiflow™ NHF therapy efficacy were investigated. All models had 21 equivalent pressure tap holes entering the airway from the outer surface of the model through which the pressure taps required for static pressure measurement could be inserted. These holes were kept to a minimum (1.7 mm diameter) and entered the airway perpendicular to its surface to prevent flow disturbance. When not in use for pressure measurement these holes were sealed off with Blu Tack™ at the outer surface of the model.

Figure 11: Comparison of the new acrylic airway 06B model (left) to the older style airway 06B^2 model made of ABS plastic (right).

All but one of the airway models was manufactured in ABS plastic via 3D printing during previous research, with the most recent model printed in acrylic during these studies. An example of each type of model is given in the photo of Figure 11. The inferior face of the models was a flat surface containing a 15 mm diameter hole, lofted to the airway as described in Chapter 4. Aluminium connections, also produced in the previous research, provided a method of attaching a flow delivery passageway to the airway model. These connections, with a 15 mm diameter hole on one face to match that on the model, could be secured to the airway models either by bolts or with a thin layer of silicone glue. When bolted, a thin layer of Universal Blue gasket glue was used to provide a seal whilst the use of silicone glue alone both fixed the connection to the airway and provided a seal. A dowel was used to align the two holes when fixing the aluminium connection to the airway models. At the opposing end of the aluminium connection was a tapped hole into which a 15 mm inner diameter brass tube with a 1/2 inch BSP F external thread could be fastened. This provided a smooth, straight entrance for flow from the pipe to enter into the airway model.

5.1.2 Lung Pump

A piston pump, inherited from previous research within the same field and illustrated by Figure 12, was used to replicate the action of an average pair of human lungs by providing the transient oscillatory flows of breathing. An acrylic tube with a nominal diameter of 140 mm comprised the pump cylinder with an acrylic piston head sealed by two back-to-back nitrile lip seals. A Hirwin precision rolled ball screw and ball nut with a 5 mm pitch provided the linear piston motion from an

Astrosyn L259RE stepper motor driven by an Astrosyn P808A stepper motor driver. A fixed block style support and SBC flange supported the ball screw while a Rollon compact 18 series rail with a T slider supported the piston rod. A National Instruments 9401 digital module and a 9172 compact DAQ chassis allowed the stepper motor to be controlled by a Labview program which took a five coefficient Fourier series input to replicate the oscillatory flow of breathing.

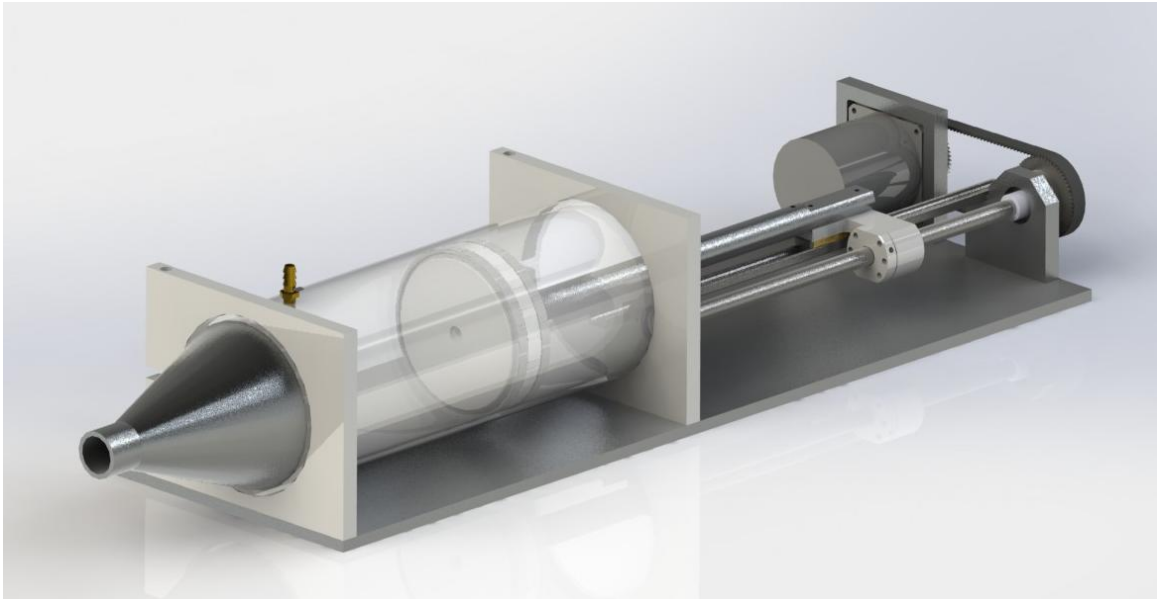

Figure 12: Illustration of the piston pump employed to replicate the action of the lungs.

The volume contained within the pump could be altered by shifting the home position of the piston and was controlled so that during CO_2 washout measurement it contained the same volume as the FRC of an average adult. In its original form the outlet of the pump consisted of a cone and numerous industrial connections necking it down from the pump diameter to 20 mm, similar to an approximate trachea diameter of 25 mm (Tortora and Derrickson, 2006). This large number of connections, shown in Figure 13, contained a large volume which was initially assigned as a portion of the lung FRC in the early CO_2 decay measurements of Experimental Method Version One. However a measure of the system's fidelity was carried out which proved that this system, although adequate for testing pressure and turbulence within the upper airway, was not accurately replicating the cycle of gas concentrations observed at the nares of a live subject. As a result of this the design of the pump was changed so that at its outlet was a flat acrylic plate with a single, circular orifice to which the components making up the anatomic dead space, including the gas sensing elements and the upper airway models, could be directly attached. This new pump design is illustrated in Figure 14. With this new exit condition it was possible to contain the entire FRC, taken to be the average adult value of 2.4 litres, within the lung pump and the anatomic dead space without. By making these adjustments to the pump the gas concentration cycle issues were rectified so that the system closely replicated the CO_2 concentration cycle of a live subject.

Figure 13: Large number of connections at the original pump exit.

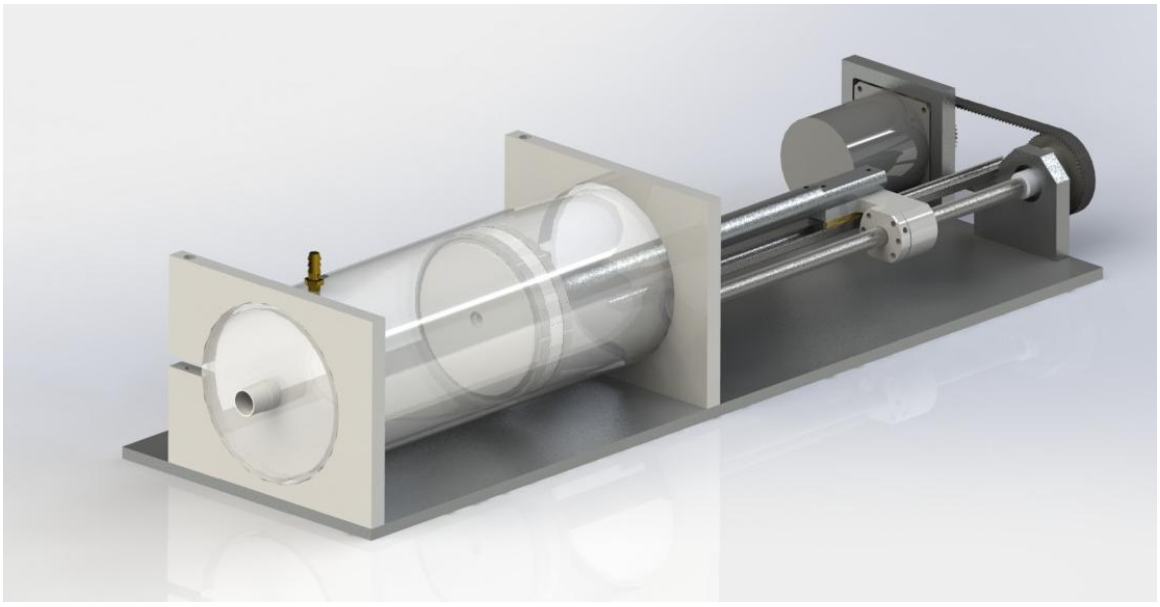

Figure 14: Illustration of piston pump with improved flat plate exit.

5.1.3 Optiflow™ Nasal High Flow System

Throughout all experiments in which NHF therapy was applied to the airway models FPH Optiflow™ cannulae were used with one exception, in the case of the final CO_2 washout experiment detailed in Chapter 9 where a flared prong cannula was employed. Large size cannulae were employed for all experiments bar those in which cannula size and prong penetration depth dependencies of CO_2 washout were examined. Air at room temperature from a reticulated compressed airline was used to supply the cannulae with the high flows. For each experiment air from the airline was directed through a Norgren pressure regulator, Platon NG series rotameter and a FPH breathing circuit filter before entering a standard FPH RT-series breathing circuit and finally into an Optiflow™ cannula. The level of NHF required was set at the rotameter by supply adjustment at the pressure regulator.

All of the three Optiflow™ cannula sizes available were used for some experiments during the course of this research. When fitting the cannulae on the model a standard process was always undertaken. The cannula was rested in the space below the nostrils and above the upper lip of the model. The prongs were adjusted so that they protruded into the nostrils at their natural angle. The cannula elastic strap was then strung around the model and pulled tight so that the cannula was held fast but not strained from its natural resting position. Finally the cannula positioning was checked and adjusted so that it was sitting centrally between the two nares.

When NHF therapy was administered to the airway models during experiments, a range of measurements were taken to encompass NHF flow rates from 10 to 60 LPM at discreet intervals of 10 LPM. This range is of particular interest as it is the range of Optiflow™ NHF therapy flow rates which are currently used by clinicians. As the air supplied to the Optiflow™ cannula for experimentation was sourced from a reticulated airline, airline pressure was sometimes low and flows greater than 60 LPM were unattainable. However, whenever flows greater than 60 LPM were possible during testing experiments were conducted to the highest possible flow rate at the same 10 LPM increments.

5.2 Static Pressure Measurement Specific Components

The system components described in this section are specific to the static pressure experiments undertaken as described in Chapter 7, and together with the permanent system components make up the full experimental system employed.

Pump to Airway Model Intermediary Connections

For measurements of upper airway pressures during natural breathing and breathing with NHF therapy flows it was desirable to condition the velocity profile of the flow from the pump. The profile of the flow exiting the lungs during expiration in live subjects was not known and, for the purpose of determining the pressures within the upper airway, it was not considered necessary to replicate it as the effects of the tortuous geometry would rapidly dominate. On inspiration, the flow profile is determined by the facial geometry surrounding the nares, which is faithfully replicated in the models. The upper airway is a complex geometrical structure linked to the lungs via the trachea, an approximately straight, circular passageway of approximately 25 mm in diameter and 120 mm in length (Tortora and Derrickson, 2006). The airway models used for experimentation were all made such that they began at the transition from the larynx to the trachea, that is, at the superior extremity of the trachea. Because of these factors it was assumed that a straight entrance to the upper airway would provide a flow from which the pressure characteristics within the upper airway could be

determined. To achieve this, a 550 mm (36 diameters) length of 15 mm inner diameter brass pipe was installed at the inferior entrance to the airway model via the aluminium connector previously described. The opposing end of the pipe was then connected to a TSI 4040 thermal anemometer flowmeter via a flexible tube fitting with an inner diameter of approximately 20 mm. The connection between the flowmeter and the pump was made by another short length of the same flexible tubing. The airway model was elevated on an angled platform so that all pressure tap positions could be accessed for measurement. An illustration of this system is given in Figure 15.

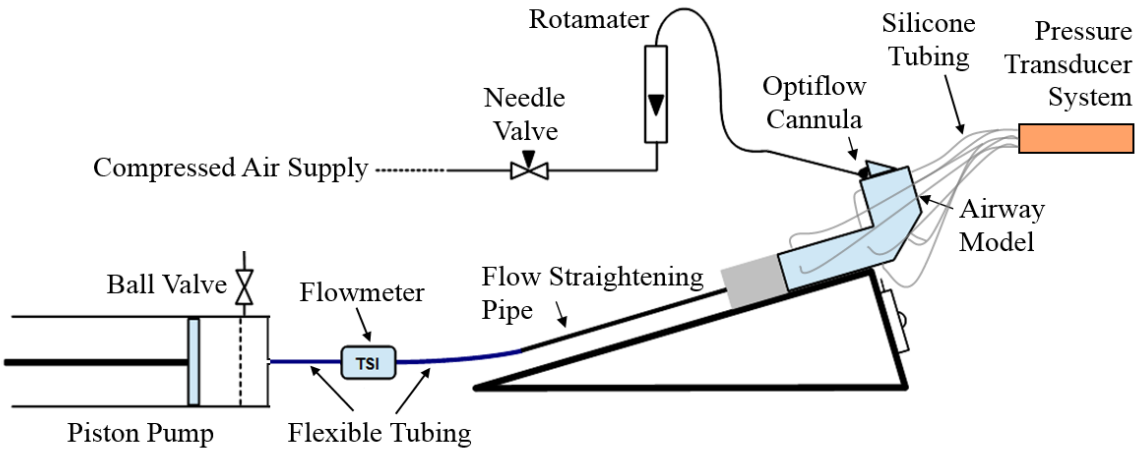

Figure 15: Schematic of the experimental system used for static pressure measurements.

Pressure Sensing Elements

A 32-port pressure transducing system, previously developed for static pressure measurements within these same airway models during constant flows, was employed for measuring the static airway pressures during oscillatory breathing flows. 32 Honeywell S&C differential pressure transducers with a sensing range of -2500 to 2500 Pa and a 0.1 Pa resolution were used within the system. Connecting the pressure sensors to measurement points in the airway models were lengths of silicone tubing with short sections of hypodermic tube at the open end. Each of these hypodermic tubes was inserted into a pressure tap hole within the airway model so that they terminated no further than 5 mm from the inner surface of the airway. The gap between each pressure tap hole and the hypodermic tube was sealed with Blu-Tack.

5.3 Turbulence Intensity Measurement Specific Components

The system components described in this section are specific to the turbulence intensity experiments undertaken as described in Chapter 8, and together with the permanent system components make up the full experimental system employed.

Pump to Airway Model Intermediary Connections

The components connecting the pump to the airway for turbulence measurements were the same as described for use in the static pressure measurements. The reasons for this are very similar to those above, with the velocity and turbulence attributes of the flow due to the geometry of the upper airway being of the greatest interest, and the turbulence of the flows exiting the lungs being unknown. The airway model was again supported on an elevated frame to allow access to the velopharynx for turbulence testing along an anterior to posterior traverse. A traverse slide with a clamp to hold the hot wire probe support was mounted to the frame at a right angle to the lay of the airway model, as shown in Figure 16. The traverse slide had a scale accuracy of 0.05 mm for accurate positioning of the hot wire probe within the velopharynx of the airway model. Both the positioning of the airway model and the traverse slide on the frame could be manually adjusted relative to one another to align the probe with the entrance hole into the model's velopharynx.

Flow Velocity and Turbulence Sensing Elements

A hot wire anemometry system was used for measuring the transient flow velocities and turbulence intensities within the velopharynx and at the external nares of an upper airway model. Three older hot wire systems; a DISA, a TSI and a third system previously developed in house; were initially trialled for use but all proved to be unstable. A new all-in-one system, the Dantec Dynamics multi-channel constant temperature anemometer (CTA) with hot wire calibrator and software, was purchased for these measurements. A Dantec Dynamics 55P11 straight miniature wire probe mounted in a 55H21 long straight probe support and connected to the multi-channel CTA with a 4 m coaxial cable was used for all measurements. Data from the probe was captured using the system software.

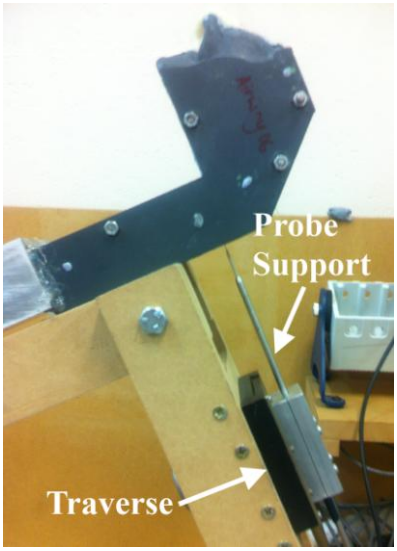

Figure 16: Traverse slide with probe support.

5.4 Carbon Dioxide Washout Measurement Specific Components

Over the course of this research two methods of determining the efficacy of anatomic dead space washout with the use of Optiflow™ NHF therapy were carried out. The first method implemented Experimental Method Version One, measured the decay of CO_2 concentration at a single measurement point. This was carried out by initially adding a known volume of CO_2 to the pump while at rest then beginning the breathing cycle and logging the concentration as it decayed. This method was not physiologically representative of the respiratory process but aimed to gain relative information on the efficacy of NHF therapy. The second method, Experimental Method Version Two, aimed to replicate the continuous process of respiration and determine an average concentration of CO_2 at a single point. This was achieved by measuring the CO_2 concentration over many breathing cycles while replicating CO_2 production in the lungs with a steady flow of CO_2 into the pump, in order to gain a temporal average of the CO_2 concentration. Certain components of the system varied between each of these two methods, however the same method of introducing the CO_2 to the pump was employed for both. All are described below and, where the system components were unique to a method, they are denoted as Version One or Two for first and second methods respectively.

5.4.1 Carbon Dioxide Feed

A 6 mm diameter inlet into the top of the pump cylinder, positioned near the pump outlet and gated by a manual ball valve, allowed an entry point for the introduction of CO_2. Through this inlet a small bleed of CO_2 could be fed into the lung volume for CO_2 washout measurements, doping the air within

to a known concentration and thus replicating the diffusion of CO_2 into the lung which occurs during pulmonary respiration. The CO_2 gas of purity greater than 99.8% was supplied from a compressed gas cylinder. Before entering the pump volume the CO_2 passed through a Norgren pressure gauge following which the flow rate was metered to the desired level via a King Instruments 7430 series low flow rotameter. Because the rotameter was not new a check on its calibration was carried out. The rotameter was connected to a low flow rate air supply at its inlet and its outlet was fed into a TSI 4140 low flow thermal anemometer flow meter by a short length of tube, to prevent significant pressure losses. Readings on both meters were taken for comparison at 10 ml/min intervals over the 0 to 100 ml/min range of the rotameter. Analysis of the readings from the two different flow meters showed that the rotameter was reading high at all points. The relation between the two flow meters, however, had a strong linear trend which could be used to correct for the rotameter's calibration error.

As the rotameter was made to meter flows of air, a conversion factor had to be applied to the desired flow rate of CO_2 to account for the difference in density to determine the equivalent rotameter scale reading. This factor, called the gas correction factor (GCF), is defined by King Instruments as follows in Equation [1] and is dependent on the gas specific gravity, g_{sp}, temperature in Kelvin, T, and the operating back pressure in PSIG, p.

$$GCF = \sqrt{\frac{g_{sp} \times (T + 460)}{36 \times (p + 14.7)}} \qquad \textbf{[1]}$$

By multiplying the desired flow rate of CO_2 by this GCF, and then correcting this flow value for the rotameter's calibration error, the scale reading required to give a CO_2 flow desired could be found. As the GCF has a small dependence on temperature it was calculated on each day of testing to account for daily variation.

5.4.2 Experimental Method Version One Specific Components

The system components described in this section are specific to the CO_2 washout experiments undertaken using Experimental Method Version One as described in Chapter 9. Combined with the CO_2 feed described above and the permanent system components these elements make up the full experimental system employed.

Pump to Airway Model Intermediary Connections

As the purpose of this method was to measure the rate of CO_2 concentration decay and how this was affected by Optiflow™ NHF, it was not imperative that the system accurately replicated the respiratory system. As such much of the initial system setup, including the original pump form with

the cone exit and many industrial connections, was employed. As for the pressure and turbulence measurements, the pump was connected to the airway via a series of flexible tubing and a straight pipe; however, in this system another flexible tube was added to the system to allow for the inclusion of the carbon dioxide sensor. This is illustrated in Figure 17.

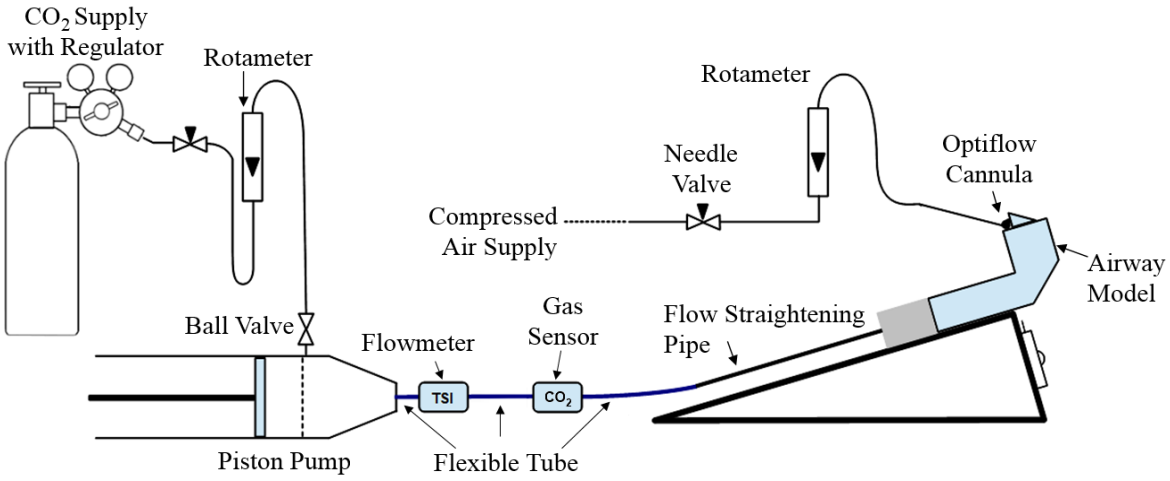

Figure 17: Schematic of Experimental Method Version One experimental system.

Carbon Dioxide Sensing Element

As the measurement of CO_2 concentration decay was not representative of a physiologically realistic phenomenon, it was decided the level of CO_2 concentration added to the model for measurement could be any detectable amount which would not cause a safety risk to those in the vicinity of the experiment. This measurement method was also to be an initial foray into the detection of gas concentrations in the experimental system, and a means of developing an accurate method for measuring CO_2 washouts in vitro. For these reasons it was concluded that low cost was a principal requirement in the gas sensor selection process. Also of high importance was the sensor sampling rate, response time, ease of calibration and accuracy. The period of the breath flow wave to be employed for these measurements was 5.08 seconds thus a sampling rate less than this was desired. As the decay rate of the CO_2 was yet unknown it was uncertain what response time would be adequate for the measurements.

From these criteria the GE Telaire Ventostat T8041, an optical CO_2 sensor designed for monitoring air duct concentrations, was selected as it had the best measurement range, sampling rate, response time and accuracy of the sensors in the low-price range considered at the time of purchase. Calibration of the sensor was completed in the factory with no other calibration required over the sensor lifespan of 15 years. The most important specifications of the sensor are listed in the following Table 2.

Table 2: Details of the GE Telaire Ventostat T8041 CO_2 sensor.

Cost	Measurement Range	Sampling Rate	Response Time	Accuracy
$436.59 (NZD)	0 - 2000 PPM	0.5 Hz	3 minutes (For 90 % step change at low flow speeds)	± 40 PPM + 3 % of reading

The sensing element of the Ventostat is located within a cylindrical probe limb with a diameter of 31.5 mm, too large to introduce directly into the connections between the pump and airway which were all approximately 20 mm in diameter. Two sets of perforated holes each covered a small, square area along the length of the probe allowing air to access the sensing element. To incorporate the sensing element of the Ventostat into the system, the limb was mounted perpendicularly to a piece of straight tube, 22.5 mm in diameter, so that the two intersected by a short depth with the tube passing across one set of perforated holes. The second set of perforated holes which lay exterior to the flow path was sealed. The tube could then be fitted in line with the connections between the pump and the airway, as illustrated in Figure 18.

Figure 18: Incorporation of Ventostat T8041 CO_2 into experimental system.

5.4.3 Experimental Method Version Two Specific Components

The system components described in this section are specific to the CO_2 washout experiments undertaken using Experimental Method Version Two as described in Chapter 9. Combined with the CO_2 feed described above and the permanent system components these elements make up the full experimental system employed.

Pump to Airway Model Intermediary Connections

As mentioned in the pump description, accurate replication of the human respiratory system volume was important for the measurement of the CO_2 washout using the temporal averaging method. The

geometry of this volume, particularly the separation of the anatomic dead space volume from the lung volume, was equally important as it was found that with the original pump cone outlet and step down connections containing some of the FRC the CO_2 profile at the airway model nares deviated significantly from that of a live subject. With the new flat plate ended pump design all system components outside of the pump; that is the airway, sensing elements and connections; made up the entire volume of the anatomic dead space. Between the airway and the pump the small amount of remaining dead space volume consisted of two consecutive gas sensor connections from the pump followed by a short length of straight 22.5 mm inner diameter tube attaching to the airway model. This is shown in the schematic of Figure 19.

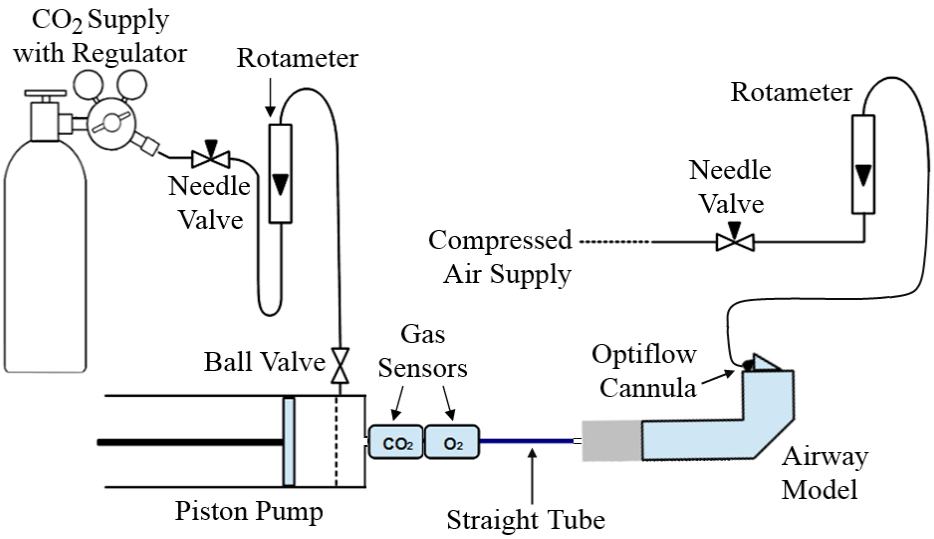

Figure 19: Schematic of Experimental Method Version Two experimental system.

As the average anatomic dead space volume is commonly stated to be 150 ml for an adult (Tortora and Derrickson, 2006) the intermediary connections were made so that their volume when combined with the volume of the upper airway model would total 150 ml. As mentioned at the beginning of this chapter, airway 06B was used as the standard upper airway model for experiments and as such the intermediary connections were made to suit the volume of airway 06B. The four other unique upper airway models had volumes which varied slightly as given in Table 1 in Chapter 4; however, as this was a result of natural variance in airway geometry it was considered acceptable to maintain the same intermediary connections for all when investigating the difference in Optiflow™ NHF efficacy as a result of upper airway variation. If the volume of each model were to have an influence on the efficacy of the therapy then this could be deduced from the results obtained.

Carbon Dioxide and Oxygen Sensing Elements

For the second CO_2 washout measurement method the system was used to replicate the physiological process of respiration, including the level of CO_2 gas exchange within the lungs. Subsequently, a gas sensor capable of measuring CO_2 levels over the range of 0 to 5.2% was required (Tortora and Derrickson, 2006). As for the previous sensor, a sampling rate of less than the breath period (4.29 seconds for the new average person breath wave to be used) was also of high importance. As this sensor needed to capture the variation in CO_2 concentration over the breath wave it was also desirable for its response time to be less than period of the breath wave. Again the sensor cost, accuracy, and ease of calibration were also prominent considerations.

From the sensors available within the budget at the time of purchase, a TDS0054 carbon dioxide optical sensor by Dynament was selected. This sensor was one of the only available within the range of the budget which met the measurement range requirements. Of these few it provided the best response time, sampling rate and accuracy. The sensor came pre-calibrated with a calibration check required after one year. A Senko SS1118 electrochemical O_2 sensor with similar specifications was also purchased at the same time for use as a reference during testing. The notable specifications for each sensor are given in Table 3 and pictures of the sensors can be seen in Figure 20.

Table 3: Details of the Dynament TDS0054 CO_2 sensor and the Senko SS1118 O_2 sensor.

Sensor	Cost	Measurement Range	Sampling Rate	Response Time	Accuracy
CO_2 Dynament TDS0054	$875.15 (NZD)	0 - 100 %V/V	Up to 4 Hz	<30 seconds (For 90 % step change)	± 2 % of full scale reading
O_2 Senko SS1118	$325.45 (NZD)	0 - 99 %V/V	-	≤ 10 seconds	± 0.5 %

(a) **(b)**

Figure 20: Gas sensors (a) Dynament TDS0054 CO_2 sensor; and (b) Senko SS1118 O_2 sensor.

As shown in Figure 20, both the O_2 and CO_2 sensors were cylindrical and, as both had a 20 mm diameter, were easy to mount in line with the pump to upper airway model connections. To hold each sensor in line with the flow at its perimeter, identical plastic connections were designed and 3D printed. These connectors, pictured in Figure 21, were formed with tapers on each end, one external and one internal, so they could be easily joined to other standard connections in use. The openings for the sensors also had a slight taper to give a push fit for sealing and accurate placement of the sensor within the flow.

Figure 21: Connectors for integrating CO_2 and O_2 sensors into the flow path of the Experimental Method Version Two system.

These connectors provided a mounting for the two sensors allowing them to be incorporated into the experimental respiratory system at the outlet of the piston pump as illustrated in Figure 19.

6 Breath Pattern Development

To provide an accurate representation of a human respiratory system a breathing pattern which replicated the form of an in vivo natural breath flow wave was desired. As described in the background theory there are two major components to the breathing pattern, the tidal volume and the respiratory rate. The form or shape of the breathing pattern itself is not symmetrical across inspiration and expiration due to the active and passive mechanisms of each respectively. A simple sinusoid waveform does not replicate this, thus in vivo breath pattern data acquired in previous research were used to form the flow patterns to drive the pump. The natural breathing pattern of a healthy 23-year-old male subject, 84 kg with a BMI of 24.6, was captured at a rate of 100Hz by a TSI-4040 flow meter attached to the outlet of a full face mask worn by the subject. Further breathing patterns of the subject were captured while receiving a range of NHF therapy levels with the Optiflow™ cannula worn underneath the mask. The applied flow rates of the Optiflow™ NHF, ranging from 10 to 50 LPM at intervals of 10 LPM, were subtracted from the captured data to extract the lung's contribution to the flow. The final breathing flow rate results from these measurements are shown in the Figure 22 plot where positive values show expiration and negative inspiration.

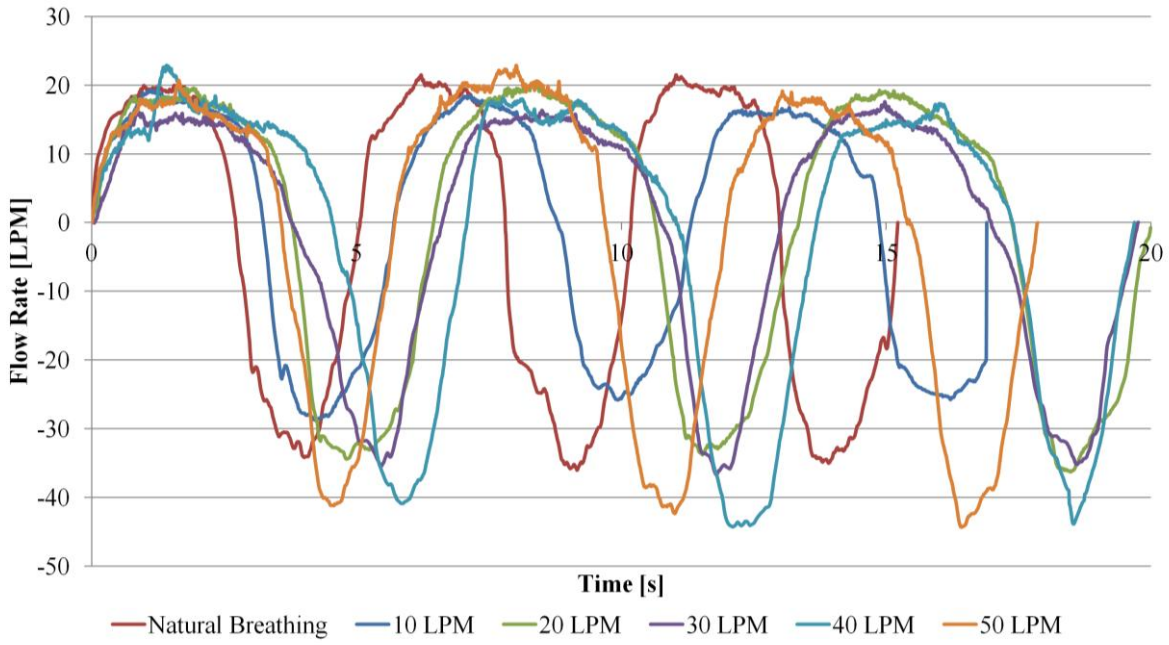

Figure 22: In vivo breathing flow rates as measured from male subject while breathing naturally and with various levels of NHF therapy.

This plot shows distinguishable changes to both the respiratory rate and the peak inspiration and expiration values with the use of Optiflow™ NHF therapy. A decreasing trend in the peak inspiration flow rate occurs with increasing levels of NHF, resulting from the assistive NHF flow. The increased

resistance to expiration from this flow also results in an increase in the period of each breath with increasing NHF flow rates.

Initially these variations of the breathing pattern with varying NHF flow rates were considered an important aspect of the respiration characteristics which should be included in the experiments. The first sets of CO_2 dead space washout experiments carried out using Experimental Method Version One were therefore done so with the breath flow wave provided matching the level of NHF therapy being administered. However, after further progression of the experimental system it was decided that the extent to which these variations occurred was most likely patient dependent like many other factors. Similarly, the in vivo measurements from which the breathing patterns were derived were performed on a healthy subject unlike the patients who usually receive Optiflow™ NHF therapy as they are experiencing some level of respiratory distress. Therefore it was decided that using a single breath wave pattern for all subsequent experiments would eliminate one variable, allowing for data measurement from which the effects of the NHF on flow and wash out characteristics alone could be determined. The natural breathing pattern was chosen for this purpose.

At the same time as the decision was made to use the natural breath pattern for all future experiments, the magnitude of the tidal volume and respiratory rate were scrutinised. The tidal volume of the original natural breathing pattern, at 799 ml, was found to be above the average accepted value of 500 ml although the respiratory rate was close to the standard 12 breaths per minute at 11.8 (Tortora and Derrickson, 2006). The greater tidal volume may in part be attributed to the method of measurement, as wearing the face mask with the attached flow meter effectively increased the subject's dead space volume. Tobin et al. (1983) studied the breathing patterns of 65 adult subjects without altering the dead space volume and found an average respiratory rate of 16.6 breaths per minute and an average tidal volume of 383 ml. The difference in their measured tidal volumes and respiratory rates to the accepted average values were attributed to the experimental methods of previous studies in which dead space volume was added to the subjects by introduction of measurement equipment (Tobin et al., 1983). When these factors were taken into consideration, it was concluded the original natural breathing pattern was not a faithful representation of an average adult and the pattern should be scaled down to do so whilst retaining a realistic form. Values of tidal volume and respiratory rate between those commonly accepted and those found by Tobin et al. (1983) were chosen, at 450 ml and 14 breaths per minute respectively. This provided an 'average' or representative adult breathing pattern with a realistic waveform which was used for all experiments except the initial CO_2 dead space wash out, Experimental Method Version One, and the measurements of turbulence intensity at the external nares. A comparison of the original natural breathing breath wave and the same breath wave scaled to the 'average' tidal volume and respiratory rate are shown in Figure 23.

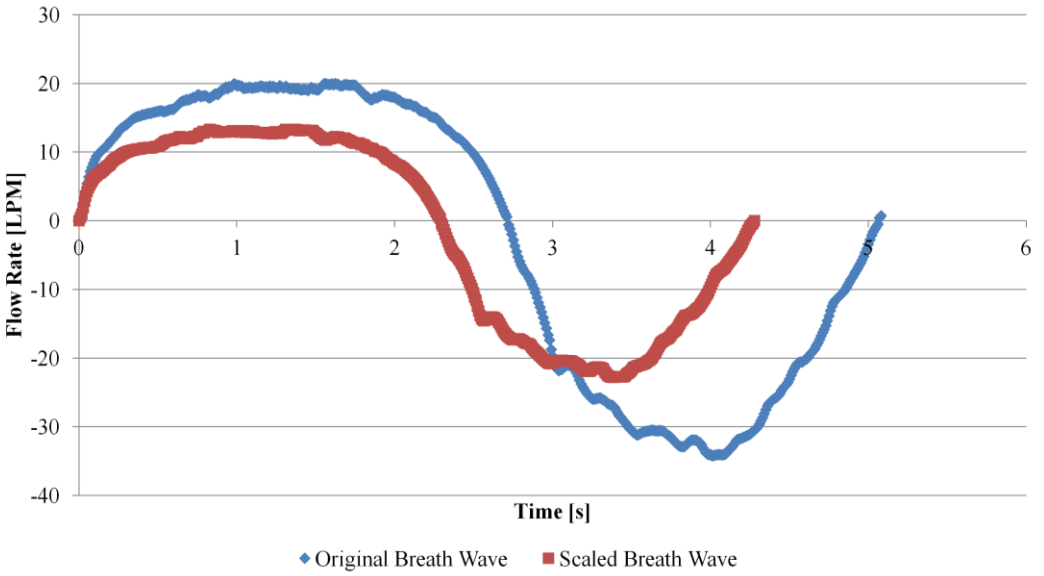

Figure 23: Comparison of the original natural breathing breath wave as measured in vivo and the wave scaled to an average 450 ml tidal volume and respiratory rate of 14 breaths per minute.

To convert the breathing data into a usable form to drive the pump, each set of data was phase averaged over twenty breaths and then converted into Fourier series. Conversion was done in Matlab by conducting spectral estimation on each breath pattern, followed by fitting of the strongest frequencies to a Fourier series from which the coefficients were extracted. A five coefficient Fourier series was determined for each set of breathing data. This was done for all breath waves employed throughout this research. This method provided close approximations of the measured data as shown in Figure 24 which gives a comparison of the 'average' natural breathing pattern to the Fourier series extracted from the same data.

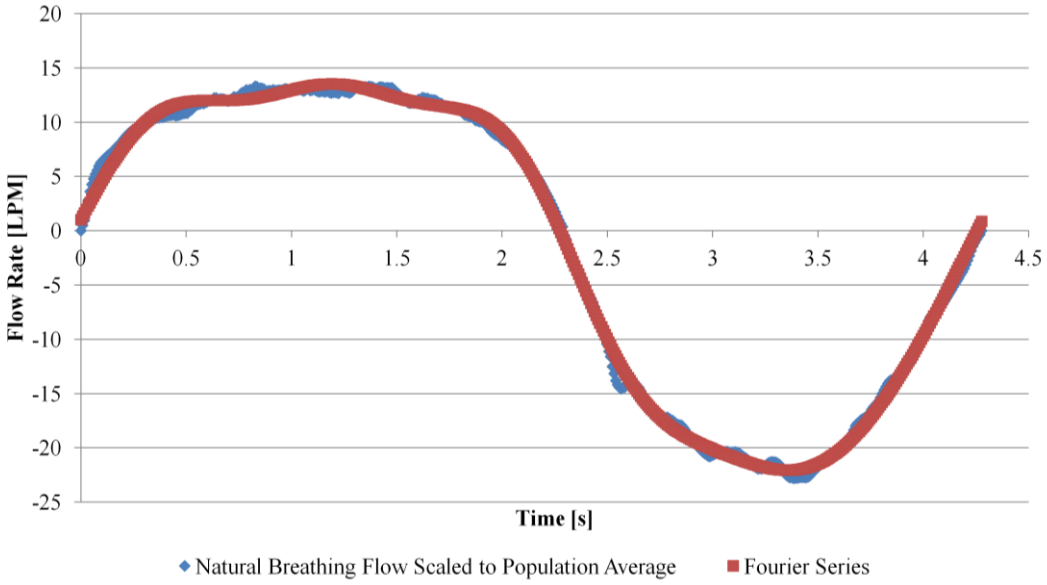

Figure 24: Fourier series breath wave compared to the scaled natural breathing breath wave.

7 Static Pressures in the Upper Airway

Prior research with the five early upper airway models employed in this research has identified that loss of pressure occurs in the upper airway when constant flow rates are used in place of oscillatory breathing flows. The static pressure results of these steady state experiments are shown in the Figure 25 plot for the case of constant 20 LPM expiration flow through each of the five airway models. The pressure loss is a result of the airway resistance and is dependent on the geometry of the individual's upper airway. Viscous pressure losses occur due to friction at the airway walls while sudden changes in airway cross section induce flow separation resulting in further losses in pressure. Within the oropharyngeal region large changes are seen in the cross-sectional area due to protrusion of the uvula and epiglottis thus high losses in pressure are expected to be observed.

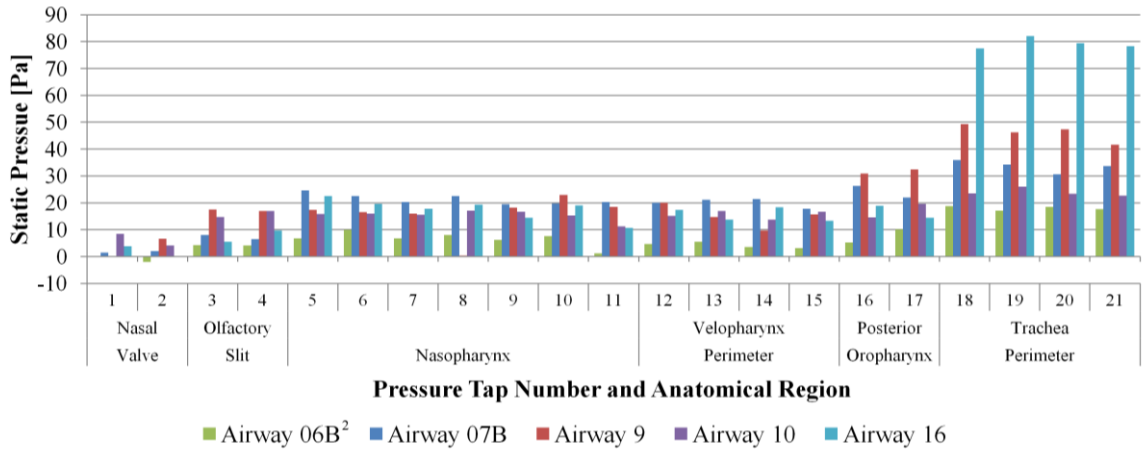

Figure 25: Static pressures observed during previous research in the five original airway models during steady-state experiments using a constant expiration flow rate of 20 LPM (adapted from Cressy et al. (2011)).

The resistance to inspiration is believed to be reduced with the use of NHF therapy as a result of the NHF flow rate meeting or exceeding the peak flow rates required by the lung expansion. This subsequently reduces the work of inspiration, and is noted as the second mechanism of action for NHF therapy by Dysart et al (2009). This would be observed as an increase in static pressure within the upper airway during inspiration with increased levels of NHF therapy. It has previously been found that during inspiration healthy, live subjects experience an increase in resistance due to the distensibility of the nasopharynx and the vacuum pressures of inspiration resulting in a decrease in airway patency (Shepard and Burger, 1990). Due to the rigidity of the models used in these experiments the occurrence of this phenomenon and its effects were not observed; however, as NHF is expected to increase pressures, thus reducing the forces which act on the airway walls to reduce patency and increase flow resistance, any reduction in resistance observed in vitro will be conservative. Similarly, the point at which inspiratory work drops to zero with the NHF flow fully

fulfilling the peak flow requirements will be the same as it would be in a compliant model. Measurements of the static pressure at numerous positions within the upper airway were undertaken to determine the influence of the use of Optiflow™ NHF therapy. These measurements were also utilised later to draw conclusions about the relationship between airway pressures and CO_2 dead space wash out.

Dysart et al. (2009) postulated that the positive airway pressure induced by the flow of NHF provides a distending pressure to the lungs and consequently improves lung recruitment, listing this as the fifth mechanism of action. Due to the rigid nature of the experimental system, in particular the lung pump, this affect cannot be investigated; instead the pressure losses and generation of positive airway pressure due to NHF therapy within the rigid airway region are explored.

It is thought that the pressure loss observed in the pharynx is an indication of the presence of turbulence, which is believed to have positive effects on dead space wash out by promoting mixing. A decrease in airway pressure during inspiration and an increase in airway pressure during expiration may then be the result of an increase in the level of turbulence. Measurements of pressure in the airway, particularly those surrounding the velopharynx, were also later compared to the results of turbulence intensity measurements across the velopharynx cross section.

7.1 Experimental Procedure

To measure the behaviour of the static pressures within the upper airway during oscillatory flows data was collected at 21 different positions over many cycles for both natural breathing and breathing with Optiflow™ NHF. The standard airway 06B model was employed and the experimental respiratory system was prepared as described in Chapter 5. The regions of the upper airway and static pressure measurement positions, focusing predominantly on the pharynx, are shown in Figure 26.

Before starting the experiments the pressure sensors were zeroed. The pump was run with the average adult breath flow wave, with 450 ml tidal volume and respiratory rate of 14 breaths per minute. The experiments were conducted for natural breathing and breathing with Optiflow™ NHF flow rates from 10 to 70 LPM in 10 LPM increments. Measurements of the static pressure at all 21 points were simultaneously collected for a period of five minutes at a rate of 100 Hz, with data collection commenced at the onset of an expiration.

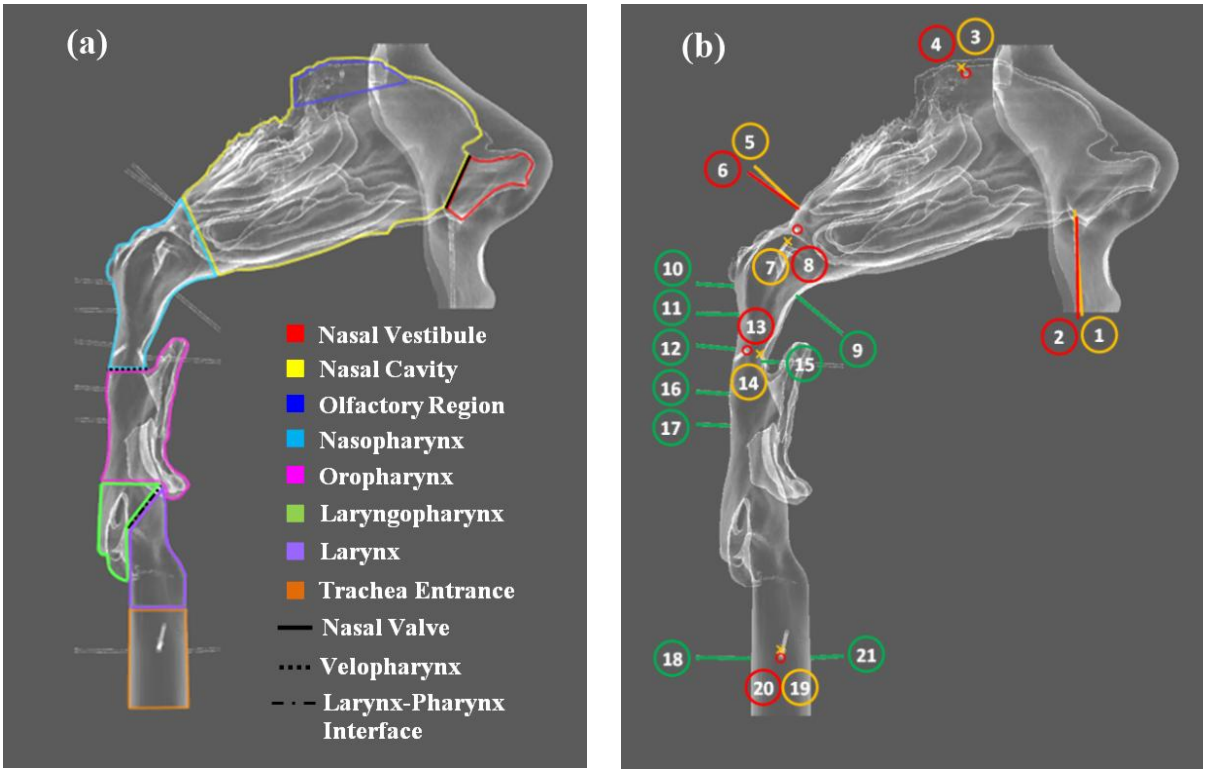

Figure 26: Right side views of airway 06B silhouette showing (a) regions of interest in the upper airway; and (b) pressure taps locations where lines normal to airway surface show posterior, anterior, inferior and superior taps while crosses and circles mark lateral taps. Lateral and side-by-side taps are coloured red and yellow to indicate right and left positions respectively.

7.2 Data Processing

As the raw pressure data collected contained some noise, an average transient static pressure profile over a single breath period was extracted by phase-averaging 20 cycles of data together. By splitting the breath cycle period into a discreet number of phase points, the values of pressure at each phase could be averaged together. As the breath wave period was not a multiple of the data collection frequency, a linear interpolation method was used to estimate the static pressures at each phase. Subsequent to data collection it was discovered a number of the cycles in each dataset had been clipped. Consequently it was necessary to manually check each set of data and extract 20 full cycles for phase-averaging. The beginning of each full cycle was determined by manual identification of the minimum flow rate prior to expiration onset from the simultaneously acquired pump flow data. Matlab was then employed to carry out the phase-averaging process. This produced smooth profiles of the large-scale transient pressures occurring at each of the measurement positions over the course of a breath cycle.

7.3 Results and Discussions

The experimental results described following are separated into two sections, the natural breathing results and the results of breathing with NHF therapy.

7.3.1 Natural Breathing

During natural breathing the static pressure at each point of measurement within the upper airway has a form similar to that of the breath flow wave. Positive pressures were measured during expiration and conversely negative pressure during inspiration. Overall the pressure wave appears in phase with the flow wave as illustrated by the results from a single measurement position in Figure 27; however, throughout the transition from expiration to inspiration the pressure lags the flow wave, in particular during the steep acceleration to peak inspiration. This is also shown in Figure 27 where it can be seen that the inspiration portion of the breath cycle is shorter than expiration and achieves higher peak flow rates, thus the steeper curve.

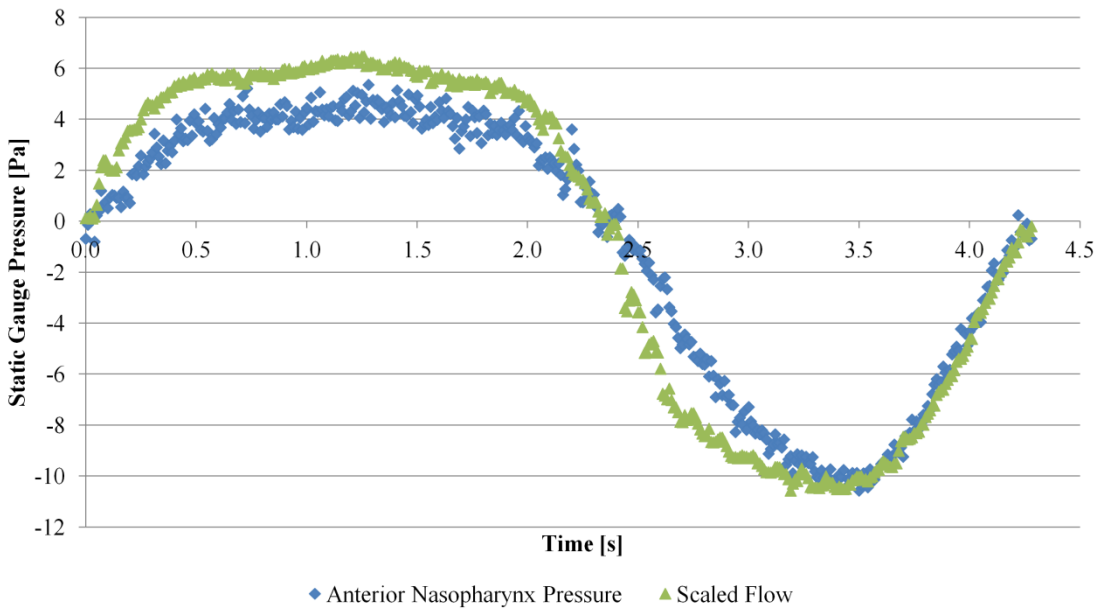

Figure 27: Transient static pressure at the anterior nasopharynx and scaled flow rate during natural breathing showing pressure lagging flow at the drop to peak inspiration. Flow rate scaled by a factor of 0.479 Pa/LPM.

In general the absolute magnitudes of peak expiration and inspiration pressures increase as the measurement points move towards the lungs, though some local decreases in magnitude are also seen. This result is indicative of the airway resistance that opposes the flow and causes pressure loss between the lungs and the external nares. The presence of airway resistance contributes to the work of breathing, with greater effort required to breathe for greater levels of resistance.

The transient static pressures at the superior nasopharynx follow a profile very similar in form to the flow rate curve with very close agreement between the ratios of peak inspiratory to expiratory values. This is illustrated in Figure 28 in which the flow rate curve has again been normalised by the peak inspiratory pressure for ease of comparison. This indicates that the pressure drop across the nasal cavity between the external nares and the point of measurement is related to the flow rate by a similar factor for both expiration and inspiration. Specifically, this implies that the flow resistance within the nasal cavities is similar in both flow directions, agreeing with the steady-stated in vitro findings of Croce et al. (2006). As previously mentioned, in vivo research has shown that in live subjects an increase in resistance is seen during inspiration due to the compliance of the nasal vestibule and later the nasopharynx (Shepard and Burger, 1990). This highlights a limitation of the use of rigid airway models as deformation of the airway is prevented and this change in resistance during inspiration is not replicated in the results.

At the superior trachea the flow rate and pressure ratios of peak inspiratory to expiratory values do not show the same agreement seen at the superior nasopharynx. This is shown in Figure 29 where the flow rate curve has been normalised by the peak inspiratory pressure as before. From this result it can be deduced that there is a slightly greater resistance to flow across the entire upper airway during inspiration than during expiration.

Between the superior nasopharynx and the trachea there is a large pressure drop during inspiration as illustrated by the plot of the peak static pressures at all measurement points in Figure 30. This drop begins as the cross-section of the airway decreases toward the minimum cross section at the velopharynx. Past the velopharynx a large irregular cavity appears on the anterior wall formed by the uvula, tongue and epiglottis in superior to inferior order. Another cavity is formed at the inferior region of the laryngopharynx below the anterior opening to the larynx. The superior of these cavities causes an expansion of the pharynx cross-section in both expiration and inspiration directions, however only expiration flow experiences a slight pressure recovery at this cross-section widening, whilst a slight drop in pressure is seen for the inspiration flow. Inspiration pressures have an overall downward trend along the flow path while in comparison expiration shows large drops in pressure with frequent recoveries.

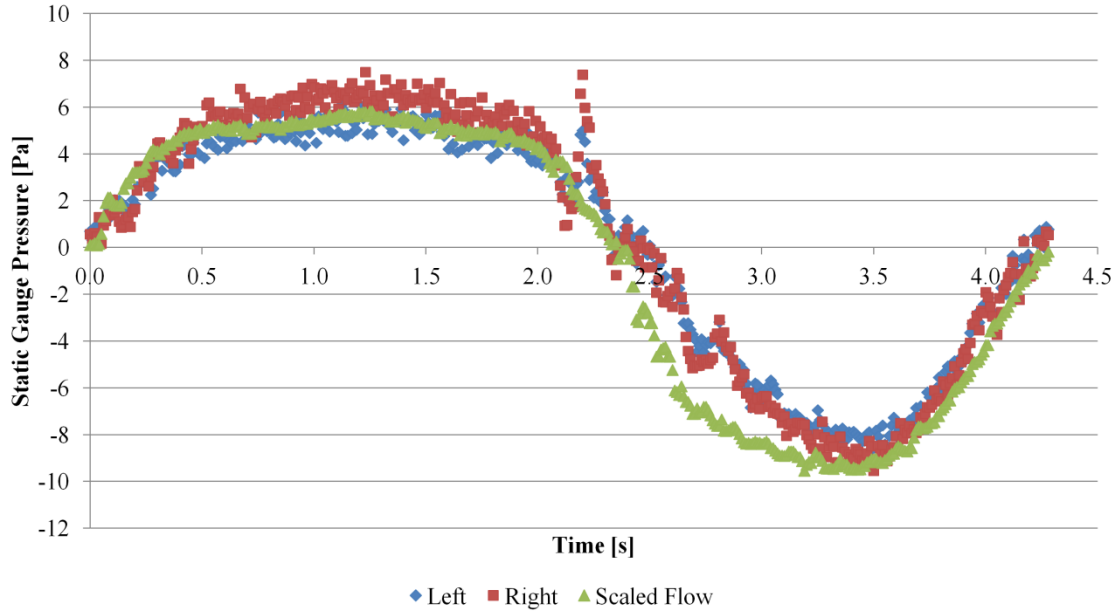

Figure 28: Transient static pressures at the superior nasopharynx during a natural breathing cycle showing close agreement in peak magnitudes to the normalised flow rate. Flow rate scaled by a factor of 0.432 Pa/LPM.

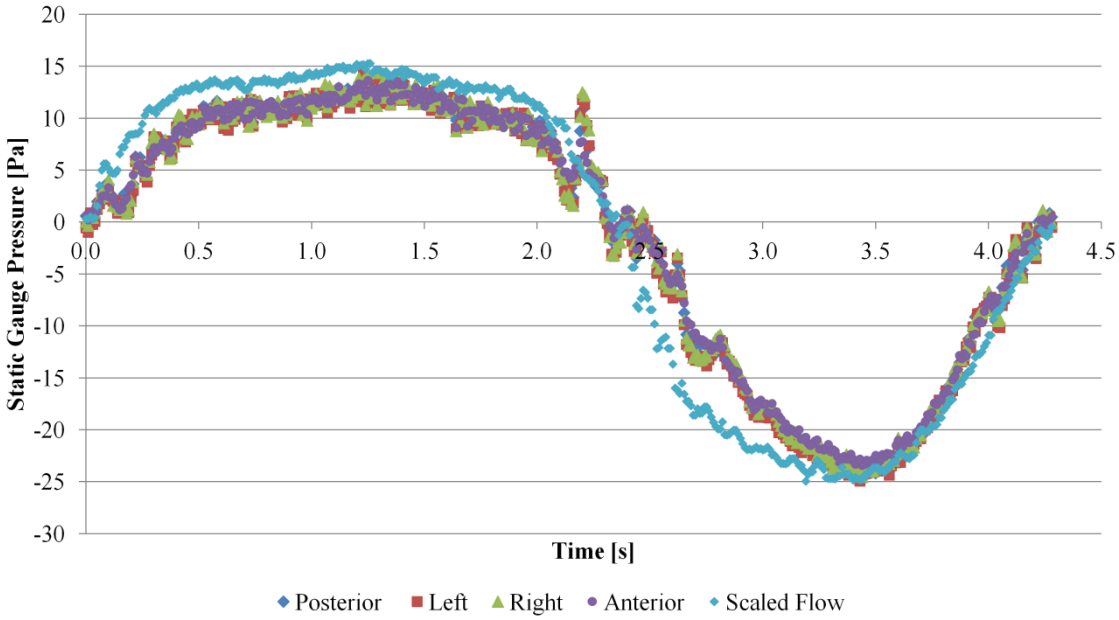

Figure 29: Transient static pressures at the perimeter of the superior trachea during natural breathing in comparison to the flow rate scaled by a factor of 1.130 Pa/LPM.

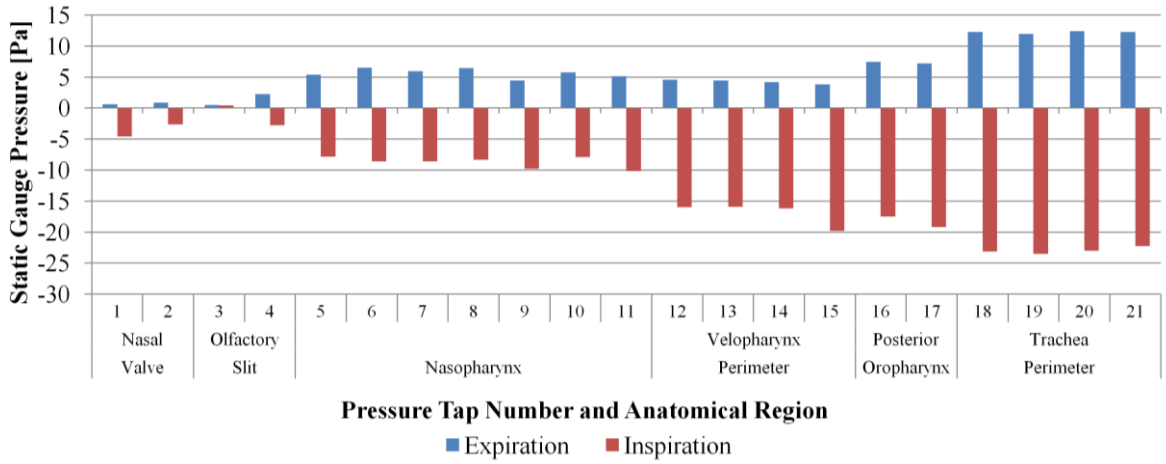

Figure 30: Expiration and inspiration peak static gauge pressures at every pressure tap location with anatomic regions labelled.

In the same region between the superior nasopharynx and the trachea the pressure drop experienced during expiration is significantly lower relative to the flow rates achieved. While the nasopharynx to laryngopharynx region causes large losses during peak inspiration, the losses during peak expiration are not equivalent as shown previously in Figure 30. Research by Stringer et al. (2010) which simulated steady state flow within the same airway showed that during peak expiration the flow is directed from the anterior opening of the larynx into the pharynx, illustrated in Figure 26 (a), in a superior-posterior direction as given in Figure 31 (b). The flow path is jet-like within the pharynx and has little interaction with the two large cavities, unlike the flow path during peak inspiration in Figure 31 (a) which shows streamlines more evenly spread across the pharynx cross section and interaction with both cavities. This difference in the flow distribution across the pharynx gives some explanation as to the differences seen in the pressure losses. As the flow passes from the velopharynx into the inferior nasopharynx during expiration there is a small recovery of pressure due to the smooth expansion. This is shown in Figure 32 by the increase in the expiration curve peak between the velopharynx and inferior nasopharynx.

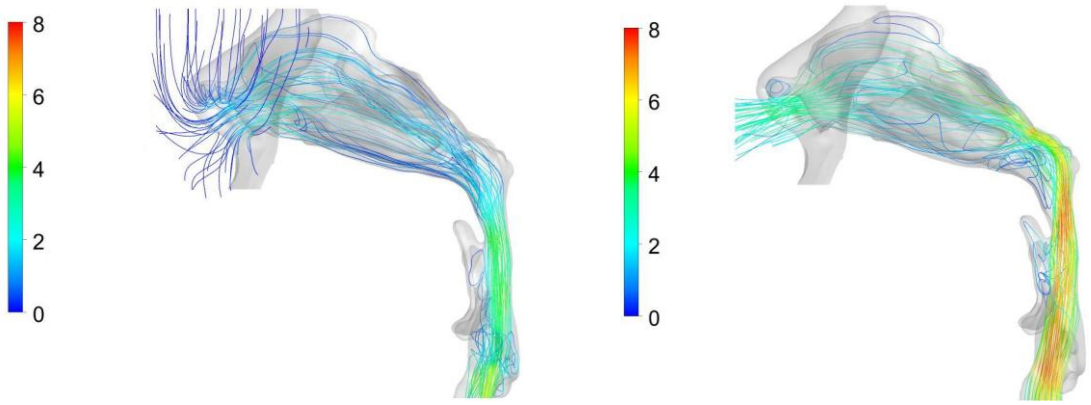

(a) **(b)**

Figure 31: CFD results of steady state flows through airway 06B showing streamlines in m/s for (a) peak inspiration flow of 22 m/s and (b) peak expiration flow of 32 m/s (adapted from Stringer et al. (2010)).

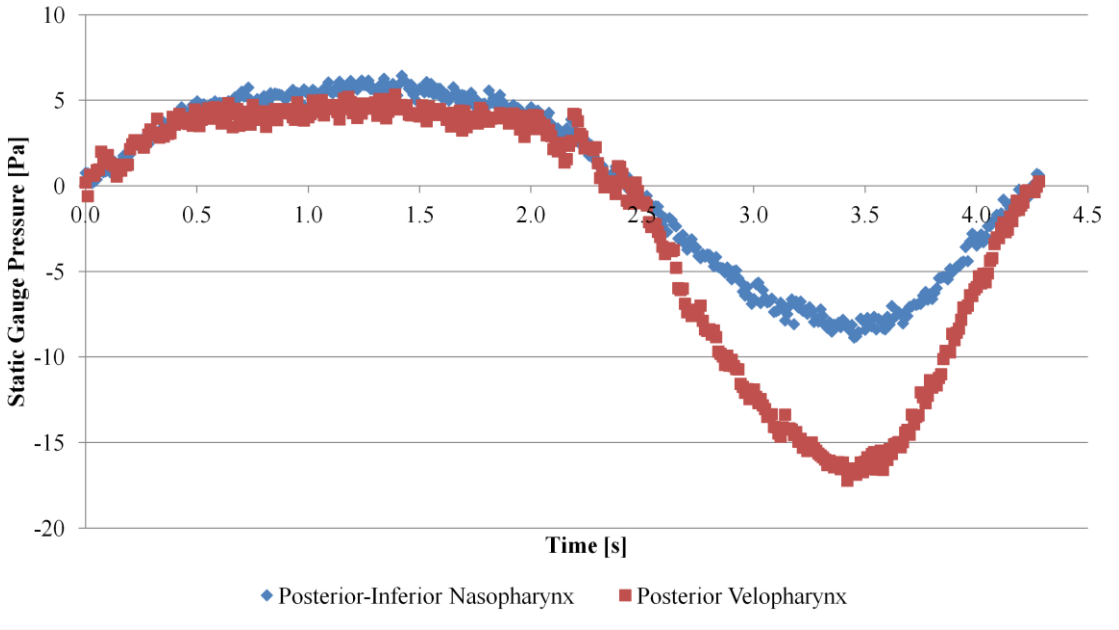

Figure 32: Transient static pressures at the posterior velopharynx and posterior-inferior nasopharynx showing small recovery of pressure during expiration.

7.3.2 Breathing with Optiflow™ NHF Therapy

With the introduction of NHF therapy the transient static pressure profiles are seen to move upwards on the vertical axis in the positive pressure direction. The mean, peak expiration and peak inspiration static pressures become more positive with increasing levels of NHF therapy. An example of this is given in Figure 33 which shows a plot of the transient static pressures at one of the superior trachea measurement positions for all levels of NHF. At this position, the most inferior measurement point in the upper airway model, the inspiration peak static pressure first crosses the horizontal axis into the positive pressure region for a NHF flow rate of 30 LPM. This implies that with a NHF flow rate of 30 LPM the upper airway resistance to flow during inspiration is fully compensated for by the inward flow of air supplied by the NHF therapy. Therefore at this flow rate the work required to draw air from the external nares to the trachea entrance would be fulfilled by the NHF therapy, reducing the overall inspiratory effort required by the lungs. This is in line with the second theory from Dysart et al. (2009) that by providing flows equal to or in excess of the peak inspiration flow rate, in this case 22.1 LPM, the airway resistance is fully compensated by the NHF. For the maximum flow rate tested of 70 LPM the mean static pressure at the trachea measurement position in Figure 33 had increased from 0 to 300 Pa (gauge). The increase in the peak static pressure of expiration however shows that there is increased resistance to flow out of the lungs. In live subjects this increased resistance would at some NHF level surpass the physical effort which can be provided by the passive elastic tension of the lungs and internal intercostal muscles and expiration would necessarily become an active process instead of a passive one. The point at which this would occur cannot be the determined from these

results as the elastic properties of the lungs were not replicated in these experiments, nor is the resistance of the conducting airways below the upper airway known. The effect of this increased expiratory resistance is of interest as persons suffering from COPD and other respiratory diseases who may receive Optiflow™ NHF therapy as a treatment often have increased airway resistance or reduced lung elasticity as a result of their condition. Therefore it is likely that there is a point at which increasing the NHF flow rate further has a detrimental effect rather than a positive one.

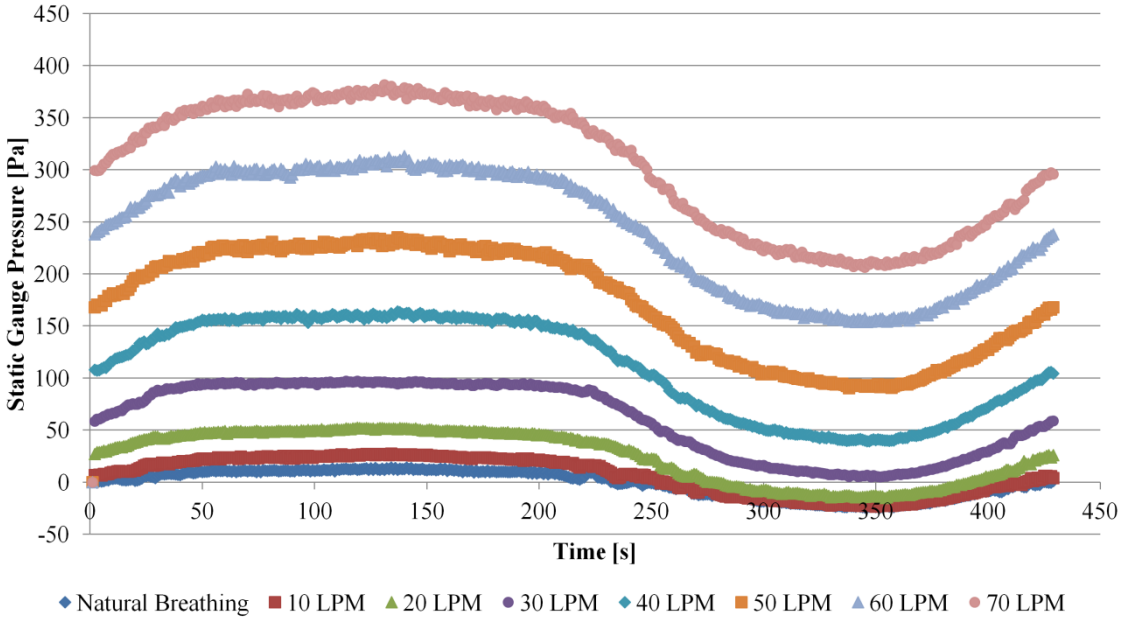

Figure 33: Transient static pressures at the posterior-superior trachea for natural breathing and all Optiflow™ NHF flow rates showing increase in mean, peak expiration and peak inspiration pressures with increasing NHF flow rates.

The increase of the peak and mean static pressures with increasing levels of NHF can also be seen in Figure 34. This gives a plot of the averages of mean, peak inspiration and peak expiration static pressures measured at the four trachea pressure taps as a function of the NHF flow rate. All three can be closely approximated by a second order polynomial. The peak inspiration and expiration curves are divergent within the range of tested NHF flow rates, with the difference between the peaks becoming greater with increasing NHF levels. This implies that within this NHF range the expiratory resistance grows at a faster rate than the inspiratory resistance declines. In other words the beneficial effects of Optiflow™ NHF therapy during inspiration develop more slowly than the detrimental effects during expiration with increasing therapy flow rates.

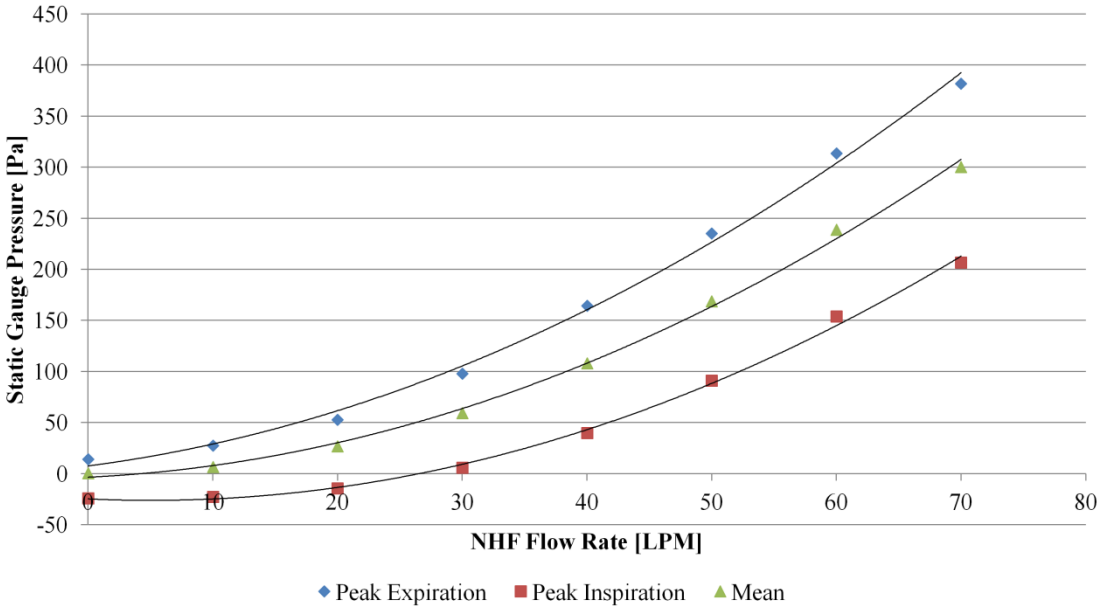

Figure 34: Plot of peak expiratory, peak inspiratory and mean static pressures at the trachea measurement locations for natural breathing and all NHF flow rates with second order polynomial fits.

As the general form of the pressure wave remains the same with increasing levels of NHF, an attempt was made to design an equation by which the natural breathing pressure wave could be adjusted to approximate the pressure wave at any level of NHF therapy. The second order polynomial fit from the Figure 34 plot was used calculate the mean position of the static pressure wave. A power relation of the form $y_{NHF=x} = y_0 A x^b$ was employed to describe the static pressure at each phase position as a function of the natural breathing pressure at the same phase, y_0, and the NHF flow rate, x. It was found that the static pressure relationship to the NHF flow rate was not linear but rather a power where a value b = 0.65 provided the best fit. As expiration and inspiration peaks grow at different rates, the constant *A* was assigned two values of 0.33 for expiration and 0.28 for inspiration. The equation is therefore:

$$y_{NHF=x} = y_0 A x^{0.65} + (0.0551x^2 + 0.5896x - 3.5793) \quad [2]$$

Equation [2] produced close agreement to the measured static pressure waves at 10 and 70 LPM NHF, and reasonable agreement at the intermittent NHF flow rates. The largest relative differences between estimated and actual transient pressures occur for 20 LPM NHF. Figure 35 shows the comparison plots of the estimated and actual transient pressures for 70 LPM and 20 LPM illustrating the predictive ability of the approximation formula. It must be noted that this formula is only applicable to this particular airway model and breathing pattern for the specific range of NHF flow rates from 0 to 70 LPM. Similarly, it is only valid for approximating the static pressures at the superior trachea position from the static pressures measured at the same position during natural

breathing as other regions show different losses and would require different expiration and inspiration specific values for the constant *A*.

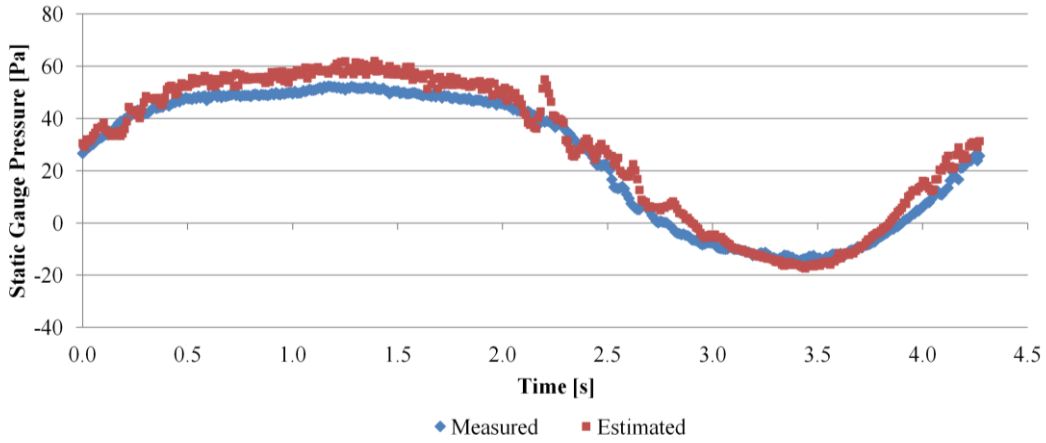

(a)

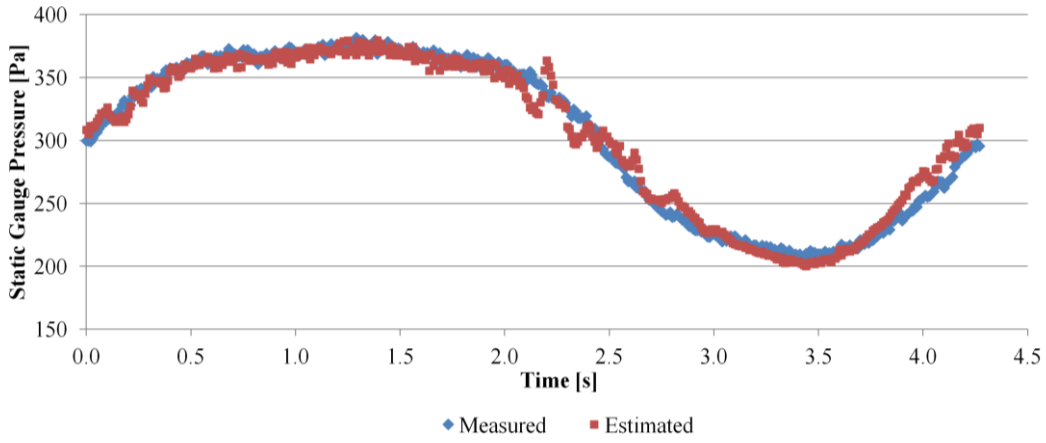

(b)

Figure 35: Plots of actual measured transient static pressures and the transient static pressures estimated using natural breathing data and Equation [2] for (a) 20 LPM showing the major differences and (b) 70 LPM showing close agreement.

With the introduction of increasing levels of Optiflow™ NHF therapy there is an increase in the pressure drop across the upper airway for both inspiration and expiration phases as previously shown in Figure 34. Relative to the flow rates of breathing achieved during each phase, expiration pressures losses surpass those of inspiration, in contrast to the greater relative pressure losses seen during inspiration for natural breathing. With the increase in flow resistance during expiration due to the inward flow of the NHF this is an expected outcome. Figure 36 illustrates this in a plot of the flow rate alongside the static pressures at the superior trachea measurement positions for 70 LPM Optiflow™ NHF therapy. The flow rate curve has been shifted up the y-axis to match the x-axis to the mean pressure and normalised by the peak inspiratory pressure allowing for the flow and pressure

profiles to be easily compared. Unlike the equivalent natural breathing plot in Figure 29 where the flow curve was greater than the static pressure curves during expiration, here the static pressure curves exceed the flow implying greater resistance to expiration flow.

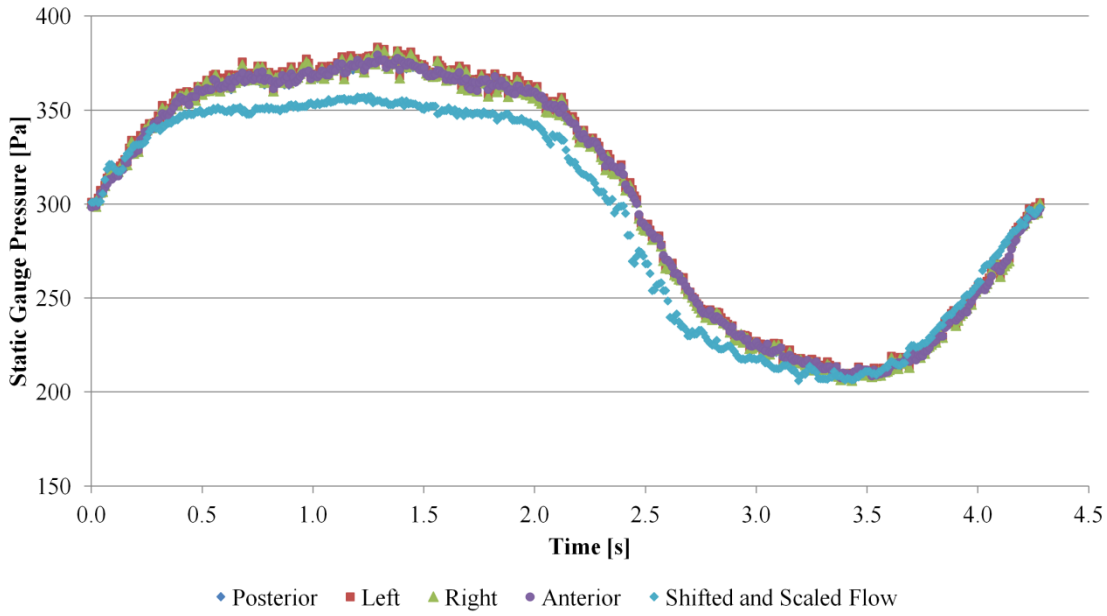

Figure 36: Transient static pressures at the perimeter of the superior trachea during breathing with 70 LPM Optiflow™ NHF therapy in comparison to the flow rate illustrating increased expiratory pressure loss. Flow rate scaled by a factor of 4.212 Pa/LPM and shifted up by constant 299.93 Pa.

7.4 Conclusions

Measurements of the static pressures at numerous positions within the upper airway 06B model were performed for natural breathing and breathing during Optiflow™ NHF therapy. During natural breathing the peak static pressures within the upper airway were seen to increase in magnitude in the direction of the trachea with local fluctuations. The form of each static pressure wave observed was overall in phase with and similar to the flow wave produced by the pump. Peak expiratory and inspiratory pressures at the superior nasopharynx, just posterior to the nasal septum, were related to the flow by a very similar factor implying that resistance across the nasal passage was the same in both flow directions. This agreed with the in vitro findings of Croce et al. (2006) but is contrary to in vivo measurements which have found that patency of the compliant nasal vestibule is decreased during inspiration leading to a slightly greater resistance than expiration (Shepard and Burger, 1990). Peak static pressures at the superior trachea during natural breathing inferred that the entire upper airway exhibited a higher resistance to inspiration than expiration. Analysis of the airway geometry concluded that this was due to the expiratory flow experiencing more recoverable pressure losses, most notably at the expansion into the nasopharynx.

Implementation of Optiflow™ NHF therapy during natural breathing flows generated an increase in the mean and peak static pressures and a deepening of the pressure amplitude at all pressure taps. Peak inspiratory static pressure at the superior trachea became less negative with increasing NHF flow rate, first crossing the horizontal axis and taking on a positive value for a therapy flow rate of 30 LPM. Thus at a flow rate of 30 LPM Optiflow™ NHF therapy fulfilled the inspiratory resistive work requirements of the upper airway. At the maximum tested NHF flow rate of 70 LPM the mean static gauge pressure at the trachea measurement positions had risen from 0 Pa during natural breathing to 300 Pa. For the NHF therapy flow rates tested from 10 to 70 LPM the general form of the transient static pressure curve remained similar to that for natural breathing and could be reasonably well approximated by scaling and translating the natural breathing curve. This was exemplified by determination and application of Equation [2] for the approximation of static pressures at the superior trachea as a function of NHF flow rate. Though the implementation of NHF therapy was found to decrease inspiratory work with increasing flow rate it also caused increasing resistance to expiration which at some level of therapy may be more detrimental than beneficial to the user.

8 Turbulence Intensity in the Upper Airway

It is hypothesised that the level of CO_2 wash out achieved by Optiflow™ NHF therapy has a relation to the air velocity within the airway and the turbulence of the flow through the pharynx. Turbulence in a flow improves the level of mixing and in the case of NHF it was postulated that turbulence within the airway would help to disturb pockets of trapped exhaled gases, flushing them out and preventing them from being re-inhaled. It was also thought that the flow velocity exiting the cannula could be related to the level of flushing achieved, as with higher jet velocities from the cannula it is possible that the flow stream would penetrate the airway to a greater depth. The greater the depth of jet penetration, the greater the volume of the airway that is flushed of CO_2 rich exhaled gases.

It is thought that in the pharynx the flow regime may be transitional due to the presence of vortices induced by the protrusion of the epiglottis into the flow path and a turbulent jet through the pharynx on expiration (Jeong et al., 2007, Shinneeb and Pollard, 2012). There has been some support for this notion from previous measurements of static pressure within the same airway models employed within this research (Cressy et al., 2011). These measurements showed a large pressure drop occurring in the pharynx when steady, constant expiratory flows were passed through the five airway models. Hot wire anemometry was employed to further examine the velocities within the airway models and investigate the presence of turbulence during both natural breathing and breathing with Optiflow™ NHF therapy.

8.1 Turbulence and Turbulence Intensity

A turbulent flow regime is characterised by chaotic instabilities in flow velocity with both time and space, often seen as vortices and eddies within the flow stream. When a flow encounters a sudden change in geometry, such as the protrusion of the epiglottis into the pharynx, turbulence may be induced in the downstream flow. A flow's regime is often described by its Reynold's number, the ratio of the inertial forces to the viscous forces, defined by the following Equation [3]. A low number indicates the predominance of viscous forces and subsequently a laminar flow. Conversely, a high number suggests inertial forces are dominant and thus the flow is turbulent.

$$\mathrm{Re} = \frac{\rho u L}{\mu} \qquad \textbf{[3]}$$

However, for a complex flow domain such as an upper airway, the occurrence of turbulence cannot be predicted confidently by the Reynold's number, nor can the Reynold's number describe the magnitude of the turbulence. Turbulence intensity, which can be experimentally determined, is a relative measure

of the level of turbulence in a flow. It is defined as the ratio of the root mean square (rms) velocity, U_{rms}, to the mean velocity of the flow, U_{mean}. This is illustrated in Figure 37 below and is defined by Equation [4].

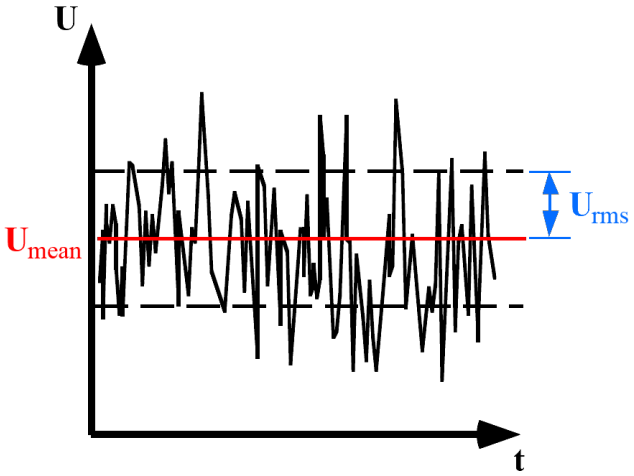

Figure 37: Illustration of a turbulent velocity profile showing mean and rms velocities (adapted from www.mit.edu).

$$TI = \frac{U_{rms}}{U_{mean}} \times 100\% \qquad [4]$$

Turbulence intensity was chosen as the measure for evaluating the turbulence within the airway as it was possible to measure both the mean and rms velocities at locations within the airway by the use of hot wire anemometry. As the determination of turbulence intensity requires a mean flow velocity and the flows examined were to be transient, only the small regions of peak inspiration and peak expiration were examined where the flow acceleration could be said to be momentarily zero. As measurement of the mean velocity was a necessary component of turbulence intensity determination, the peak inspiration and expiration mean velocities observed during all measurements are also examined and discussed within this chapter.

Hot Wire Anemometry

Hot wire anemometry is a commonly used technology for measuring turbulent flows as the method of sensing is highly responsive to velocity fluctuations. The sensing element, in the form of a probe, is also very small with a shaft diameter of only 1.9 mm. Both of these attributes make hot wire anemometry ideal for measuring turbulence intensity within the small volumes of the pharynx.

Hot wire anemometers measure velocity by employing the principles of heat convection and Ohm's law. The probe consists of a fine platinum-plated tungsten wire filament, 5 μm in diameter, suspended between two thin metal posts 1.25 mm apart forming an electrical pathway between them. The probe is connected to a control box where it forms part of one arm of a Wheatstone bridge. The control box electrifies and regulates the current supplied to the probe maintaining the filament at a constant resistance and subsequently a constant temperature. By measuring the bridge voltage, which constitutes the heat transfer, the air velocity can be determined using the known heat transfer properties of the filament and the air.

Each probe is known to have a particular voltage to velocity curve. Due to the delicate nature of the probe filament it is susceptible to small changes in its heat transfer properties with exposure to airborne debris during testing. A simple two-point probe calibration can be carried out prior to testing to account for this and bring the curve into alignment. To do this two flows of known constant velocities, one at the upper and the other at the lower end of the probes measuring range, are passed over the probe and their respective voltages are captured. The voltage-velocity curve is then fitted to these two calibration points.

8.2 Experimental Procedure

Two different sets of velocity and turbulence intensity measurements were carried out focusing on two anatomic regions. The first set concentrated on the velocities and turbulence intensities of flows passing through the nares and how these differed between each naris of the same airway and further how they were affected by changes to the upper airway geometry. These experiments required the use of the five different upper airway models but excluded use of Optiflow™ NHF therapy. Measurements were also made on two live adult subjects as a comparison to the controlled in vitro environment. Optiflow™ NHF therapy could not be employed for these experiments as the cannula prongs occlude much of the central area of each naris thus preventing placement of the hot wire probe. The second set of measurements looked more closely at the turbulence intensity within a single airway, mapping the variation along an anterior to posterior traverse of the velopharynx. Optiflow™ NHF therapy was introduced to these experiments to investigate how this turbulence intensity profile along the traverse differed when increasing levels of NHF therapy were applied to the model. This experiment utilised only one of the upper airway models, the standard airway 06B model, and various levels of Optiflow™ NHF therapy. Both experiment sets required slightly different procedures as defined in the following sections; however, the hot wire probe calibration and data acquisition methods were the same for both.

8.2.1 Probe Calibration

As described above there is a known relationship between the velocity of the air flow past the probe and the measured bridge voltage, which depends on physical properties of the system. As a result of using the probe in an open air environment its resistive properties can differ from use to use. Subsequently it was necessary to calibrate the probe regularly to ensure that measurements recorded were accurate, in this case on a daily basis before each use.

The Dantec Dynamics hot wire calibrator was used to calibrate the probe with the two-point calibration described above. Compressed air was supplied to the calibrator and metered to one of two constant, factory-set velocities, denoted as low and high and selected with a lever handle on the calibrator. A needle valve could also be adjusted to provide additional flow velocities which could be determined using a pitot tube at the flow outlet. The hot wire probe was mounted above the flow outlet in a cradle and adjusted so that it was situated central to the orifice with the filament in line with the outlets upper surface. Once in place the probe was connected to the CTA control box and the current turned on. The system variables were input into the Dantec Dynamics software and the two-point calibration program was run, where the bridge voltages were recorded for the low and high calibrator settings. The software then fit the curve to the calibration points and saved the calibration for subsequent measurements, thus completing calibration.

8.2.2 Data Acquisition Setup

As the turbulence intensity is defined as the ratio of the rms velocity to the mean velocity of the flow, the turbulence intensity of the oscillatory flow as a whole cannot be simply defined. Instead the turbulence intensity at characteristic regions of the flow, namely the peaks of inspiration and expiration, were investigated. At these peaks, where the flow acceleration drops to zero, there are short intervals of time where the mean velocity of the flow can be considered to be momentarily constant. It is for these short intervals of approximately constant velocity that hot wire data was desired. To capture the velocity fluctuations in the flow the data acquisition system of the Dantec software was set up to record a minute of data for each in vitro experiment at a sampling frequency of 1 kHz. This set up allowed for the capture of multiple consecutive breath waves so that during data analysis the turbulence intensities calculated at peak inspiration and expiration could be averaged over a minimum of ten breath cycles. Data was captured for a shorter period of 20 seconds during in vivo experiments at the same 1 kHz frequency.

8.2.3 External Nares Measurements

To examine the levels of velocity and turbulence intensity which occur at the centre of the naris during natural breathing, both in vitro and in vivo experiments were performed. During in vitro experiments five unique airway models were employed, whilst two live subjects volunteered for the in vivo investigations. Individual measurements were performed at each naris, left and right, for all five airway models and the two live subjects. The procedures employed in vitro and in vivo are described separately below.

In Vitro

The five different upper airway models to be used for this first set of turbulence intensity experiments showed a wide variation in the size and geometry of the nares. Table 4 provides the average length of the major diagonal of the nares for each airway model as well as the major width of the base of the nose. All dimensions were measured from the physical models as illustrated by Figure 38.

Table 4: Major measurements of the nares and nose of each airway model showing large variation in physical characteristics.

	Average Major Naris Diagonal Length [mm]	Major Width of the Base of the Nose [mm]
Airway 06B[2]	20.09	33.80
Airway 07B	14.97	39.45
Airway 09	13.23	30.86
Airway 10	19.47	33.60
Airway 16a	13.94	41.48

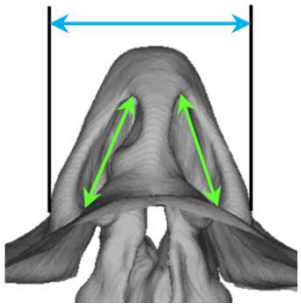

Figure 38: Illustration of nose and naris measurement positions with naris major diagonal length shown by green arrows and major width of nose base shown by blue arrow.

Additionally each model had visible asymmetry between the left and right nares. As a consequence of this it was considered too complex to define a universal datum on the models' surfaces from which measurement positions could be specified. Similarly, it was decided that a single point measurement would suffice for each naris as defining a series of equivalent measurement positions across all models would be just as complex. Subsequently the positioning of the probe for each naris turbulence intensity measurement was set by eye. The probe filament was aligned with the centre of the naris and in line with the plane of the naris cross-section. This is illustrated in Figure 39 where the probe is positioned central to the left naris of Airway $06B^2$.

Figure 39: Two views of the probe positioning central to the external naris opening of Airway $06B^2$

Once the probe had been positioned the experiment was commenced by starting of the piston pump. During these tests the first generation of the breath flow waves, with the high tidal volume of 799 ml and breath period of 5.08 seconds as described in Chapter 6, was employed as it was the standard breath wave at the time. After a minute had passed to allow the system to settle into a consistent rhythm, data acquisition of the flow rate from the TSI flowmeter was initiated at the onset of an expiration, followed by hot wire data acquisition initiation at the onset of the next expiration. After completion of a minute of hot wire data acquisition flow rate logging was also terminated.

In Vivo

The turbulence intensity at the external nares of two adult subjects, one male (41 years, BMI of 21.5 kg/m^2) and one female (24 years, BMI of 18.8 kg/m^2), were also measured for comparison to the in vitro experiments. Subjects were seated in an upright position with the head stabilised by an ophthalmology chin rest. Hot wire probes were positioned central to the outlet of each naris in the same manner as in vivo testing; however, due to the inability to completely fix the subjects' heads, the probes were positioned slightly farther from the nares to prevent probe damage. Due to the uncomfortable nature of the experiment and the possible adverse affects on the breathing pattern, data

was acquired for a minimum period of 20 seconds. Data acquisition was commenced at the onset of expiration as was the case for in vitro experiments. For all experiments subjects were encouraged to be relaxed and breathe naturally.

8.2.4 Velopharynx Traverse Measurements

Experiments to determine the turbulence intensity profile across an anterior to posterior traverse of the velopharynx in an airway model were performed for both the case of natural breathing and breathing with various flow rates of Optiflow™ NHF therapy. The purposed of these experiments was to determine whether the introduction of Optiflow™ NHF therapy increased the level of turbulence within the airway, specifically at the velopharynx, and how this possible increase may in turn be affected by the NHF flow rate. As it was the effects of the Optiflow™ NHF therapy on the turbulence which were under investigation, these experiments were performed using only the standard upper airway geometry, airway 06B.

To allow for measurements to be made within the airway the original airway model, airway 06B[1], was prepared with a small, 3.5 mm diameter hole entering into the posterior velopharynx central a transverse cross section. The length of this hole, from the entry point on the exterior model surface to its exit on the posterior velopharynx wall, was measured to be 11.40 mm for reference during traverse movements. Through this hole a hot wire probe was able to gain access to the full anterior to posterior diameter of the velopharynx.

The model was set up in the experimental system for the turbulence intensity measurements as described in the Chapter 5. The probe support was mounted into the traverse mechanism clamp, as illustrated in Figure 40, and a shorting probe was installed into it. As can be seen in Figure 41, the shorting probe is a solid single prong, unlike the delicate hot wire probe, and as such could be used to accurately measure the depth to which the velopharynx could be accessed with the traverse. First, the probe was advanced until its end was flush with the exterior surface of the airway model and the traverse scale reading was recorded. The probe was then advanced through the hole until it met with the anterior surface of the velopharynx, once again recording the reading on the traverse scale. The difference between the two readings was then calculated as 21.40 mm, the maximum depth of the velopharynx. The difference between this depth and the depth of the hole, which equated to the straight line length between the anterior and posterior surfaces of the velopharynx, was also calculated at 10.00 mm. This length was divided into nineteen equally spaced measurement points, 0.05 mm apart, which began and ended 0.05 mm from the anterior and posterior velopharynx walls.

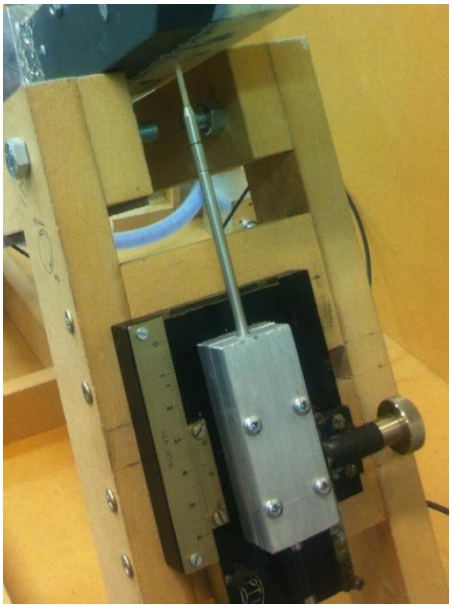

Figure 40: Probe support mounted into traverse mechanism positioned perpendicular to entry hole in posterior wall of the Airway 06B[1] model.

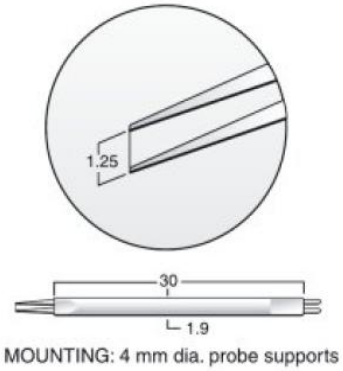

(a) **(b)**

Figure 41: Comparison of Dantec Dynamics (a) 55P11 probe used for measurements; and (b) shorting probe used to find position of anterior velopharynx wall (adapted from dantecdynamics.com).

Once these critical dimensions had been found, the shorting probe was replaced with the calibrated hot wire probe. As with the shorting probe, this was advanced until it was flush with the exterior surface of the model and the traverse reading recorded. From this measurement, the traverse positions for each of the nineteen measurement points were calculated and the probe was advanced to the first and most anterior position. The clearance gap between the hot wire probe and the hole perimeter was sealed with Blu Tack at the exterior surface to prevent any flow from short-circuiting the airway path.

These more comprehensive measurements of turbulence intensity within the airway were performed during a later stage of the research than the external nares experiments and during the interval the breath flow wave had evolved to represent that of a more average human adult. Subsequently these experiments were conducted using the average breath flow wave with a 450 ml tidal volume and a breath frequency of 14 breaths per minute. Prior to beginning measurements the pump was allowed a minute of operation for the flow to settle into a consistent pattern. Data acquisition followed the same protocol described for the external nares measurements where TSI flow meter data logging was begun at the onset of an expiration cycle followed by the initiation of hot wire data acquisition at the onset of the next expiration cycle. At the conclusion of hot wire data acquisition, the flow meter data logging was stopped and the probe was moved to its next measurement position. The seal around the probe was assessed and adjusted as necessary before the data acquisition process was repeated. This was carried out until data for all 19 measurement points was attained.

The first set of measurements did not employ Optiflow™ NHF therapy thus replicated a naturally breathing adult. For subsequent experiments the Optiflow™ nasal cannula was placed on the airway model and supplied with air flows as described in the Chapter 5. The turbulence intensities at the nineteen traverse positions were then re-measured following the same protocol above for all Optiflow™ NHF therapy flow rates assessed from 10 to 70 LPM at 10 LPM intervals. The use of NHF therapy is expected to alter the breathing patterns of the user when administered to live subjects; however this affect was not investigated as the breathing pattern employed remained constant throughout all experiments so that the influence of the NHF therapy on the velocities and turbulence could be observed.

8.3 Data Processing

To extract the mean and rms velocities from the peak inspiration and expiration hot wire data a few steps were necessary. First, the regions of interest over which the flow velocity could be considered to be constant had to be defined. Analysis of the breath flow waves used to drive the pump allowed for identification of regions of approximately constant flow rate and therefore flow velocity. These brief windows, defined in terms of milliseconds, were referenced from the instantaneous point of zero velocity at the beginning of the expiration portion of the curve. As two different forms of the breath flow wave were used, an older version for the in vitro nares experiments and the newest version for the in vitro velopharynx measurements, these regions were different in length but occurred at the same position relative to the period of the breath. The peak velocity regions evaluated for expiration and inspiration are highlighted on a plot of a natural breathing flow wave measured during an in vitro velopharynx experiment in Figure 42.

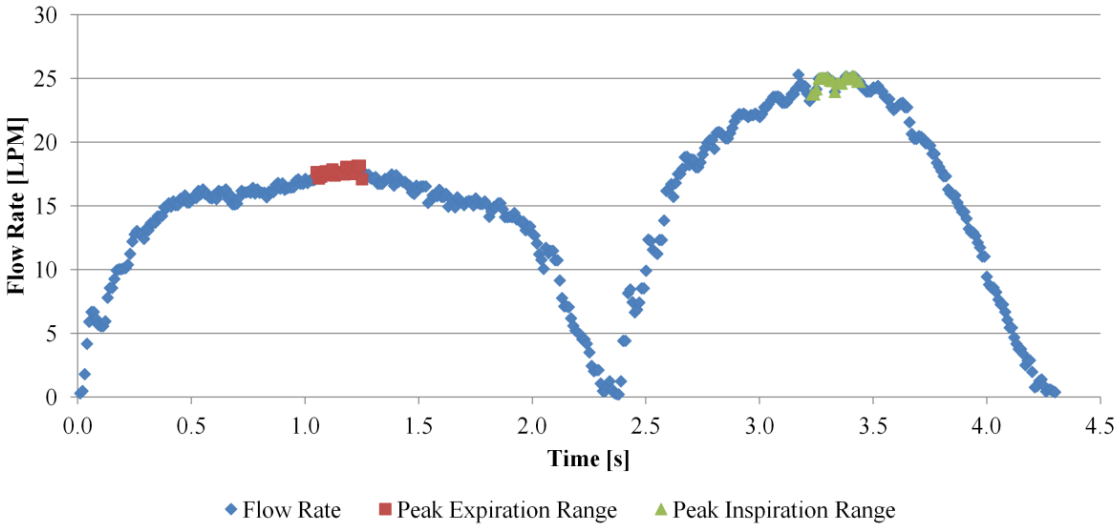

Figure 42: Flow rate profile of natural breathing flow wave illustrating regions used to determine turbulence intensity at peak expiration and inspiration.

Manual triggering of the hot wire data acquisition meant that the raw data sets did not all start exactly at the beginning of expiration, the reference for the data analysis. Consequently, it was necessary to manually adjust some of the raw data sets accordingly before the peak inspiration and expiration regions could be extracted.

Matlab was used to extract and analyse the peak inspiration and expiration regions from the data sets. For the in vitro experiments ten inspiration and ten expiration peak regions from every data set were reduced to mean and rms velocities. From these ten, an average mean and rms velocity and hence turbulence intensity were able to be calculated for each set of data. For the in vivo results only one inspiration and one expiration peak from each data set were analysed as fewer and less uniform breath cycles were captured due to the less controlled nature of the experiments. The formulae used to calculate the mean velocities, U_{mean}, and rms velocities, U_{rms}, are given as Equations [5] and [6] below, and from these values turbulence intensities were determined using the previously stated Equation [4].

$$U_{mean} = \frac{1}{N}\sum_{i=1}^{i=N} U_i \qquad [\,5\,]$$

$$U_{rms} = \sqrt{\frac{1}{N-1}\sum_{i=1}^{i=N}\left(U_i - U_{mean}\right)^2} \qquad [\,6\,]$$

8.4 Results and Discussions

The experimental results described following are separated into two sections, the external nares measurements followed by the velopharynx traverse experiments. The external nares measurements are further divided into the in vitro and in vivo results, though comparisons are made between the two within the in vivo results subsection.

8.4.1 External Nares

In Vitro

Figure 43 shows a plot of the first 25 seconds of raw hot wire anemometry data obtained from the right naris of airway 06B[2] during natural breathing. This shows the raw velocities captured, beginning at the onset of expiration. Both expiration and inspiration are given as positive values due to the nature of measurement by hot wire anemometry which cannot determine flow direction, only magnitude. From just this raw data it can be seen that the velocity during peak expiration reaches a higher mean value than peak inspiration. Peak expiration also shows a much higher level of turbulence than peak inspiration as seen by the noise at the peak of the plot curves.

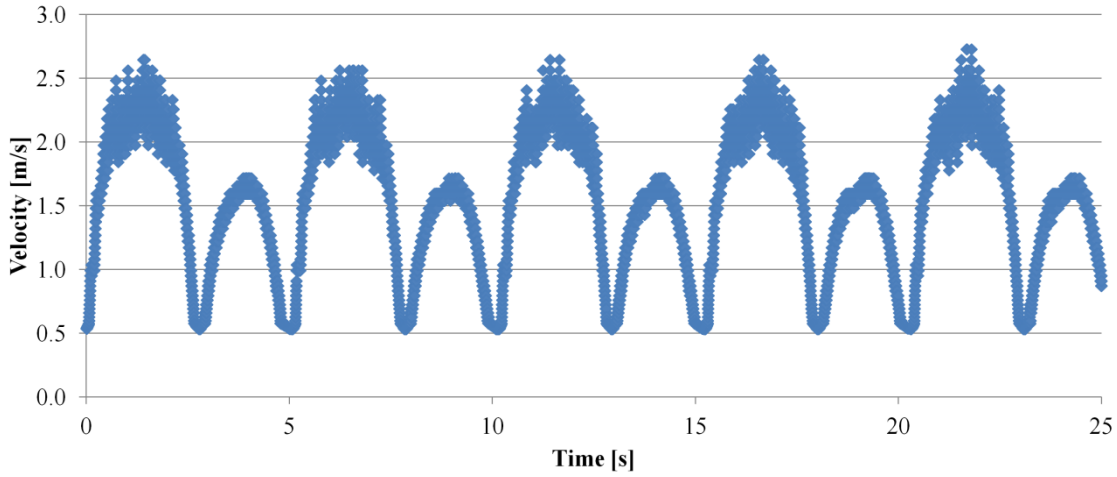

Figure 43: The first 25 seconds of raw hot wire data acquired at the right naris of airway 06B2 during natural breathing.

The mean velocities at each naris during the peak of expiration and inspiration were extracted from the five airway models hot wire anemometry data. These velocities have been plotted together identified by naris (left or right) and cycle peak (expiration or inspiration) in Figure 44.

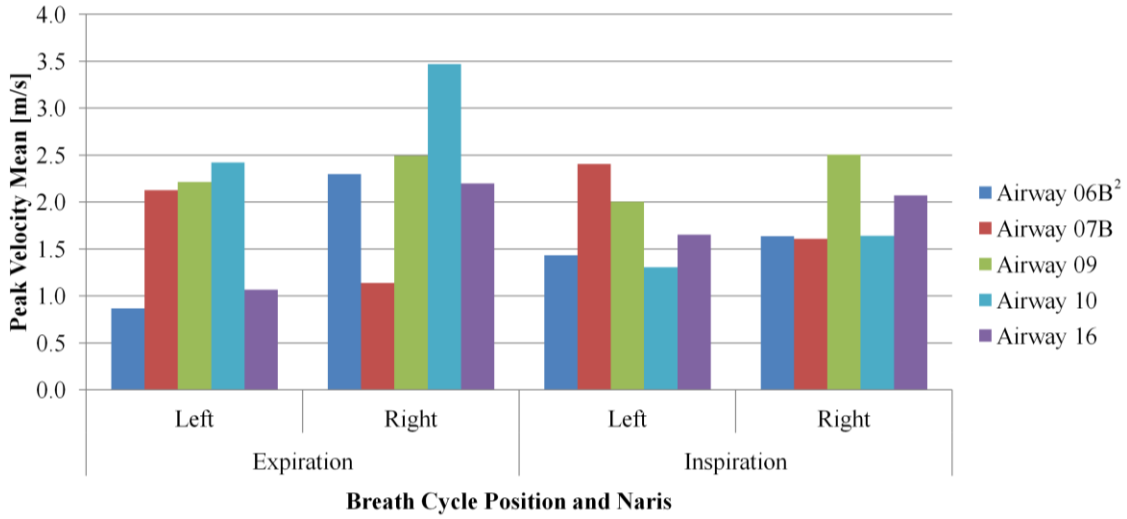

Figure 44: Peak expiration and inspiration mean velocities at each naris averaged over ten breath cycles for each of the five airway models.

Differences in mean peak velocity can be seen between both nares of each airway and also between expiration and inspiration peaks at the same naris. The mean velocity during peak expiration at each of the ten nares is greater than the mean velocity at peak inspiration for exactly half of the cases. Although there is an even split between which flow direction produced the greatest velocity magnitude, the velocity magnitudes found during peak expiration show a much greater spread than peak inspiration. Mean peak velocities of 0.87 to 3.47 m/s were seen across the airway models for expiration while inspiration mean peak velocities ranged from 1.31 to 2.50 m/s. It is known from other research that air is drawn into the nares from a hemispherical region surrounding the nose (Doorly et al., 2008b, Taylor et al., 2010) during inspiration. This provides a more even profile across the cross sections of the naris than expiration which produces a jet like profile on exit (Stringer et al., 2010). Because the probe was positioned central to each naris by eye, it is likely that this position did not coincide with the centre of the expiration jet in all cases. This would explain the large variation seen in the expiration peak magnitudes.

For each of the five different airways tested, the naris which exhibited the greatest mean peak velocity during expiration also had the greatest mean peak velocity during inspiration. Static pressure measurements in the airway $06B^2$ model indicated that the airway resistance through the solid model nasal cavity was equal for both inspiratory and expiratory flow directions. From these velocity results it is further implied this is true not only for the nasal cavity as a whole but for each side of the nasal cavity individually. The differences in the velocities seen at the two nares of each airway show a difference in the resistance in each nasal cavity with the flow favouring the path of least resistance. It is well known that for most adults the mucosal lining of the two sides of the nasal cavity swell and contract oppositely in a cyclic manner known as the nasal cycle. This process has a period of approximately three to seven hours and occurs such that the total resistance across the nasal cavity

remains almost constant (Baraniuk and Kim, 2007, Jones, 2001, Moinuddin et al., 2001). Four of the five airway cases showed the highest mean peak velocities at the right naris indicating that at the time they were subjected to the CT scanning process they had a higher resistance through the left side of their nasal cavity.

A high level of difference is seen between the turbulence intensities of peak expiration and peak inspiration observed at the nares as illustrated in Figure 45. For all airway models turbulence intensities during peak expiration of at least 30% were seen at one naris, both nares in the case of airway 16, whilst no airway had a turbulence intensity exceeding 4% at either naris during peak inspiration. Overall very high levels of turbulence intensity were measured during peak expiration with a maximum of 46% observed at the left naris of airway 09. Conversely, peak inspiration presented low turbulence intensities for all airways with a maximum of 4% seen at left naris of airway 16. These low levels of turbulence during peak inspiration agree well with the 2.5 % turbulence intensity found at the naris cross section of a 20 times scale nasal cavity by Hahn et al. (1993) during an average steady inspiratory flow rate. The presence of high turbulence in the case of peak expiration is an expected result due to the flow of expiration having the form of a jet created by the contraction at the nasal valve. As this jet passes through the nasal vestibule and exits the naris it exerts a shear force upon the relatively stationary mass of surrounding ambient air, causing a transfer of momentum and inducing turbulence. During inspiration however, air is drawn into the nares from the surrounding hemisphere with little disruption from the smooth profiles of the surrounding face.

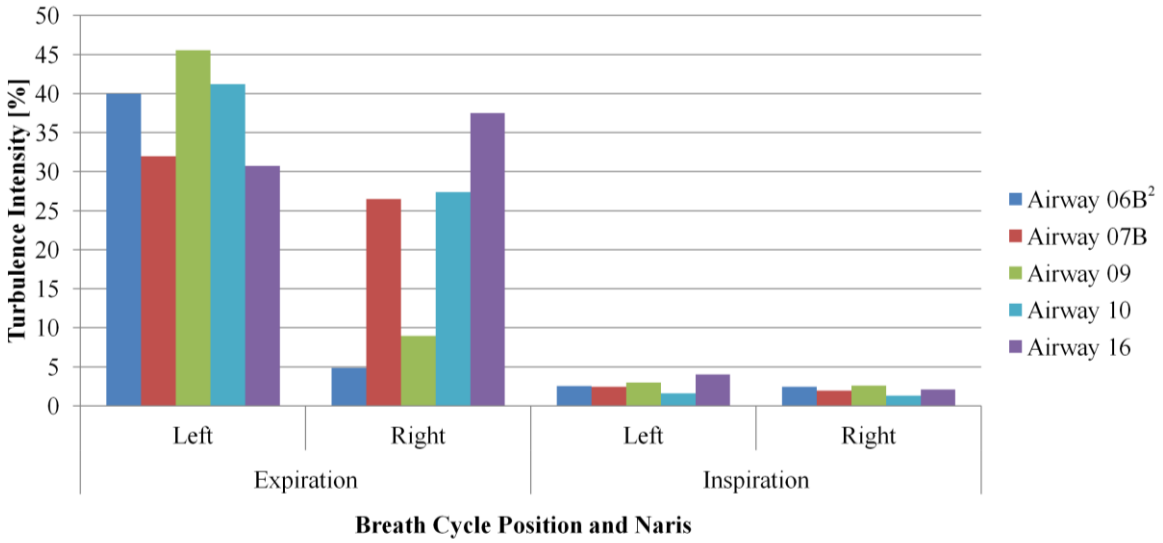

Figure 45: Peak expiration and inspiration turbulence intensities at each naris averaged over ten breath cycles for each of the five airway models.

As with the mean velocities there is a large spread in the turbulence intensities observed at peak expiration. The breathing pattern used for this experiment was the same for all airways therefore any variation in the turbulence intensity is due to the geometrical differences in the airway models and

differences in the positioning of the probe. The geometry of the nasal valve and nasal vestibule would affect the velocity and profile of the expiratory jet and subsequently the turbulence intensity at the naris. Unfortunately another effect of the geometrical differences is the difficulty it causes in determining analogous measurement positions between the five models. It is possible that the differences seen are predominantly caused by the geometrical variation in the airway models, but it is also likely that they result from measurements being taken at only a single point with the probe positioned by eye. With such high levels seen at some airway nares it is highly likely that the turbulence intensity varies greatly across each naris cross section and the points of greatest turbulence intensity may not have been captured at each naris. Despite this some interesting points can still be drawn.

Similar to the peak mean velocity results which showed a bias towards a single naris in both directions, the naris showing the highest turbulence intensity during peak expiration also showed the highest turbulence intensity during peak inspiration for four of the five airways. The exception to this was airway 16 which had the greatest turbulence intensity of 37% at the right naris during peak expiration, compared to 31% at the left, while during peak inspiration the left naris displayed the higher turbulence intensity of 4% in contrast to 2% at the right. Airway 16 is a unique geometry as it appears to be from a person of Polynesian or Micronesian descent based on facial features, unlike the other four airways which appear to be of European descent. Most importantly the profiles of the nares are significantly different as shown in Figure 46. This could be the source of the difference seen in turbulence intensity peaks between airway 16 and the four other airway models.

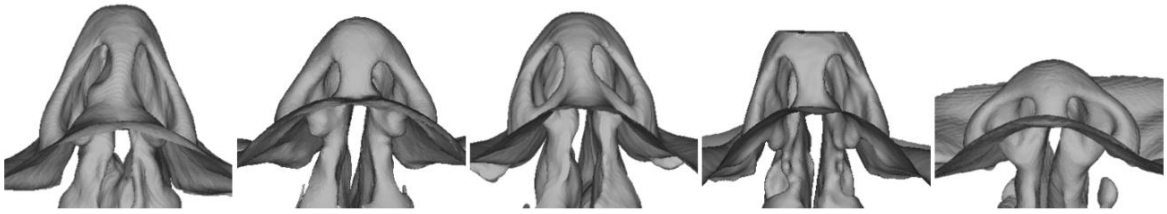

Figure 46: View of the nares of each the five airways from left to right 06B, 07B, 09, 10 and 16 showing the significant difference in the form of the nares of Airway 16.

Figure 47 shows the turbulence intensity and mean velocity observed at each naris of the five airways during (a) peak expiration and (b) peak inspiration. From plot (a) it can be seen that in three of the five airway cases the naris which produced the higher mean velocity showed the lower turbulence intensity during peak expiration. Similarly, plot (b) shows that the naris with the higher mean velocity during peak inspiration produced the lower turbulence intensity in four of the five airways. The mean velocity at the naris during both peak expiration and inspiration is therefore not an indicator of the magnitude of the turbulence. This is further confirmed by a plot of the turbulence intensity at each naris as a function of the mean velocity given in Figure 48.

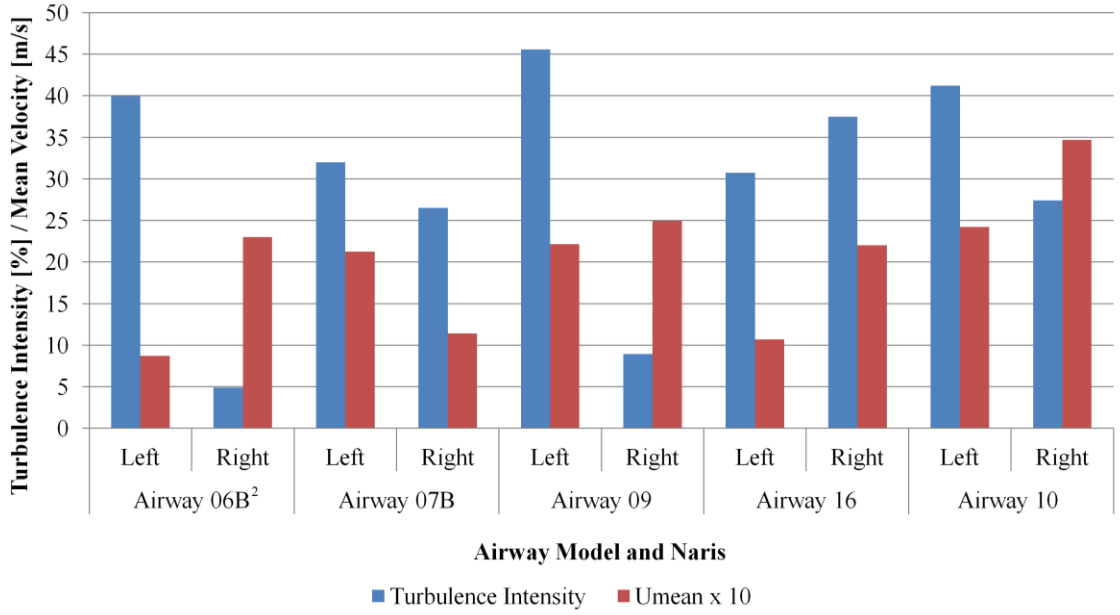

(a)

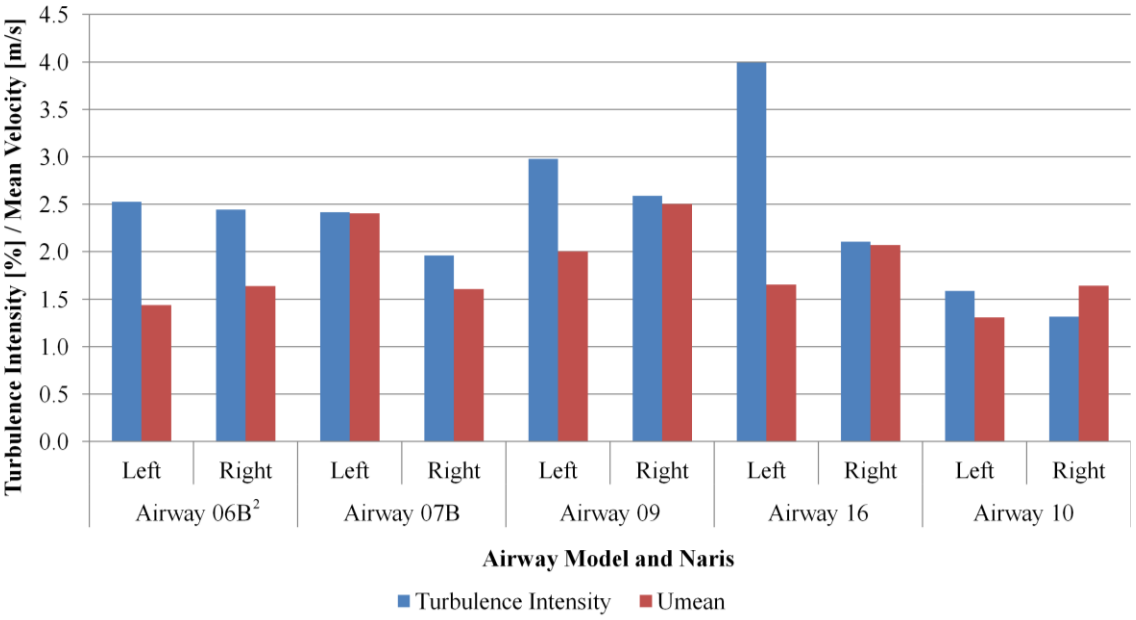

(b)

Figure 47: Comparison of turbulence intensity and mean velocity found at each airway naris during (a) peak expiration where mean velocity has been scaled up by a factor of 10; and (b) peak inspiration.

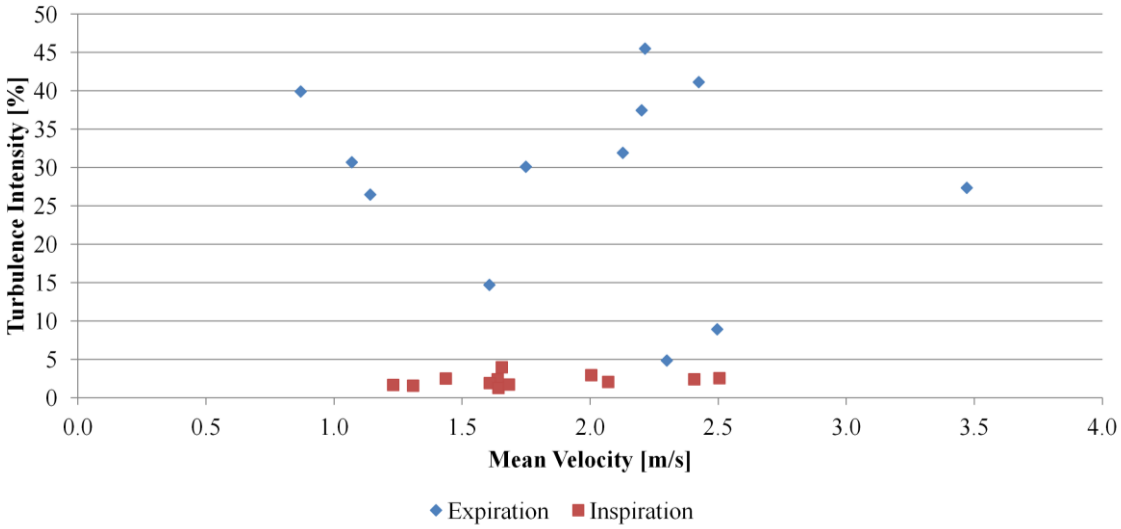

Figure 48: The turbulence intensity measured at each airway naris as a function of the mean velocity measured at the same naris for both peak expiration and peak inspiration illustrating the absence of a relationship for either.

These two figures show that a high mean velocity at the measurement position is not indicative of high or low turbulence intensity at the same position for either peak expiration or inspiration. There is no discernible relationship between the mean velocity and the turbulence intensity.

In Vivo

The raw velocity data obtained outside the central nares of the two live subjects is plotted in the following Figure 49 with each series beginning at the onset of inspiration. It is immediately apparent that the velocity pattern at each measurement position has much greater variation from cycle to cycle than was seen in the controlled in vitro experiments. Results from the female subject also show a change in the period of the breath cycle between the measurements at the two different nares, whilst the breathing frequency of the male subject had close agreement of between the two. This discrepancy in the breathing frequency of the female subject indicates the effect of being conscious of observation on the breathing pattern. Despite the subject understanding the necessity to breathe as naturally as possible their breathing pattern was still affected.

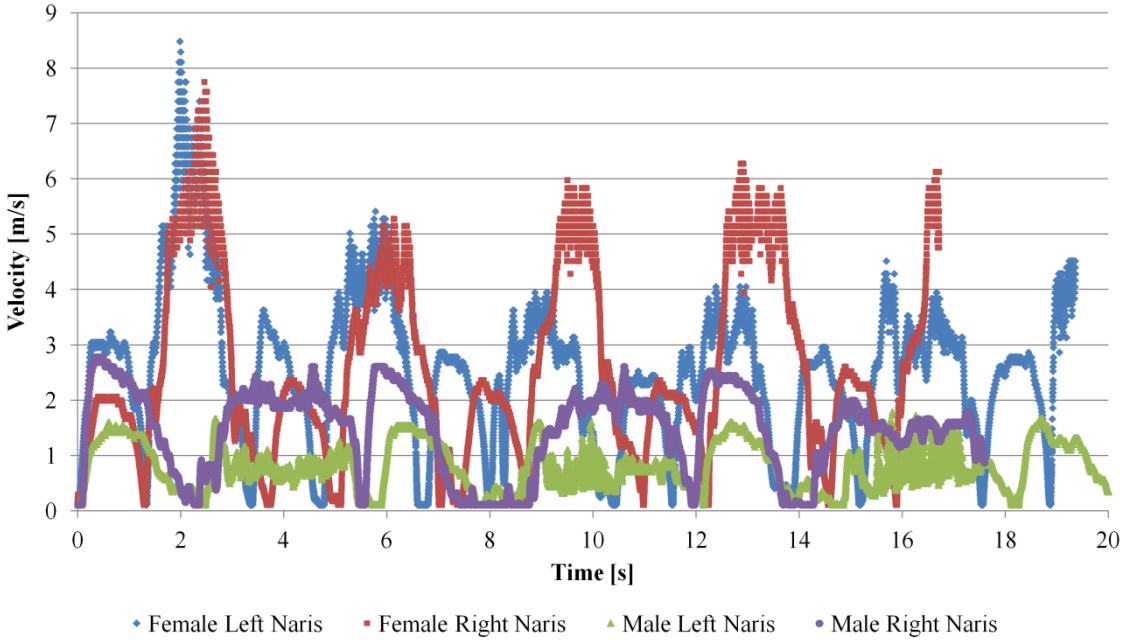

Figure 49: Raw hot wire data from in vivo naris experiments showing wide variation in breathing patterns between male and female subjects.

The magnitudes of the peak velocities at the nares also differ greatly between the two subjects with the male showing velocities no greater than 3 m/s while the female subject produced peak velocities exceeding 8 m/s during one expiration cycle. These very high peaks occur at both nares for only the first expiration of captured data and are not the mean peak velocities but the maximum velocities measured. Although the later expiration peaks measured on the female subject show lower and more regular velocities they are still in excess of those measured on the male subject. The differences in velocities between the two subjects are an indication in the wide variation in breathing patterns, tidal volumes and nasal geometries between the two. This validates the benefits of performing in vitro measurements with controlled breathing conditions as a means of observing the influence of airway geometry alone.

As with the in vitro data, mean velocities at the peak of expiration and inspiration were extracted from the hot wire anemometry data; however, due to the more erratic nature of the breathing patterns only a single expiration and a single inspiration peak were evaluated from each twenty second dataset. The peak expiration and inspiration mean velocities for both subjects are plotted in Figure 50.

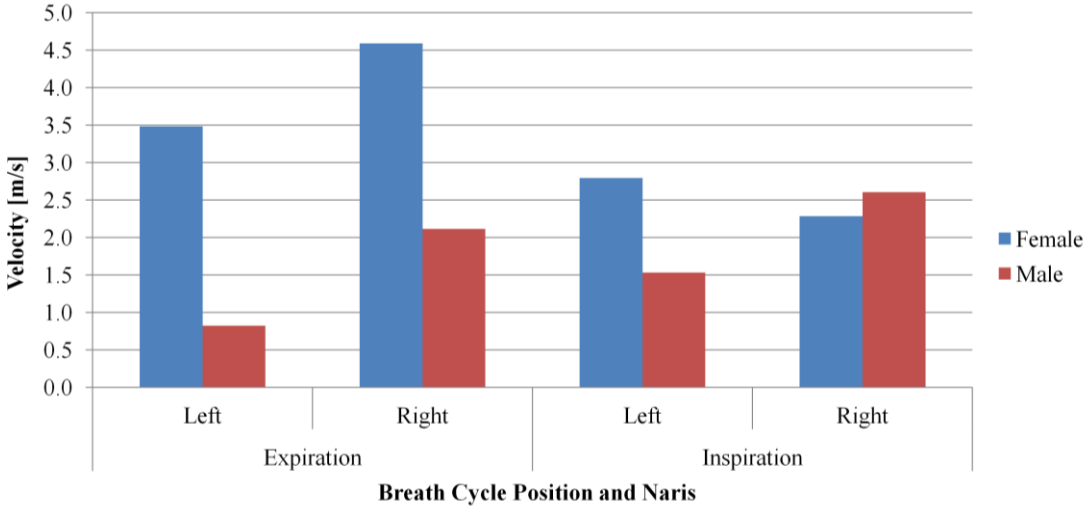

Figure 50: Comparison of the mean peak velocities seen at the nares of each in vivo subject for both peak expiration and inspiration.

Comparison to the in vitro results shows that, like the airway models, the male subject shows the same velocity bias through one naris for both expiration and inspiration. The female subject however has a higher mean peak velocity of 4.59 m/s through the right naris during expiration but a greater mean peak velocity through the left on inspiration. This was not seen in any of the in vitro results and is perhaps a result of the probe being positioned eccentric to the expiration jet. As was seen in the raw data plot the female subject presents much higher velocities during expiration than the male subject. The inspiration mean peak velocities are much closer in magnitude. The mean peak velocities measured during the in vivo experiments show a slightly larger but similar range to the in vitro results as illustrated in Figure 51.

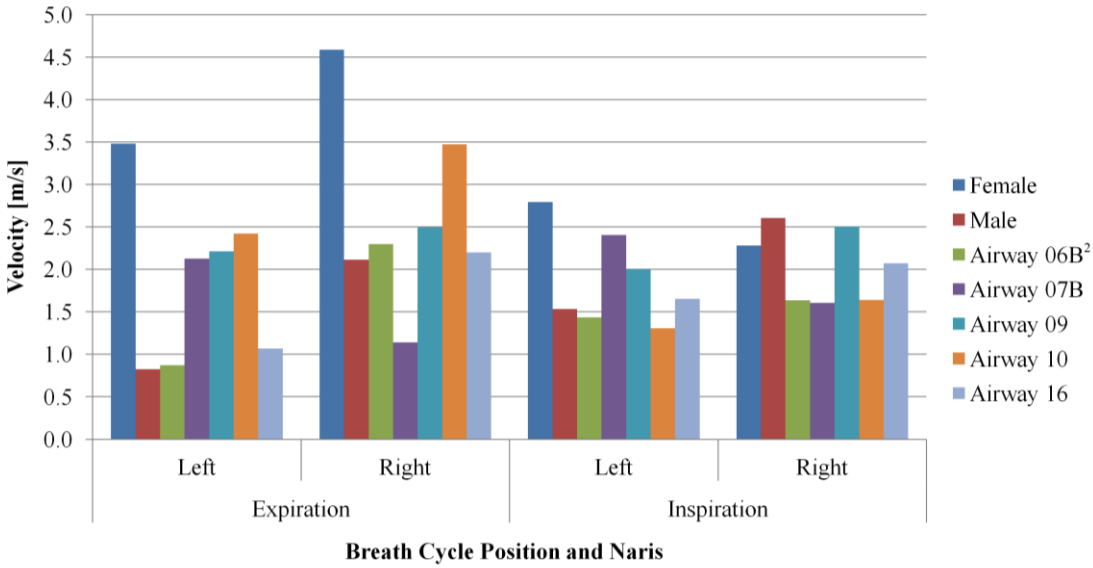

Figure 51: Comparison of in vivo mean peak velocity results to in vitro for each naris at peak expiration and inspiration.

The turbulence intensities calculated for peak expiration and peak inspiration from the in vivo data are plotted in Figure 52. As for in vitro turbulence intensities at the nares the peak inspiration values are lower than peak expiration. The range seen in vivo is however smaller than in vitro with a maximum turbulence intensity of 28.6% seen at peak expiration. Again it can be derived that the mean peak velocity observed at the naris does not give an indication of the turbulence intensity.

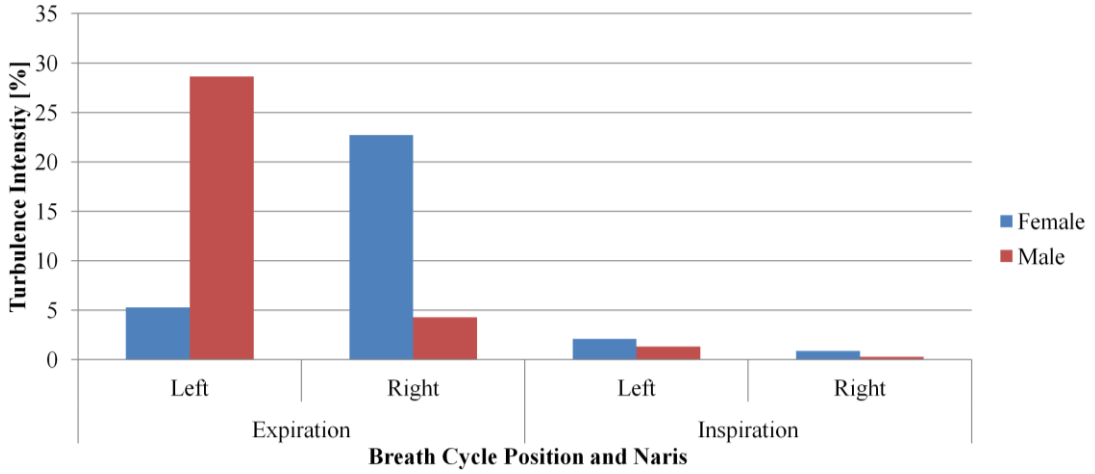

Figure 52: Comparison of the turbulence intensities seen at the nares of each in vivo subject during both peak expiration and inspiration.

Both peak inspiration and peak expiration in vivo turbulence intensities are similar to in vitro, as shown in the comparison of Figure 53. For peak expiration results from the male subject's left naris showed the highest in vivo turbulence intensity of 28.63%. The maximum in vivo turbulence intensity during peak inspiration of 2.10% was conversely seen at the left naris of the female subject. The in vivo levels observed are all within the range found in vitro at the mid to low end. This may be the result of slight differences in the in vivo testing conditions in particular the positioning of the probe further from the nares than in vitro. This was necessary to prevent possible damage to the probe due to movement of the subjects' heads. Positioning of the probe at a slightly farther distance from the nares would be expected to reduce the level of turbulence measured particularly for expiration, as the farther from the naris the lower the flow momentum and wider the jet. Another contributing factor is the more erratic nature of the raw in vivo data. Determination of the peak expiration and inspiration regions was far more difficult for these data sets as each curve was unique and, as was the case for expiration, the peaks were hard to identify amongst the turbulent noise. Subsequently, the regions chosen may not be analogous to those used to determine the turbulence intensities for the in vitro experiments. An observer bias may have also affected the results as regions were chosen based on how 'average' they appeared, thus noisier regions were avoided. It is also possible that the differences in rigidity and surface roughness of the nasal vestibule and valve between the rigid models and live subjects affected the hot wire anemometry measurements and caused the in vitro turbulence intensities

to be greater. This however cannot be confirmed as the rigid models are all of anonymous origin and too many other variables such as tidal volume and breathing frequency are present during in vivo experiments. The presence of higher temperatures in the in vivo expiratory flows may also help to suppress turbulence due to an increase in viscosity, however any viscosity increase would be slight as the higher humidity also present would prevent large viscosity increases (Tsilingiris, 2008).

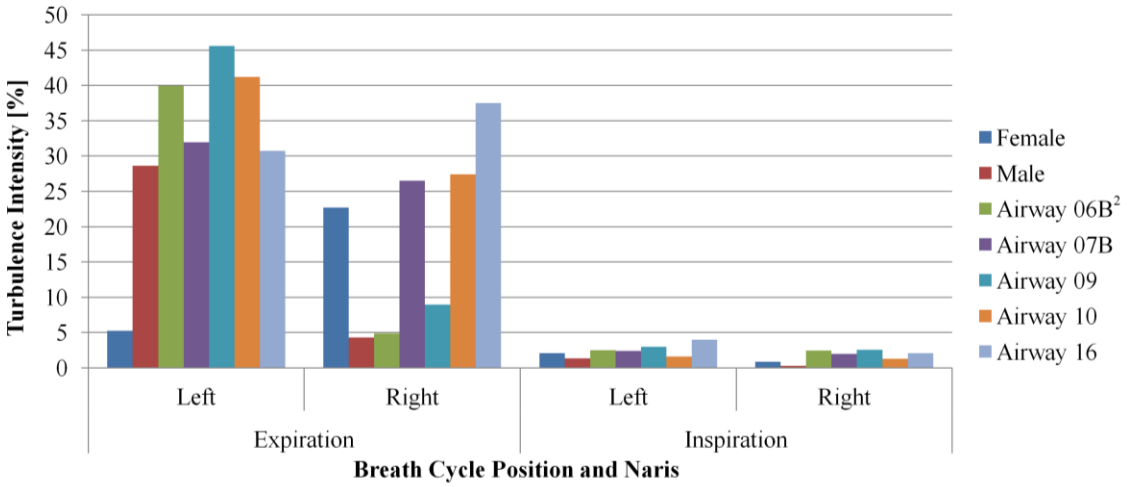

Figure 53: Comparison of in vivo turbulence intensities to in vitro for each naris at peak expiration and inspiration.

In vivo results show similar patterns of high turbulence intensity during peak expiration and low during peak inspiration. The magnitudes of peak expiration turbulence intensities however are slightly lower in vivo than in vitro though in vivo levels still fit within the range seen in vitro. Again, there was no observable correlation between the mean peak velocities and the levels of turbulence intensity at each naris.

8.4.2 Velopharynx Traverse Measurements

Results from the airway 06B[1] anterior to posterior velopharynx traverse were analysed to extract the peak expiration and inspiration mean velocities and turbulence intensities for each of the 19 measurement positions. Figure 54 illustrates the location of the traverse line, shown in green, on a silhouette image of the airway 06B profile. The green line spans the entire anterior to posterior length of the velopharynx at the centre of the cross section, with the anterior and posterior sides marked with the letters A and P respectively.

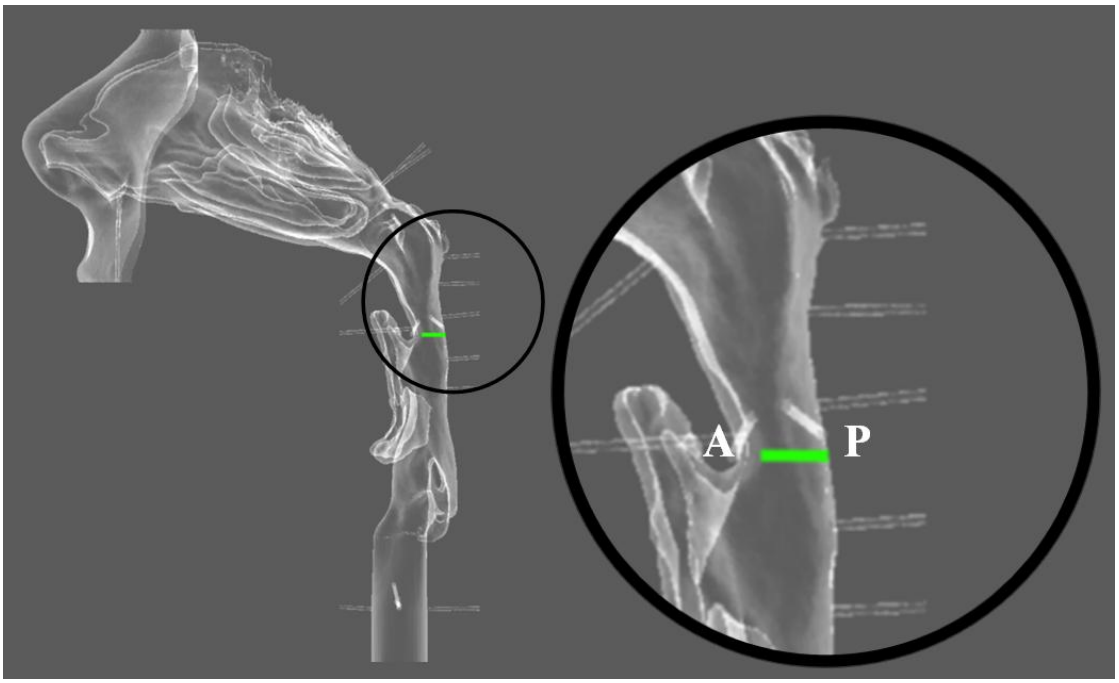

Figure 54: Airway 06B silhouette illustrating position of traverse path used for in vitro velopharynx hot wire anemometry experiments.

The mean peak velocities measured across the velopharynx traverse for peak expiration and peak inspiration during natural breathing are shown in Figure 55 with the distance from the anterior wall normalised by the length of the traverse so that 0 represents the anterior wall and 1 the posterior wall. A maximum mean velocity of 3.82 m/s was observed along the traverse during peak expiration whilst a smaller maximum of 3.02 m/s was measured during peak inspiration.

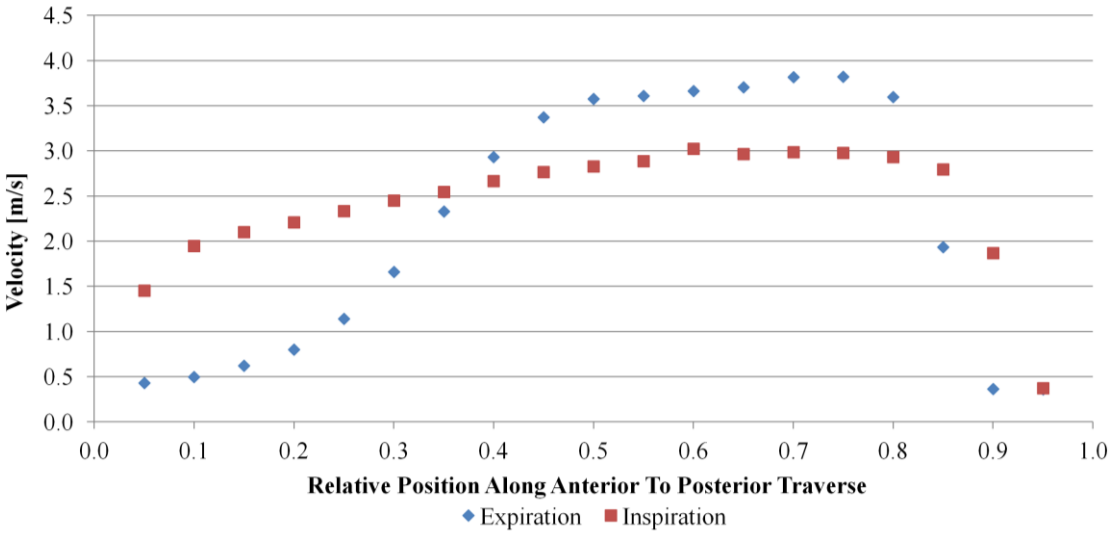

Figure 55: Velocity profiles during both peak expiration and inspiration of natural breathing across the anterior to posterior velopharynx traverse where 0 represents the anterior wall and 1 the posterior wall.

During inspiration the velocity profile has a more even distribution across the traverse when compared to expiration which exhibits a bias towards the central to posterior region of the

velopharynx. This result agrees with the steady state CFD work of Stringer et al. (2010), as mentioned in the static pressure results section, which illustrated inspiration flow distributed across the velopharynx while expiration flow was concentrated in a jet-like stream toward the posterior wall of the pharynx. Greater velocities through the velopharynx were achieved during peak expiration in comparison to inspiration despite peak inspiration reaching higher flow rates. These higher velocities during expiration were also observed in the steady-state CFD study of Stringer et al. (2010) as illustrated in the CFD results of Figure 56 which show the velocity profile through the same airway 06B geometry at a sagittal section. The velocity magnitudes measured via hot wire anemometry are not as high as those found in the CFD analysis as a result of the CFD study being steady-state and employing different peak flow rates to those employed for the in vitro experiments. Significantly higher peak flow rates were used in the CFD study for expiration with a value of 32 m/s as opposed to the in vitro peaks of 13.5 m/s.

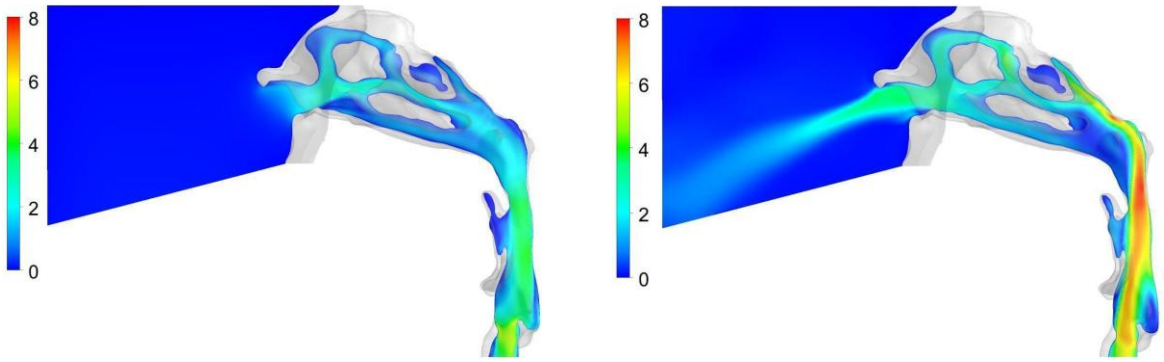

(a) **(b)**

Figure 56: Velocity map across sagittal section of the same airway 06B geometry as found by steady-state CFD analysis for (a) peak inspiration flow rate of 22 m/s; and (b) peak expiration flow rate of 32 m/s (adapted from Stringer et al. (2010)).

With the introduction of Optiflow™ NHF therapy there is little change to the expiration velocity profile, as shown in Figure 57 which gives the expiration velocity profiles for natural breathing and all Optiflow™ NHF flow rates tested. With increasing levels of NHF therapy reductions are observed in the velocities in the centre of the velopharynx and dramatic increases in velocities are seen at the two most posterior measurement positions. The anterior region also shows decreasing velocities with increasing NHF flow rates for all except the maximum 70 LPM. This result infers that the flow of NHF produces more resistance at the anterior and central regions of the velopharynx, pushing the expiration jet closer to the posterior wall. The maximum mean peak velocity measured along the traverse shows very little variation from 3.82 m/s during natural breathing to 3.71 m/s during breathing with 70 LPM NHF therapy.

On inspiration the changes to mean peak velocity are similarly small as given in Figure 58. With increasing levels of NHF therapy the velocity bias moves slightly further toward the posterior of the

velopharynx with small reductions in velocity at the anterior and slightly larger increases near the posterior. The use of NHF therapy projects the flow of air further toward the posterior with increasing flow rate. Contrary to expiration, during inspiration the maximum mean peak velocity along the traverse increases significantly from a natural breathing value of 3.02 m/s to 3.55 m/s for breathing with 70 LPM NHF therapy.

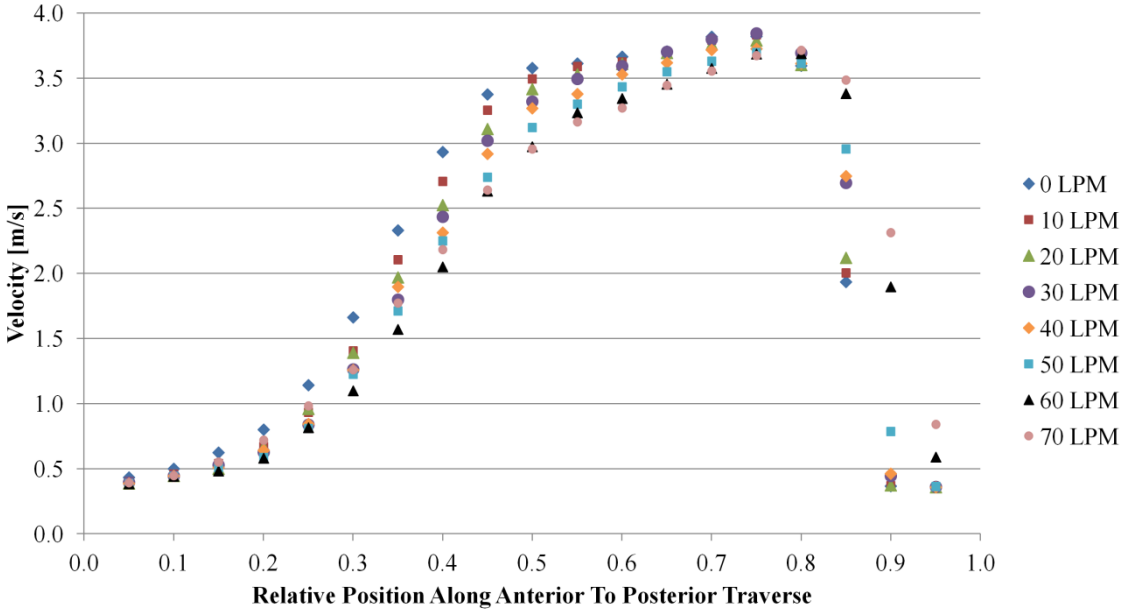

Figure 57: Peak expiration velocity profile across the anterior to posterior velopharynx traverse for natural breathing and breathing with Optiflow™ NHF therapy flow rates from 10 to 70 LPM.

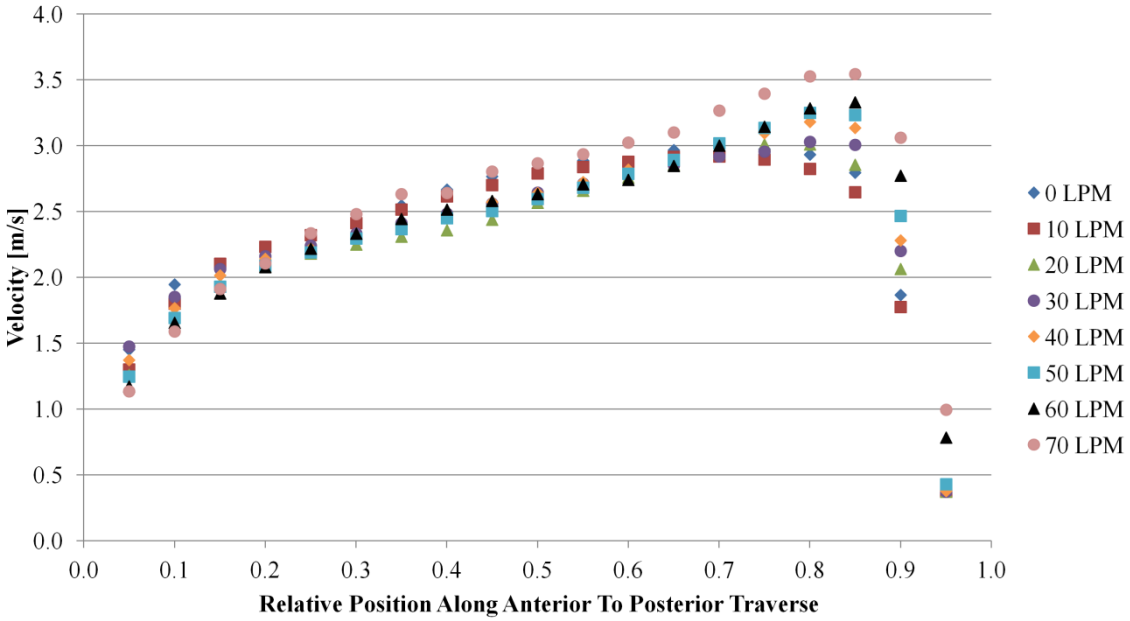

Figure 58: Peak inspiration velocity profile across the anterior to posterior velopharynx traverse during natural breathing and breathing with Optiflow™ NHF therapy flow rates from 10 to 70 LPM.

The turbulence intensity profiles along the velopharynx traverse for peak expiration and inspiration during natural breathing are displayed in Figure 59. As was seen in the measurements at the external nares very high turbulence intensity levels are achieved during peak expiration in comparison to the relatively low levels for peak inspiration. The peak inspiration turbulence intensity profile is reasonably flat with peaks of 9% and 12% near the anterior and posterior walls which may indicate a turbulent boundary layer. During peak expiration flow high levels of turbulence intensity, with a maximum of 55%, were observed near the anterior velopharynx. The turbulence intensity distributions along the traverse for both peak expiration and inspiration also agree well with the steady state CFD results of Stringer et al. (2010) who mapped the turbulent kinetic energy (TKE) in a sagittal section as shown in Figure 60. These maps show that in the region of the velopharynx traverse there is very low, uniform TKE during inspiration and high TKE concentrated at the anterior and decreasing toward the posterior during expiration. The level of turbulence intensity during peak expiration exceeded that of peak inspiration for all traverse positions except the two most posterior.

Examination of the airway geometry shows that the airway has a smooth contraction toward the velopharynx immediately above the traverse thus producing only low levels of turbulence intensity across it during peak inspiration. In the region below the velopharynx an irregular cavity is formed by the uvula, tongue and epiglottis on the anterior wall of the oropharynx. As the expiratory flow passes into the pharynx from the opening of the larynx in the anterior wall, the protrusion of the epiglottis further directs the jet toward the posterior. Above the epiglottis there is a sudden expansion into this aforementioned anterior oropharyngeal cavity promoting flow separation and turbulence. Turbulence is further exacerbated by the downward protrusion of the uvula into the anterior of the expiration jet path just below the velopharynx. This protrusion disrupts the expiration flow as it passes through the oropharynx into the velopharynx. These irregular geometrical features induce the high levels of turbulence measured in the anterior region of the velopharynx traverse. Less turbulence is seen during peak expiration from the centre to posterior of the traverse as the posterior pharynx has a much smoother form. The effect of this anterior oropharyngeal cavity on the turbulence during peak inspiration cannot be determined from the velopharynx traverse; however it is known from the static pressure experiments that a large pressure drop is seen between the trachea and velopharynx during peak inspiration and it is likely that this is in some part due to turbulence generated by this region, in particular the protrusion of the epiglottis.

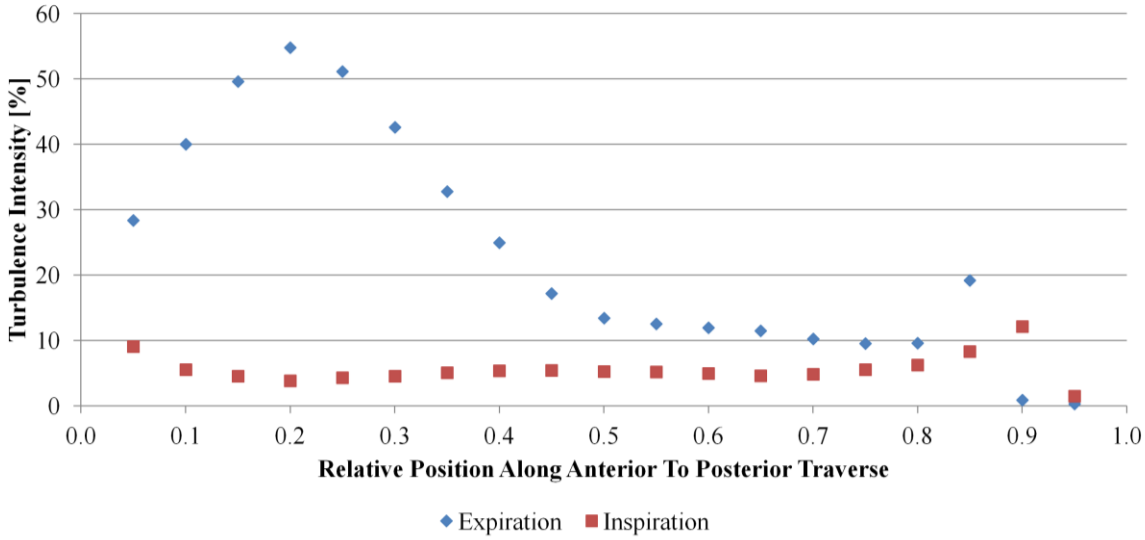

Figure 59: Turbulence intensity profiles during both peak expiration and inspiration of natural breathing across the anterior to posterior velopharynx traverse where 0 represents the anterior wall and 1 the posterior wall.

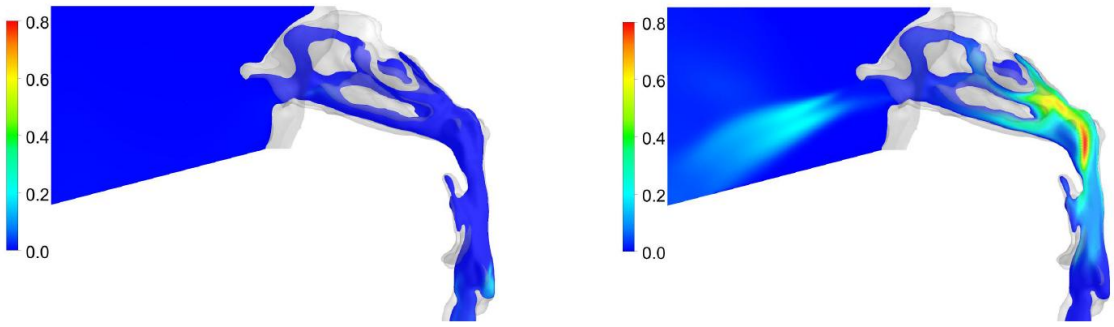

(a) **(b)**

Figure 60: Map of turbulent kinetic energy, in $m^{-2}s^{-2}$, across sagittal section of the same airway 06B geometry as found by steady-state CFD analysis for (a) peak inspiration flow rate of 22 m/s; and (b) peak expiration flow rate of 32 m/s (adapted from Stringer et al. (2010).

Figure 61 shows that the introduction of NHF therapy generated little difference in the turbulence intensity profile measured along the velopharynx traverse during peak expiration. Increasing flow rates of NHF see a small reduction in the turbulence intensity near the anterior wall and an increase near the posterior. The peak of the turbulence intensity profile rises in magnitude with increasing NHF until it reaches a maximum of 59% at 40 LPM following which it begins to decline again. In the centre of the velopharynx higher NHF therapy levels gives generally greater turbulence intensity though this becomes less prominent further toward the posterior. When considering the mean velocities it can be deduced that the increase in the peak turbulence intensity occurs due to a significant decline in the mean velocity at this point without an equivalent decline in the rms velocity. That is to say that at this point the rms velocity did not increase significantly with increasing NHF

flow rates to provide higher turbulence intensity rather that the mean velocity decreased. The relative changes in turbulence intensity in the velopharynx during expiration with the use of NHF are low and thus is not likely a major contributor to the CO_2 washout achieved by the Optiflow™ NHF therapy.

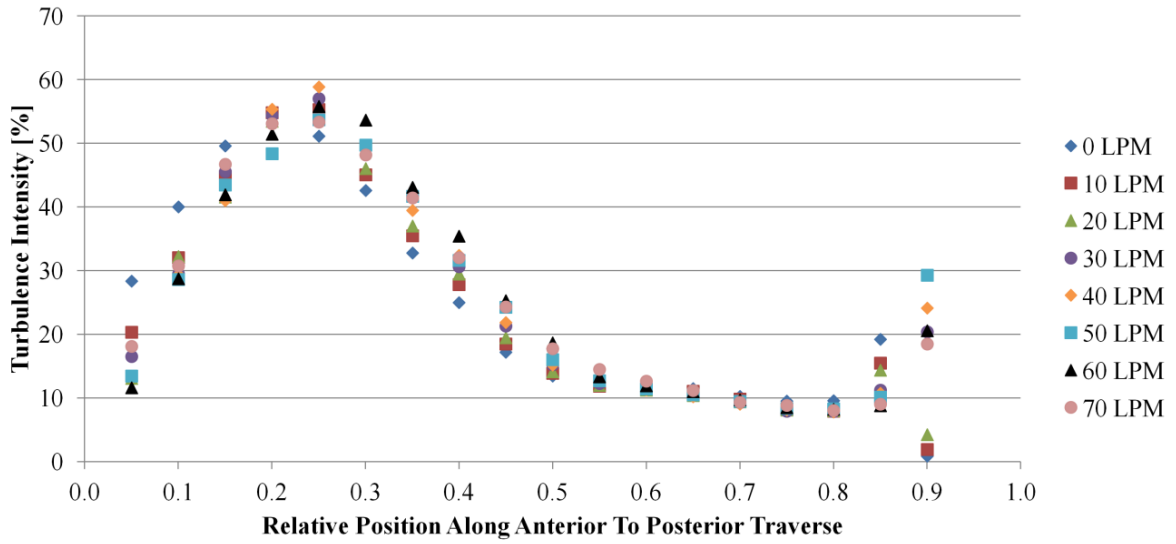

Figure 61: Peak expiration turbulence intensity profiles across the anterior to posterior velopharynx traverse during natural breathing and breathing with Optiflow™ NHF therapy flow rates from 10 to 70 LPM.

The changes to turbulence intensity during peak inspiration show a more uniform increase across the entire anterior to posterior traverse with increasing NHF flow rates as shown in the plot of Figure 62. Again much greater increases are observed near the walls, the posterior wall in particular which rises from 1.5% during natural breathing to 51% with 70 LPM NHF. Away from the walls an average increase in turbulence intensity of 11% is seen between breathing naturally and breathing with 70 LPM NHF. Considering the relatively low levels of turbulence observed during natural breathing this is not an insignificant increase, more than tripling the natural breathing peak inspiration average turbulence intensity. Though this increase in turbulence is unlikely to significantly improve the CO_2 flushing of the upper airway as it occurs during inspiration, the promotion of mixing may still prove beneficial by diluting any remaining pockets of CO_2 rich gases which could be re-inhaled.

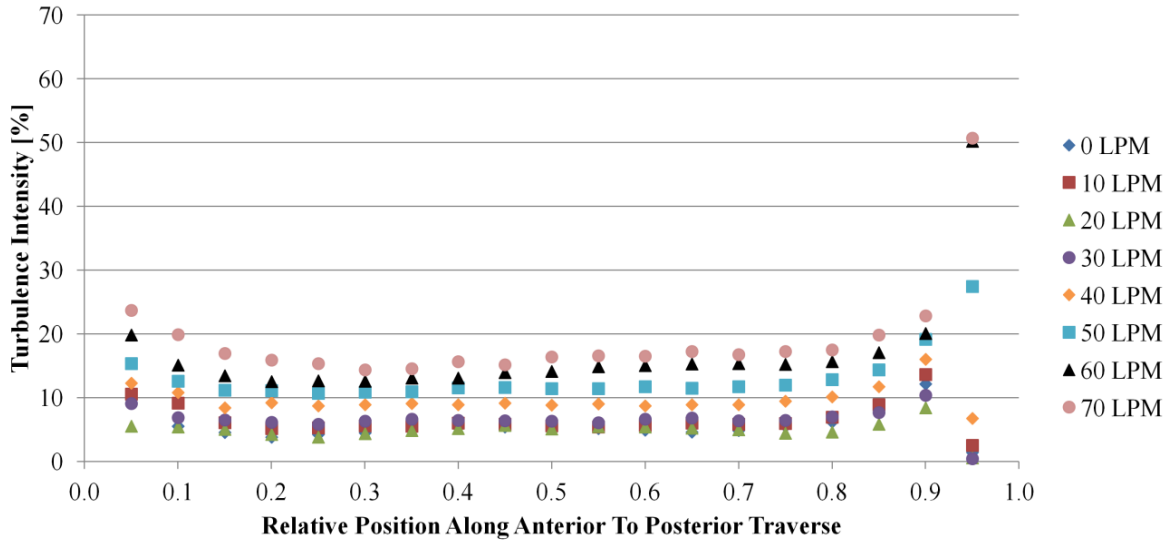

Figure 62: Peak inspiration turbulence intensity profiles across the anterior to posterior velopharynx traverse during natural breathing and breathing with Optiflow™ NHF therapy flow rates from 10 to 70 LPM.

8.5 Conclusions

Hot wire anemometry was employed to measure velocities at the nares of the five unique airway models and two live subjects during natural breathing. Further measurements were carried out along an anterior to posterior traverse of the airway 06B[1] velopharynx for natural breathing and breathing with Optiflow™ NHF therapy. From these measurements mean peak velocities and turbulence intensities could be extracted.

The greatest mean peak velocities observed at the exterior nares occurred during peak expiration for both in vitro and in vivo experiments, attributed to the presence of a high velocity jet focussed from the nasal valve on expiration as opposed to a more uniform velocity profile on inspiration. A larger range of mean peak velocities were also seen during peak expiration than peak inspiration. It is believed that this is a result of the approximately central placement of the probe not coinciding with the centre of the expiratory jet for all nares. Maximum mean peak velocities of 3.47 and 2.50 m/s were seen for expiration and inspiration respectively across the five in vitro airway models. In vivo, the female subject exhibited very high mean peak velocities during expiration with a maximum of 4.59 m/s. The naris which presented the highest velocity during expiration also produced the highest inspiration velocity for all in vitro experiments but only one of the two in vivo experiments. This implied that the path of least resistance through the two nasal cavity sides was the same in both flow directions, agreeing with the findings of the in vitro pressure investigations. A range of low to high levels of turbulence intensity were observed at the exterior nares during peak expiration for both in

vivo and in vitro conditions whilst peak inspiration produced low turbulence intensities. No discernible relationship could be found between the peak velocities and turbulence intensities measured at each individual naris.

During natural breathing flow conditions the anterior - posterior traverse of the velopharynx found a more even velocity distribution at peak inspiration and higher maximum velocities during peak expiration. This aligned with the steady-state CFD findings of Stringer et al. (2010) where a high velocity jet was observed through the pharynx for expiration only. The introduction of NHF therapy had little influence on the velocity profiles, inducing a slight shift in the velocity distribution toward the posterior with increasing flow rates for both peak expiration and inspiration. Similarly, the expiration turbulence intensity profile was little affected by the introduction of NHF therapy, with increasing flow rates producing a slight decrease near the anterior wall and increase in the central to posterior region whilst the peak turbulence intensity remained in a constant location and was at a maximum for 40 LPM NHF. A more uniform increase was observed during peak inspiration with the average turbulence intensity away from the walls increasing triple fold between the conditions of natural breathing and breathing with 70 LPM NHF therapy. Though the changes in turbulence intensity with increasing levels of NHF therapy were small for peak expiration and are thus unlikely to contribute significantly to washout effects, the considerable increases in peak inspiration turbulence intensity may assist in diluting any CO_2 retained in the anatomic dead space. It is also possible that in other regions of the upper airway the use of NHF therapy produces much greater increases in turbulence intensity not observed in these experiments which may contribute to mixing and CO_2 washout.

9 Carbon Dioxide Washout of Anatomic Dead Space

Carbon dioxide is constantly produced within human body cells as a waste product of cellular respiration. It is continuously delivered to the lungs for expulsion in the venous blood, or deoxygenated blood, where it passes through the pulmonary capillaries which cover the alveoli. Diffusion of the CO_2 from the blood into the alveoli is driven by the pressure gradient across the interstitial respiratory membrane, such that CO_2 diffuses into the lungs to attain an equilibrium concentration. When at rest, the deoxygenated blood entering the pulmonary capillaries has a CO_2 partial pressure of 45 mmHg and an O_2 partial pressure of 40 mmHg (Tortora and Derrickson, 2006). Within the alveoli the partial pressures of CO_2 and O_2 respectively are 40 and 105 mmHg (Tortora and Derrickson, 2006). Following gas exchange, the partial pressures within the oxygenated blood leaving the pulmonary capillaries have changed to 40 mmHg of CO_2 and 100 mmHg of O_2 (Tortora and Derrickson, 2006). This results in a CO_2 concentration of 5.2% in the lungs. For an average human adult the diffusion rate of CO_2 into the lungs occurs at 200 ml/min (Widmaier et al., 2011). This is equal to the diffusion rate of O_2 into the pulmonary blood when at rest (Tortora and Derrickson, 2006).

For those subjects suffering from respiratory distress, attaining the level of respiratory ventilation required to maintain this equilibrium of concentrations is difficult and can result in hypoxemia, low oxygen levels in the arterial blood. These patients require some form of ventilation therapy, such as Optiflow™ NHF, to reduce the stress on the body and achieve a healthy level of blood oxygenation. Optiflow™ NHF therapy has been shown to improve the blood oxygenation levels of patients suffering from mild to moderate respiratory distress as effectively as the more established full face mask oxygen therapy. Moreover, use of Optiflow™ NHF therapy has a greater level of patient compliance to the therapy regime. Though it has been proven to improve blood oxygen saturation, the mechanisms by which this is achieved are still unproven.

The main proposed mechanism, investigated by the experiments laid out in this chapter, is the CO_2 washout of the anatomic dead space. If regions of the conducting airways are continuously flushed with fresh air by NHF therapy, then the ratio of alveolar gas to air that is contained in the conducting airways over the course of a breath cycle is reduced. This equates to a reduction in the average concentration of CO_2 and an increase in the average concentration of O_2 maintained in the airway over the breath cycle. Subsequently, the higher concentration of O_2 residing in the conducting airways at the onset of inspiration will increase the partial pressure of O_2 in the lungs thus improving the rate of gas exchange across the alveolar wall. Similarly the lower concentration of CO_2 in the conducting airways results in a decrease of the partial pressure of CO_2 in the lungs, increasing the diffusion rate of CO_2 into the lungs.

The reduction of the CO_2 concentration and the resulting increase in O_2 concentration within the conducting airways can also be seen as an apparent reduction in the anatomic dead space. As some volume of alveolar gases are flushed out and replaced with NHF gases, the fresh air is apparently closer to the lungs and thus the anatomic dead space is decreased. The two in vitro experimental methods, Experimental Methods Version One and Two, employed to determine the CO_2 dead space washout and the influence of Optiflow™ NHF are described in the following sections. For both methods air was employed as the NHF therapy gas as measurement of CO_2 washout was the major experimental focus and the use of O_2 or an air-oxygen mix could not reasonably be thought to have a significant influence on the CO_2 concentrations observed. Performing these experimental methods in vitro allowed for much greater variable control and prevented certain complications associated with in vivo measurements such as the physical inaccessibility of airway regions and uncontrollable breathing patterns.

9.1 Experimental Method Version One

The first experimental method developed to examine the occurrence of anatomic dead space washout focused on measuring a CO_2 concentration rate of decay. As previously stated this experimental method was not intended to be true to the physiological process of respiration. Rather, this was an initial means of determining the relative efficacy of Optiflow™ NHF therapy at reducing the CO_2 level within the experimental system as opposed to operating the system as a naturally breathing adult. Two variations of the system setup were trialled for the CO_2 concentration decay, defined and described below as Set-up One and Two.

As these experiments were carried out early in the research the experimental respiratory system was in one of its early forms as described in the Chapter 5 with a larger than average FRC volume, some of which was contained within the connections between the pump and the model. Similarly, the breath flow waves used to drive the pump were the initial patterns derived directly from live subject measurements. These breath waves are described in detail in Chapter 6. Only two breathing cases were examined, natural breathing and a single, midrange NHF therapy flow rate of 30 LPM for testing NHF efficacy. For the 30 LPM NHF therapy case the pump was driven by the Fourier series derived from measurements on the live subject experiencing the same level of NHF therapy. For the experiment with no Optiflow™ NHF therapy in use the original natural breathing flow wave, tidal volume of 799 ml and breathing period of 5.08 seconds, was employed to drive the pump. To test the fidelity of the experimental method the natural breathing test performed with Set-up Two was repeated a total of six times for comparison.

9.1.1 CO_2 Concentration Decay Experimental Procedure

Set-up One

To prepare the experiment using the first setup the pump piston was retracted to give the largest possible volume of 5.84 litres within the entire experimental system. The pump and the step down connections were isolated from the later connections and airway model as illustrated in Figure 63. The volume was then sealed off and the ball valve from the CO_2 feed system into the pump was opened. Initially the line from the CO_2 rotameter to the pump ball valve was broken so that any CO_2 feed would not pass into the pump while stabilising the CO_2 flow. The CO_2 feed was adjusted until a desired flow rate was achieved, then allowed to stabilise. The required volume of CO_2 was then introduced by reconnecting the feed line, allowing CO_2 flow into the pump for a specified time period followed by closing off of the ball valve. This method allowed for introduction of CO_2 to give a concentration of close to 2000 ppm (0.2 % V/V), the limit of the sensor used for the experiments. Set up of the system was then completed by unsealing the connections to the pump outlet and reattaching the rest of the experimental system.

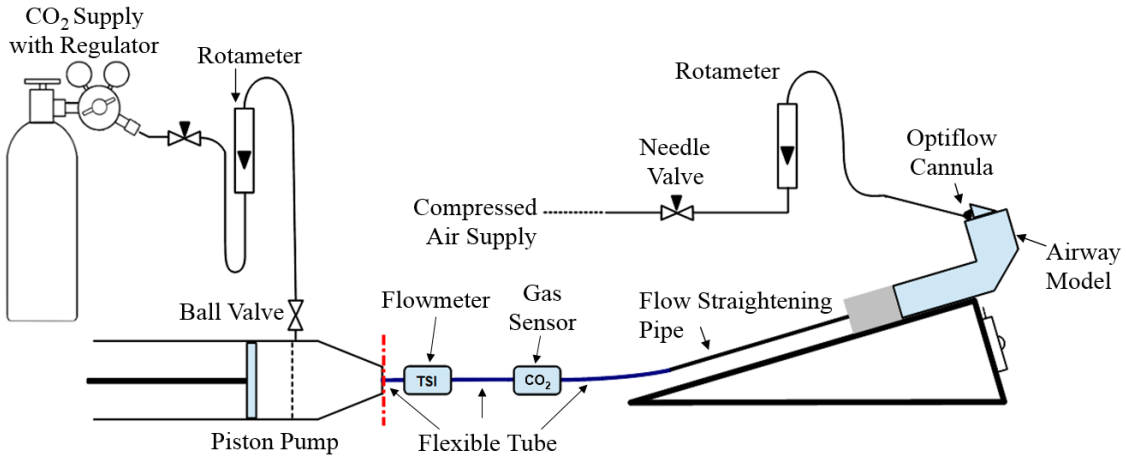

Figure 63: Set-up One schematic illustrating by the dashed red line the point of isolation of the pump and step down connections.

For measurements in which Optiflow™ NHF therapy was applied to the model, the cannula was set up on the model and the NHF flow rate established before the pump was reconnected to the rest of the system to avoid any delays post reconnection.

Set-up Two

The second experimental setup procedure was almost identical to that of the first, with all the steps from Set-up One carried out except for placement of the cannula on the model. Once CO_2 had been

introduced to the pump and the system components all reconnected, one further step was taken. The piston was advanced to provide the smallest possible volume within the system, at 3.58 litres, while simultaneously flushing the downstream connections and components with the increased CO_2 concentration air. To prepare for the measurements with Optiflow™ NHF therapy the cannula flow rate was established prior to placing the cannula on the model, which was carried out only once the above steps were complete.

9.1.2 Data Acquisition

Experiments were begun immediately after all preparation steps had been finalised to prevent unwanted gas mixing by diffusion. Data acquisition from the gas sensor and flow meter were initiated at a sampling frequency of 100 Hz followed by starting of the pump. The system was allowed to run until the CO_2 concentration decay had plateaued and a level of less than 600 ppm (0.06 %V/V) was achieved. The concentration of CO_2 in the earth's atmosphere is approximately 400 ppm (Wayman et al., 2013) however this level can be much higher in inhabited buildings, thus the lower limit of 600 ppm was chosen as it was the lowest level which was consistently attainable in the experimental area.

9.1.3 Data Processing

Initially it was thought that the measured data from different experimental runs could be directly compared to one another. However it was soon obvious that due to the very low level of CO_2 introduced into the system, as restricted by the sensor range, there was significant variation in the concentration of CO_2 at the commencement of each individual experiment. The poor repeatability of the initial CO_2 concentration prompted a change in the method of data processing.

All concentration data was converted from units of ppm to %V/V for consistency with the later Experimental Method Version Two experiments. A reference level of initial CO_2 was then set at 0.08 %V/V at which point analysis of data would begin. The time taken, in seconds, for the CO_2 concentration to reach the second reference level of 0.06 %V/V was extracted from each data set. A theoretical time to attain the same reduction in concentration was also found assuming perfect mixing of inspired air with the rest of the system volume. This was calculated iteratively using equation [7] with variables V_s, the total system volume; V_t, the tidal volume; C_i, the average CO_2 concentration in the system at the beginning of breath cycle i, and C_a, the concentration of CO_2 in the room air. The equation states that during each breath cycle a portion of the total system volume, the tidal volume, is expelled via expiration and replaced with room air on inspiration. By assuming perfect mixing, the instantaneous CO_2 concentration within the system at the end of a breath cycle is therefore a weighted

average of the initial system concentration and room air concentration based on their relative volumes. An example of the results of the iterative calculation is graphed in Figure 64.

$$C_{i+1} = \frac{((V_s - V_t) * C_i + V_t * C_a)}{V_s} \quad [\ 7\ ]$$

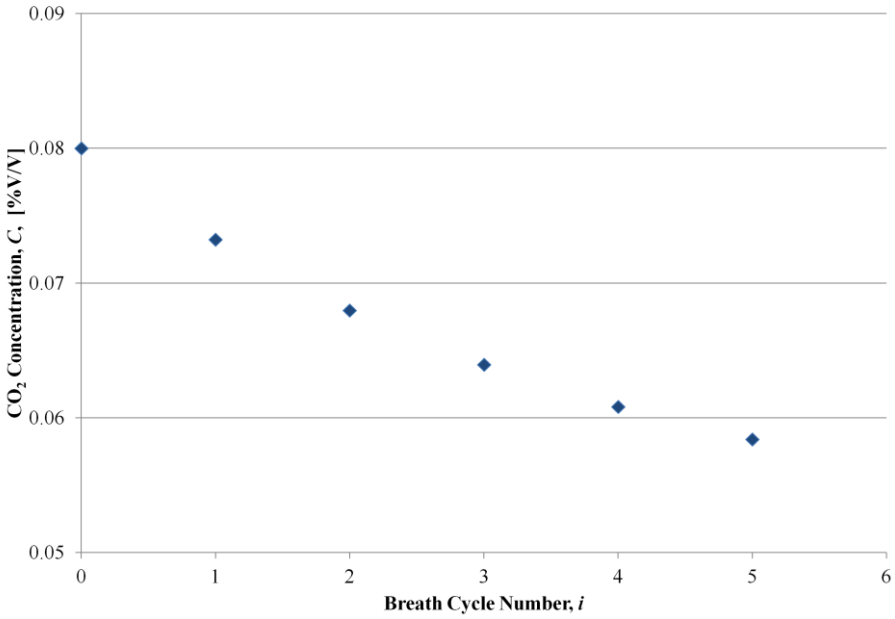

Figure 64: Example of the outputs from the iterative calculation using Equation [7] to find the number of theoretical breath cycles for a 0.08 to 0.06 %V/V CO_2 decay when assuming perfect mixing.

This calculation was carried out for all four experiment scenarios performed using Set-up One and Set-Up Two. When calculating the theoretical time for the two experiments in which NHF therapy was used at a flow rate of 30 LPM, the occurrence of dead space washout was ignored. Thus the only influencing factors providing difference to the four scenarios were the variation in pump volume between Set-ups One and Two, and the period of the breath cycle between natural breathing and breathing with the 30 LPM NHF therapy.

9.1.4 Results and Discussions

From the theoretical calculations it was found that only 8 breath cycles would be required to attain the reduction from 0.08 to 0.06 %V/V CO_2 in Set-up One when assuming perfect mixing. This was the case for both scenarios of natural breathing and breathing with 30 LPM NHF therapy, as the difference in the tidal volume between the two was small at only 15 ml. Despite requiring the same

number of cycles, the decay time is slightly higher for the 30 LPM NHF therapy scenario as the breath period is longer than that of natural breathing. For Set-up Two the theoretical decay times were reduced to a mere 5 breath cycles for both breathing with 30 LPM NHF and natural breathing due to the reduction in the system volume. These results and the times are listed in Table 5 alongside the results extracted from the experimental data.

It was immediately apparent from the results of these experiments that metering a preset volume of CO_2 into the pump volume could not be repeated accurately. Consequently it was necessary to set an upper limit attained by all experiments from which the time analysis could be started. Figure 65 shows the full time series of the four decay experiments, with all reaching levels above 0.08 %V/V upper limit.

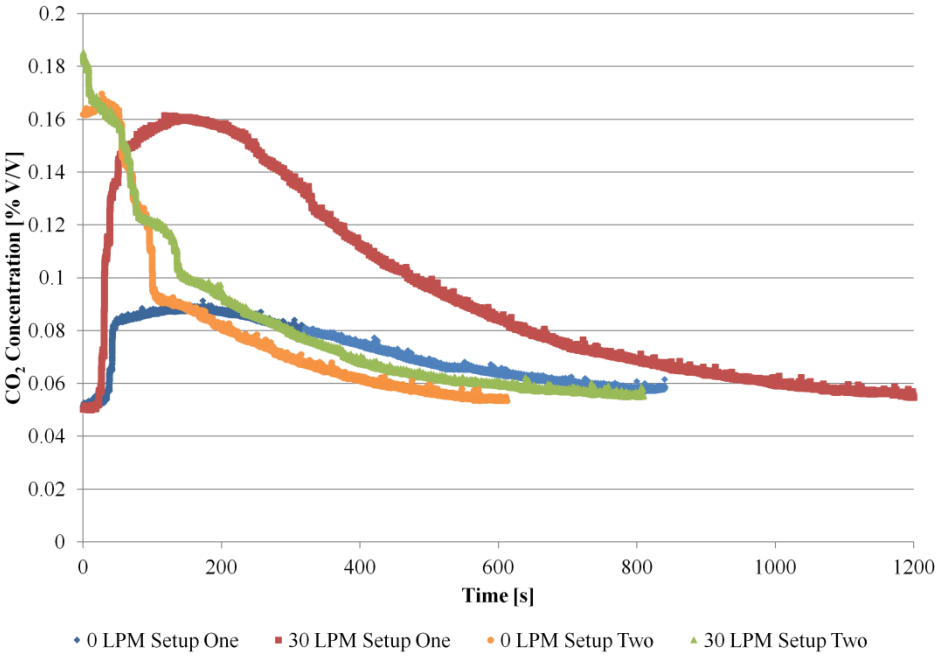

Figure 65: Full time series of CO_2 concentration decay results from experimental Set-ups One and Two.

Figure 66 shows all experiments with results beginning at the upper limit of 0.08 %V/V. In this plot the most significant observable difference is between the two setups used, with the Set-up Two results decaying to the lower limit much faster than the two datasets obtained using Set-up One. For Set-up One alone the use of NHF therapy at 30 LPM accelerated the rate of decay to a small extent when compared to the natural breathing case. Conversely, in Set-up Two the use of NHF therapy decreased the rate of CO_2 decay when compared to the natural breathing result.

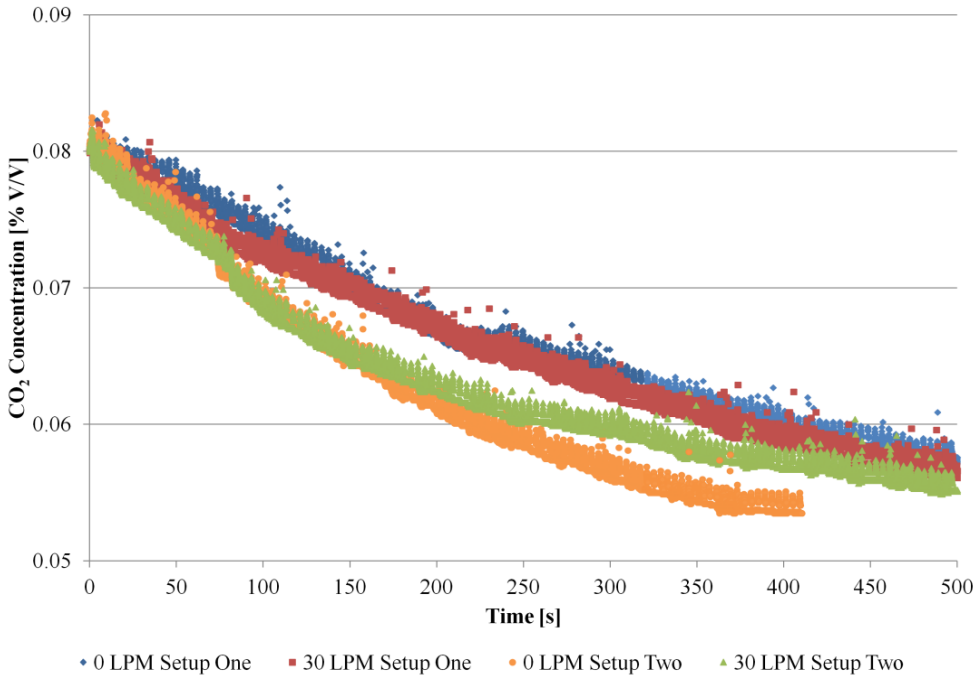

Figure 66: CO_2 decay curves of both Set-up One and Two beginning at upper limit of 0.08 %V/V.

The times taken for each experiment to decay from 0.08 to 0.06 %V/V CO_2 were extracted and are given in Table 5. Comparisons between the theoretical and experimental decay times show extreme differences with experimental times an order of magnitude greater than those calculated. It was not expected that perfect mixing would occur within the system and these large disparities show definitively that this assumption is inadequate.

Table 5: Theoretical and experimental CO_2 concentration decay results.

	Set-up One		**Set-up Two**	
	0 LPM NHF	**30 LPM NHF**	**0 LPM NHF**	**30 LPM NHF**
Breath Cycle Period	5.08 s	6.63 s	5.08 s	6.63 s
Tidal Volume	0.799 l	0.814 l	0.799 l	0.814 l
Theoretical Number of Cycles for Decay	8	8	5	5
Actual Number of Cycles for Decay	76.43	53.57	42.22	39.84
Theoretical Decay Time	40.64 s	53.04 s	25.40 s	33.15 s
Actual Decay Time	388.26 s	355.17 s	214.46 s	264.17 s
Actual Total Volume Exchanged	59.20 l	43.96 l	33.73 l	32.56 l

Comparison of the results from Set-up One show that the introduction of NHF therapy did reduce the time for CO_2 decay from 388.26 seconds for natural breathing to 355.17 seconds. The total volume exchanged to achieve this decay was also reduced by 15.25 litres. Set-up Two results also show a reduction in the total volume exchanged with the introduction of NHF; however, the decay time was faster for natural breathing. In spite of a lesser number of cycles and thus the lower volume exchanged with the introduction of 30 LPM NHF, the much shorter breath period of natural breathing produced a faster decay in this setup. As other contributing variables such as tidal volume differences were present in these experiments, the difference in the decay rates are most likely cumulative and not directly attributable to the introduction of NHF flow alone.

By comparing the results from the analogous experiments of Set-ups One and Two it is obvious that the system volume has a large influence on the rate of the CO_2 decay. The reduced system volume of Set-up Two resulted in much faster decay times of 214.46 seconds as opposed to 388.26 seconds and 264.17 seconds as opposed to 355.17 seconds for the natural breathing and 30 LPM NHF scenarios respectively. However there is no consistent reduction attributable to the use of NHF therapy in these four experiments.

Six repetitions of the Set-up Two natural breathing experiment were carried out to determine experimental repeatability, the results of which are plotted in Figure 67 with data all beginning at 0.08 %V/V. The figure shows that there are significant differences in the decay curves of the six experiments resulting in a wide variation of decay times. The decay times from the analysed curves are laid out in Table 6.

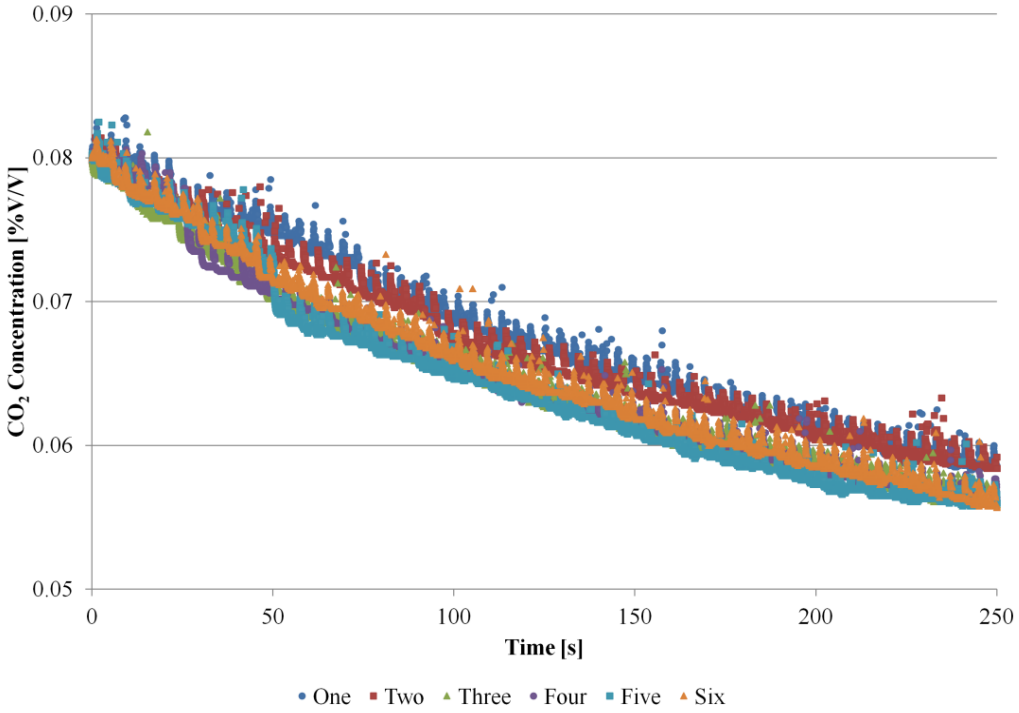

Figure 67: Repeatability tests of CO_2 decay during natural breathing using Set-up Two.

Table 6: Results of CO_2 decay repeatability experiments.

	One	Two	Three	Four	Five	Six
Actual Number of Cycles	42.22	42.16	32.62	34.36	31.93	35.06
Actual Decay Time	214.46 s	214.18 s	165.69 s	174.53 s	162.21 s	178.13 s
Total Actual Volume Exchanged	33.73 l	33.69 l	26.06 l	27.45 l	25.51 l	28.02 l

These repeatability results give an average decay time of 184.87 seconds with a standard deviation of 23.53 seconds for natural breathing with experimental Set-up Two. With the standard deviation this high, equal to 12.7% of the average value, the repeatability of these experiments is poor. It can also be seen in Figure 65 to Figure 67 that there are noticeable step changes in the CO_2 concentration curves. These step changes result from the low response rate of the sensor which was unable to accurately capture the decay. As a consequence of these issues, the non-physiological experimental system volume and the non-physiological introduction of CO_2 as a single fixed volume as opposed to a continuous flow, these results were concluded to be of little practical use. Subsequently Experimental Method Version One was not pursued further in favour of developing and using the physiologically representative Experimental Method Version Two.

9.2 Experimental Method Version Two

The second experimental method undertaken to investigate anatomic dead space washout was designed to replicate an average adult respiratory system and measure the time-averaged concentration of CO_2 at a single reference point within the conducting airways. This method would be capable of giving a clearer picture of what occurs in live subjects and how Optiflow™ NHF therapy influences the concentrations of CO_2 in the anatomic dead space. O_2 concentrations were also measured simultaneously for additional information. This method was used to determine whether Optiflow™ NHF therapy provided dead space washout and to what degree it did so for various levels of NHF therapy. Following this, further experiments were carried out to investigate how the efficacy of the therapy was itself affected by variation in the upper airway geometry variation.

The efficacy of Optiflow™ NHF therapy was the first experiment set carried out and the method used became the basis for all following tests in which the upper airway geometry variation was investigated. Measurements of the CO_2 and O_2 concentrations during natural breathing with the standard airway 06B model were carried out on each day of testing as a measure of experimental repeatability. The introduction of CO_2 into the system was found to be a likely source of error introduction due to the manual control of pressure and flow rate as well as the conversions required to account for the disparity between rotameter calibration and working fluid. Repeatability tests were subsequently considered an appropriate action to mitigate the risk of error introduction. The experimental system employed for these tests was as described in Chapter 5. The pump, set up to contain an average adult FRC volume of 2400 ml, was driven by the average adult breathing pattern with the 450 ml tidal volume and breathing rate of 14 breaths per minute for all Experimental Method Version Two CO_2 washout experiments.

9.2.1 Data Processing

Though the experimental methods varied slightly the process of data analysis remained constant for all results obtained, and will therefore be explained once here. As the CO_2 introduction into the system was continuous and constant throughout each ten minute experiment every dataset was checked to ensure that the overall CO_2 concentration trend was constant to confirm the system was in equilibrium throughout data capture. If a positive or negative trend was seen to be caused by a small region of data at the start of the set, the dataset would be cropped to leave the constant majority. However if the non-constant trend pervaded the entire dataset, experiments were repeated. As the response times of the new CO_2 and O_2 sensors were still in excess of the breath cycle period, direct comparison of the transient concentrations across a single cycle was impractical. Instead a temporal average was found

for each set of data providing an average CO_2 concentration at the measurement position for the particular state examined. The O_2 concentration data was processed using the same method.

9.2.2 Efficacy of Anatomic Dead Space Washout with Optiflow™ NHF Therapy

The first experiment undertaken was to determine the efficacy of anatomic dead space washout with the use of Optiflow™ NHF therapy and how the level of dead space washout was affected by the flow rate of NHF therapy employed. This set of experiments then became the basis of the further experiments performed for the investigation of upper airway geometry influences on therapy efficacy.

Experimental Procedure

To determine the efficacy of anatomic dead space washout when using Optiflow™ NHF therapy the following protocol was designed. An illustration of the experimental system employed is provided in Figure 68. As laid out in Chapter 5, calculations had to be carried out in order to determine the rotameter flow rate required to replicate the rate of CO_2 diffusion into the lungs. For an average person with an alveolar ventilation of 4000 ml/min, this rate is known to be approximately 200ml/min. Due to the calibration of the rotameter, adjustments had to be first be made for the calibration error, temperature dependent buoyancy of the CO_2 and back pressure of the compressed CO_2 source so that the flow rate could be set correctly. After calculation of the rotameter flow rate, the volume of the pump was set to the average adult FRC volume of 2400 ml by adjusting the piston position. The pump was started so that it was providing the oscillatory flows of an average adult, with a tidal volume of 450 ml and breathing rate of 14 breaths per minute. Starting the pump first prevented the CO_2 concentration from rising above the level found within an average pair of lungs while initiating and stabilising the CO_2 feed. To set the CO_2 feed rate the ball valve into the pump was opened, the gas cylinder turned on and the back pressure set to 50 PSIG. The flow rate through the rotameter was carefully metered to the calculated value with particular attention paid to maintaining the correct back pressure. Once set the flow rate, back pressure and pump CO_2 concentration were given at least five minutes to settle to equilibrium. The data acquisition system was set to log the gas sensor outputs of both the CO_2 and the O_2 concentrations at a rate of 100 Hz for ten minutes for each test.

A control experiment was carried out first with the system replicating a naturally breathing adult, with no cannula in place on the standard testing model airway 06B. Results from this test provided the baseline expectations for the gas concentrations. Experiments were then conducted with Optiflow™ NHF therapy applied to the model. NHF flow rates of 10 to 80 LPM were tested at intervals of 10 LPM to provide a map of the efficacy of CO_2 dead space washout as a function of NHF flow rate.

These tests at natural breathing and breathing with NHF flow rates from 10 to 80 LPM were then repeated on a further three separate days to determine the experimental repeatability.

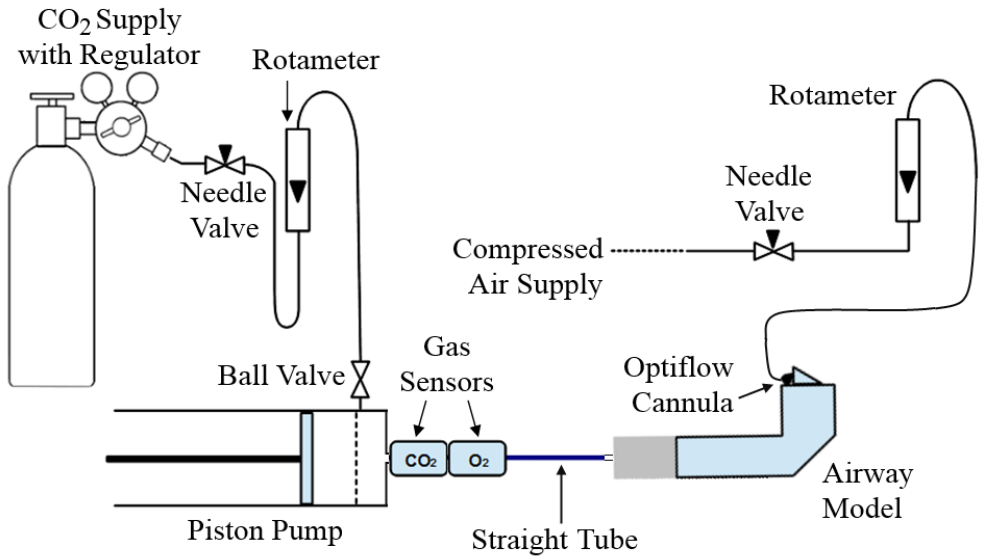

Figure 68: Experimental respiratory system schematic for Experimental Method Version Two.

Results and Discussions

For the first iteration of this experiment the CO_2 concentration outside the lung pump settled to an average value over many breath cycles of 4.85 %V/V during the replication of natural breathing. Introduction of Optiflow™ NHF therapy induced a reduction in this average concentration with higher flow rates providing lower average CO_2 concentrations. At the highest NHF flow rate employed of 80 LPM an average CO_2 concentration was measured as 3.84 %V/V. Further repetitions of the same experiment on three separate occasions showed a close agreement between the average CO_2 concentrations measured during natural breathing. Larger differences were seen between average concentrations observed during administration of Optiflow™ NHF therapy; however none of these exceeded 4.9% of the lowest measured average. The plot of Figure 69 shows the results from all four repetitions of the experiment, with horizontal error bars indicating the level of variation in the NHF flow rate supplied due to air supply instability.

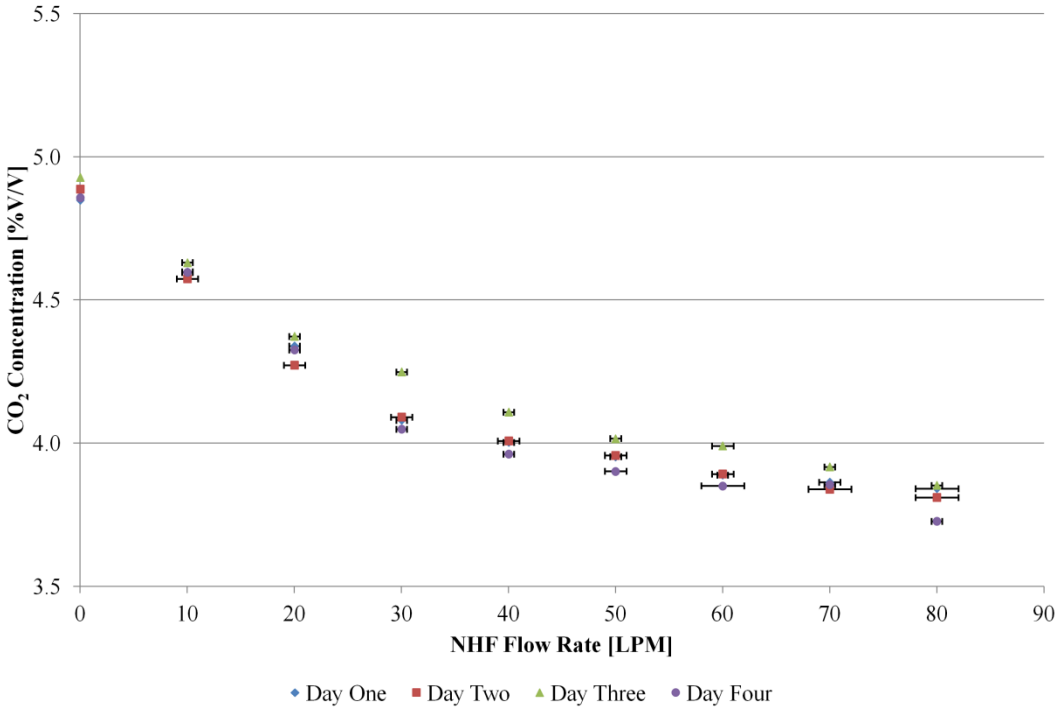

Figure 69: Time-averaged CO_2 concentrations during natural breathing and breathing with Optiflow™ NHF flow rates from 10 to 80 LPM showing experimental repeatability over four separate days of testing.

The results from these repeated experiments were used to determine a mean value for the average CO_2 concentration at natural breathing and for each flow rate of Optiflow™ NHF therapy. The variation observed in the concentrations over the four days of testing for the same breathing condition, natural breathing and for each specific level of NHF therapy, were then used to define an error for each. This was specified as two standard deviations of the repeatability results either side of the mean, with the standard deviation, σ, calculated using the formula of Equation [8] where x is the measured CO_2 concentration and $\bar{x}$ the mean CO_2 concentration. Figure 70 provides a plot of these mean CO_2 concentrations with the associated errors derived from the repeatability experiments. The trend of the mean CO_2 concentrations can be closely approximated by a second order polynomial within the range of breathing conditions tested. The second order polynomial fit, with an R-squared value of 0.99, is also plotted with the data in Figure 70.

$$\sigma = \sqrt{\frac{1}{n-1}\sum_{i=1}^{n}(x_i - \bar{x})^2} \qquad \textbf{[8]}$$

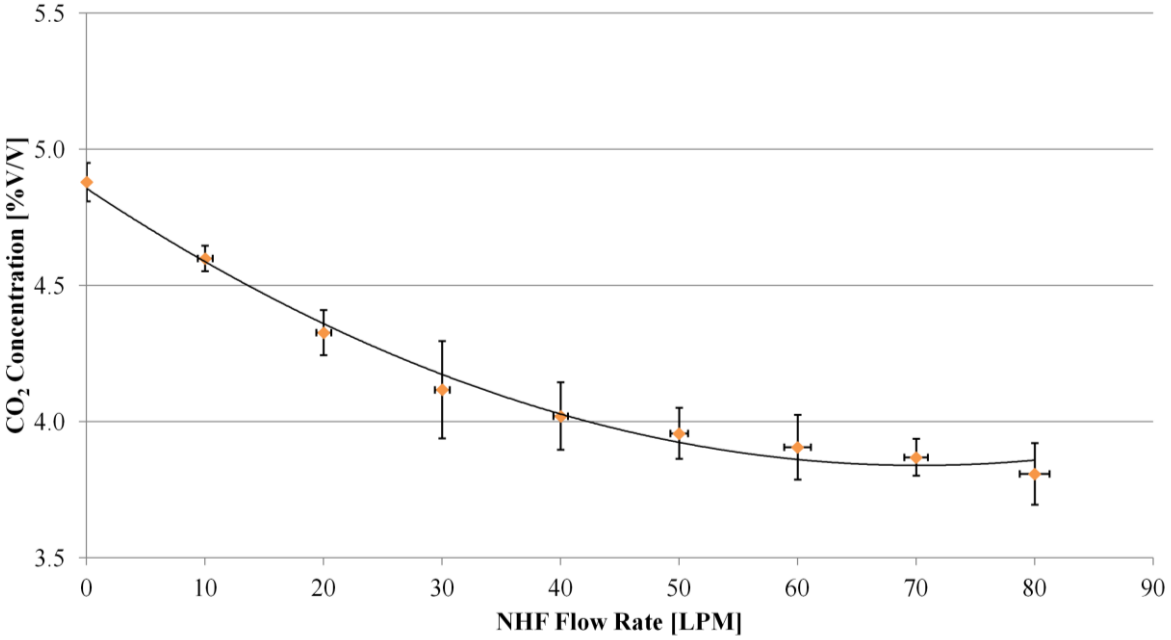

Figure 70: Mean time-averaged CO_2 concentrations observed during natural breathing and breathing with Optiflow™ NHF flow rates from 10 to 80 LPM.

The mean values from the repeated experiments give a time-averaged CO_2 concentration of 4.88 ± 0.07 %V/V during the natural breathing condition. Breathing with only the lowest Optiflow™ NHF therapy level of 10 LPM resulted in a 0.28 %V/V reduction to an average CO_2 concentration of 4.60 ± 0.05 %V/V. When breathing with the highest flow rate of Optiflow™ NHF therapy this level had dropped to a mean CO_2 concentration of 3.81 ± 0.11 %V/V. Optiflow™ NHF therapy flows of 10 to 30 LPM provided significant reductions in the CO_2 concentration, after which the decline began to slow with increasing NHF flow rates. With only 30 LPM NHF therapy there is reduction of 0.76 %V/V in the CO_2 concentration from that observed during natural breathing. By increasing the NHF flow rate to 80 LPM only another 0.31 %V/V reduction is gained, thus the most significant reductions are seen within the first 30 LPM of therapy. This is an interesting result when taking into consideration the static pressure measurements which showed 30 LPM to be the lowest level of Optiflow™ NHF therapy for which the inspiratory resistance of the upper airway was completely compensated for by the NHF flow provided. As increasing the NHF flow rate further induces greater rises in the resistance to expiration while yielding more modest reductions in the concentration of CO_2, it is likely that some NHF flow rate close to 30 LPM would be optimal if this were a live subject.

The repeatability results of the average O_2 concentration show a much greater spread at each breathing condition as shown in Figure 71. As for the average CO_2 concentration plot the horizontal error bars show the level of variation in the NHF flow rate supplied due to instability in the air supply.

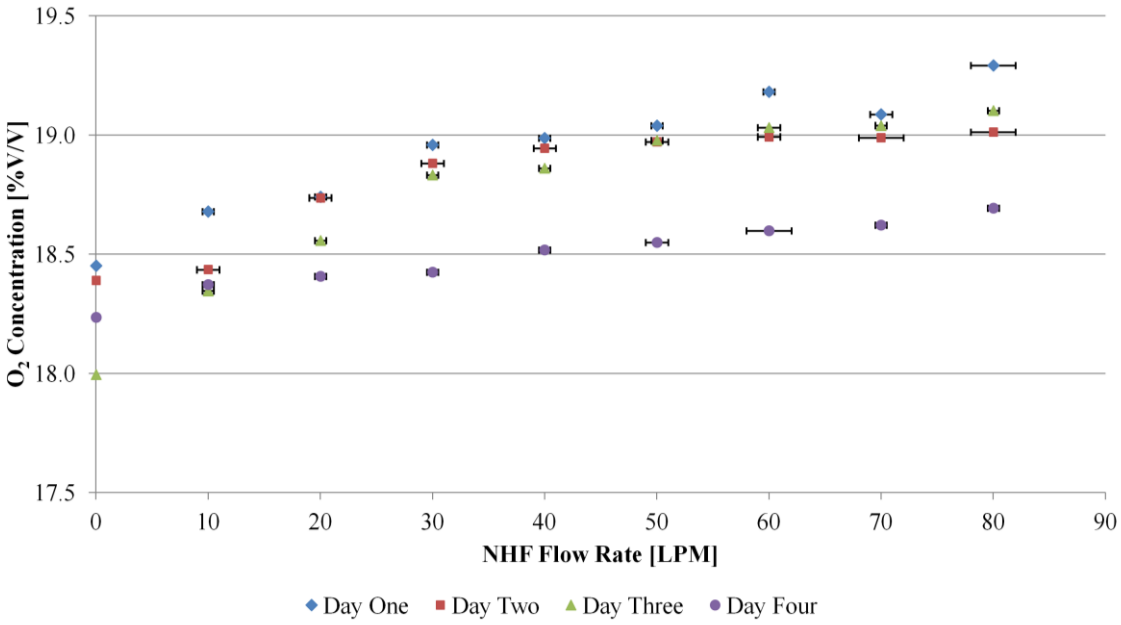

Figure 71: Time-averaged O_2 concentrations during natural breathing and breathing with Optiflow™ NHF flow rates from 10 to 80 LPM showing experimental repeatability over four separate days of testing.

From these repeatability results a mean O_2 concentration was calculated for each breathing condition along with an associated repeatability error once again defined as two times the standard deviation of the results. The mean O_2 concentration curve is given in Figure 72 which shows the results have very low repeatability. As the NHF therapy supplies ambient air, of which 70 %V/V is nitrogen and only 21 %V/V is oxygen, only a fraction of the volume of CO_2 flushed from the airway is replaced with oxygen. Therefore any increase in the magnitude of O_2 concentration observed will only be a fraction of the observed decrease in CO_2 concentration. Because of this, the high variation seen in the O_2 concentration results is even more significant, with some error bars spanning almost the entire range of observed time-averaged O_2 concentrations. As a result of this O_2 concentration results from further experiments were disregarded as unreliable.

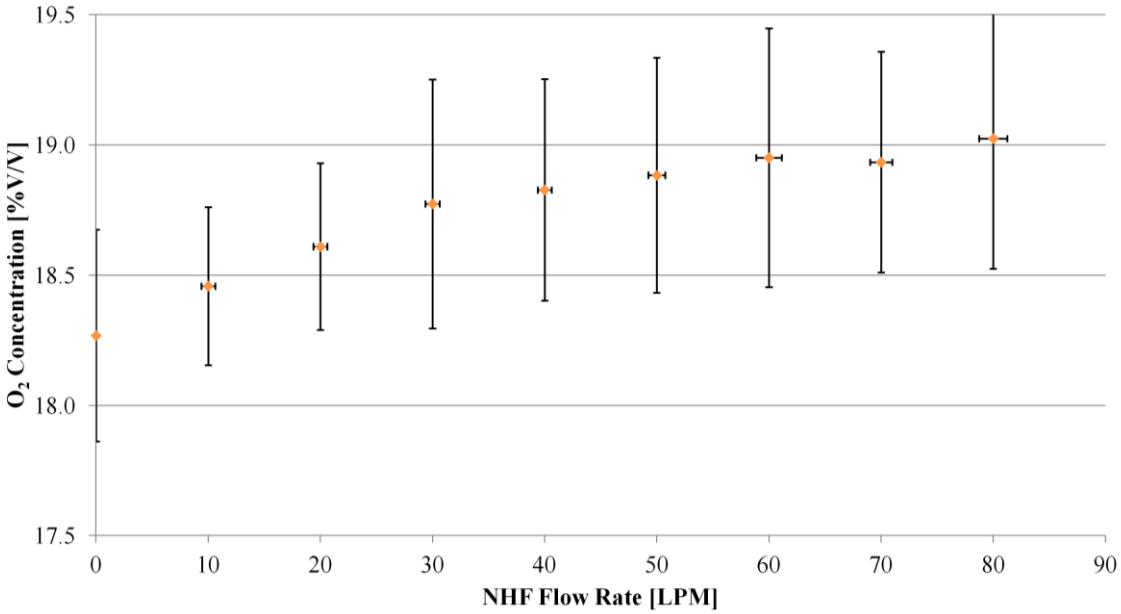

Figure 72: Mean time-averaged O_2 concentrations during natural breathing and breathing with the implementation of various flow rates of Optiflow™ NHF therapy with vertical error bars illustrating low repeatability of results.

The results of these experiments showed that introduction of Optiflow™ NHF therapy results in a significant reduction in the concentration of CO_2 observed. Higher flow rates of NHF therapy produced lower concentrations of CO_2, however the relationship was not linear and the rate of CO_2 reduction decelerates with increasing NHF flow rate. The experiments showed a good level of CO_2 measurement repeatability across the four repetitions with close agreement at natural breathing and differences not exceeding 5% of the lowest measured value. Conversely, O_2 concentration measurement repeatability was found to be very low and as a result further O_2 measurements were disregarded.

9.2.3 Influence of Upper Airway Variation

Experimental Procedure

As the geometry of the human airway is unique for every individual; with variation in airway patency, internal volume and geometrical features; the efficacy of Optiflow™ NHF therapy may depend upon the user. To gain insight into the variation in Optiflow™ NHF therapy efficacy caused by the upper airway anatomic differences between subjects the experiment described in the previous section was carried out using a further four unique upper airway models, giving a total of five airways tested. These upper airway models were the five unique geometries described in Chapter 4. By performing this NHF flow rate experiment on five different airway models the dependence of the average CO_2

concentration on the rate of NHF therapy could be determined for each individual model. Subsequently comparisons of this dependency could be made to gain understanding into how the efficacy of the therapy may vary between subjects.

Each airway model was set up with the experimental respiratory system in the same manner as the standard upper airway model as explained in Chapter 5 and illustrated by Figure 68. A large size Optiflow™ cannula was fitted to each model for all tests requiring Optiflow™ NHF therapy. Images showing the fit of the cannula on airway 16 in comparison to the fit on the standard airway 06B model are provided in Figure 73 from which it is notable that the cannula prongs on the airway 16 model are significantly deformed by the size and shape of the nares. Medium and small cannula were tried on the airway 16 model in an attempt to provide a better fit; however, both were worse fitting than the original large cannula resulting in the final use of the large cannula.

Figure 73: Comparison of large size Optiflow™ cannula fit on airway 06B model (left) and airway 16 model (right) showing ill-fitting nature of cannula on the airway 16 model.

Results and Discussions

A significant level of variation was seen in the average CO_2 concentrations observed during natural breathing across the five airway models. The variation in the CO_2 concentrations observed increased with the introduction of 10 LPM Optiflow™ NHF therapy and continued to increase with increasing NHF flow rates. The results obtained for each unique upper airway model are plotted together in Figure 74, with flow rate errors determined from the reliability of the air supply during each test and concentration errors taken to be equal to that determined from the repeatability experiments performed previously. Concentration error bars have been plotted only on the highest and lowest values to preserve clarity. This plot shows that the variation seen between the different models for the same testing conditions are significantly greater than the repeatability error and can therefore be attributed to airway model differences. Despite the significant differences in the efficacy of the

Optiflow™ NHF therapy observed between the airway models, a significant level of CO_2 washout was achieved for each with increasing levels of therapy providing improved reductions in the average CO_2 concentration.

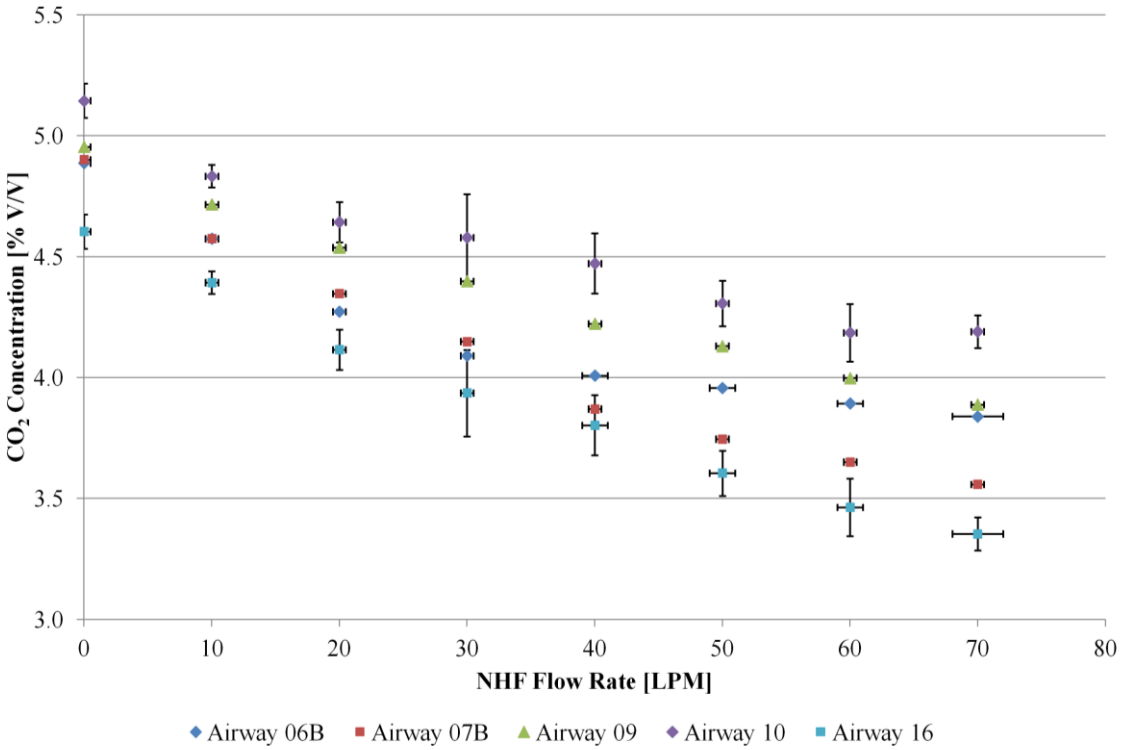

Figure 74: Average CO_2 concentrations during natural breathing and breathing with Optiflow™ NHF therapy flow rates of 10 to 80 LPM for each of the five unique upper airway models showing significant variation.

As variation was seen in the time-averaged CO_2 concentrations and therapy efficacy across the different airway models an investigation of the physical differences was undertaken to determine if the causes of these variations could be simply explained. A number of the physical differences in the airway models were able to be identified and measured by employing the mesh analysis software packages MeshLab and netfabb® Basic. The first of these was the internal upper airway volume. As all other sections of the experimental setup remained constant throughout the tests, the variation in the airway model volumes would cause slight differences in the dead space and overall system volume. The total volume of each airway model was measured by editing each airway mesh in MeshLab such that the trachea exit and the nares were capped to close the internal upper airway volume. The volume of each was then attained using the netfabb Basic analysis tool. The surface area of the internal airway was also extracted from these meshes prior to capping the nares and trachea exit. The results of these measurements are given in Table 7.

Table 7: The internal volumes and surface areas of the five unique upper airway models.

Upper Airway	Airway 06B	Airway 07B	Airway 09	Airway 10	Airway 16
Volume [cm^3]	53.84	60.16	48.27	57.57	43.70
Surface Area [cm^2]	307.91	330.33	281.88	304.70	281.73

Both internal airway volume and surface area were plotted against the average CO_2 concentrations observed during natural breathing and breathing with two representative Optiflow™ NHF therapy flow rates to establish if there were any prevailing relationships. The plot of average CO_2 concentration as a function of upper airway internal volume is given in Figure 75 while Figure 76 gives a plot of the same CO_2 concentrations as a function of the upper airway internal surface area. In both figures the natural breathing data point for each airway is labelled, with all three vertically aligned points belonging to the same airway. In Figure 76 the CO_2 concentrations for airways 16 and 09 fall on almost the same vertical line as the upper airway internal surface areas are very similar, however they are distinguishable as airway 09 has the greater CO_2 concentrations for all three experiment conditions. These two plots show no discernible relationship between the CO_2 concentration and either the upper airway internal volume or surface area. Microsoft Excel was used to fit linear, power and second and third order polynomial curves to the data within each plot and R-squared values were used to determine the accuracy of each fit. No curve fit provided an R-squared value in excess of 0.65; therefore none were considered a true representation of the data.

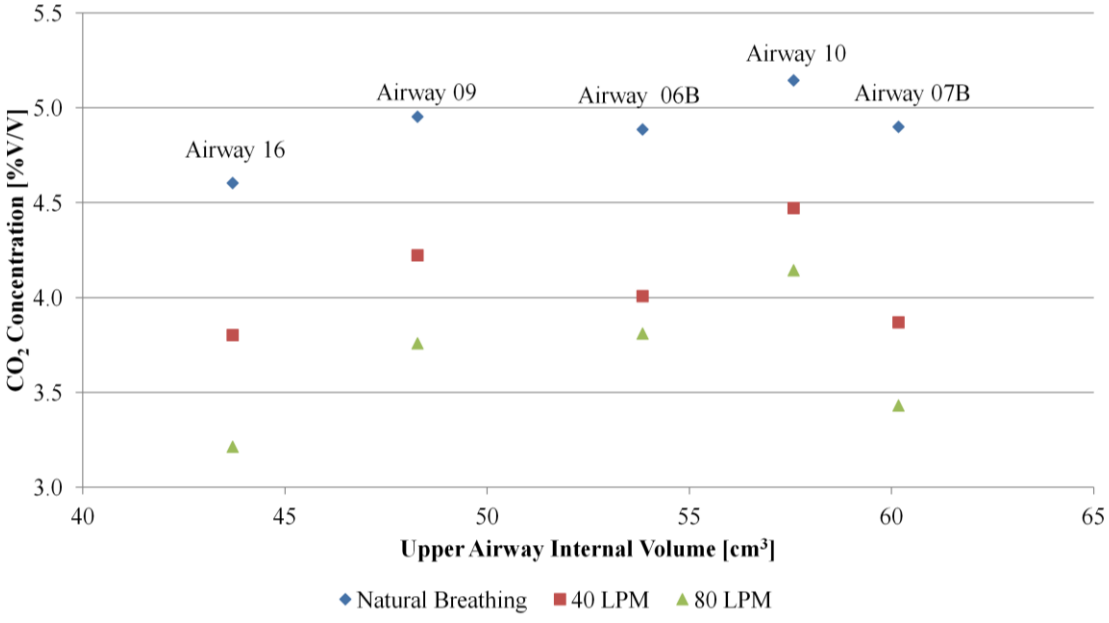

Figure 75: Average CO_2 concentrations observed as a function of the upper airway model internal volumes for natural breathing and two representative flow rates of Optiflow™ NHF therapy.

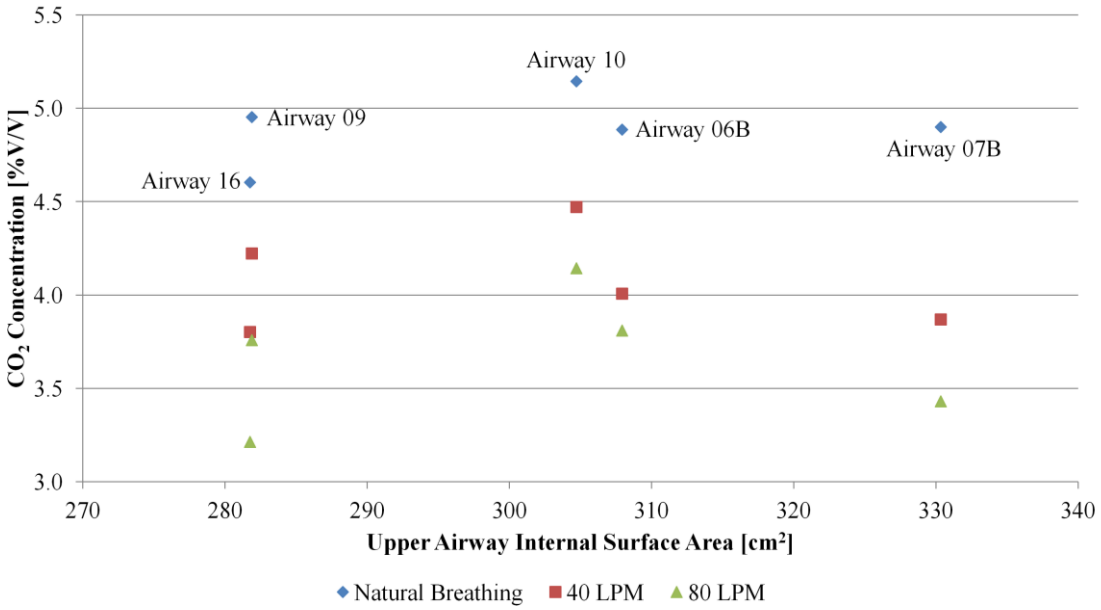

Figure 76: Average CO_2 concentrations as a function of the upper airway model internal surface area for natural breathing and two representative flow rates of Optiflow™ NHF therapy.

As the combined cross-sectional area of the nasal valves is the smallest within the nasal passage they were considered another point of interest and possible contributor to the average CO_2 concentration differences observed across the airway models. These cross sections were subsequently extracted from each airway and measured using netfabb Basic. This was achieved by estimating the central flow path through each nasal valve and inserting a plane normal to the flow path to extract the minimum cross section which could then be measured. It was further decided that the small cross-sections formed at the velopharynx and larynx contractions would similarly be of interest, therefore they were also extracted using the same process. Additionally, the overall maximum cross-sectional area from each airway nasopharynx was also captured and measured and the overall upper airway minimum was extracted from the nasal valve, velopharynx and larynx values. The results of these measurements are provided in Table 8.

Table 8: Measured cross-sectional areas of interest for the five airway models.

Cross-Sectional Area [cm^2]	Airway 06B	Airway 07B	Airway 09	Airway 10	Airway 16
Nasal Valve (Total)	2.22	1.84	1.29	0.98	1.51
Velopharynx	0.91	1.08	0.64	0.94	0.81
Larynx	0.79	0.77	0.71	1.11	0.42
Minimum	0.79	0.77	0.64	0.94	0.81
Maximum	4.30	4.76	4.18	4.57	4.97

A plot of the average CO_2 concentration as a function of cross-sectional area was then created for each of the five measurement sets of Table 8 to determine if any simple relationships could be extracted. These were prepared in the same manner as the volume and surface area measurements with natural breathing and breathing with two representative NHF flow rates of 40 and 80 LPM. The plots for each of these are given in Figure 77 to Figure 81. The results of these plots show that cross-sectional area of the larynx, given in Figure 79, provides the most reasonable linear fit to the CO_2 concentration during natural breathing with an R-squared value of 0.92. The minimum cross-sectional area, shown in Figure 80, also provides a reasonable linear fit of to the natural breathing data with a 0.85 R-squared value. The other three cross-sectional area variables of Table 8 show no close relation to the natural breathing CO_2 concentration observed.

From both the pressure and turbulence intensity measurements, as well as previous CFD investigations, it is known that on expiration the larynx projects a jet into the pharynx. It is perhaps possible that by having a smaller cross-section at the larynx the expiration jet of CO_2 rich air which enters the pharynx has a higher velocity and is subject to less mixing with the ambient air occupying the pharynx volume at the conclusion of inspiration. In this case the expired air exiting the nares would have a higher CO_2 concentration; therefore, for the same CO_2 production rate at the lungs, less CO_2 would reside in the upper airway at the start of the subsequent inspiration. This would lead to an overall lower average CO_2 concentration being observed.

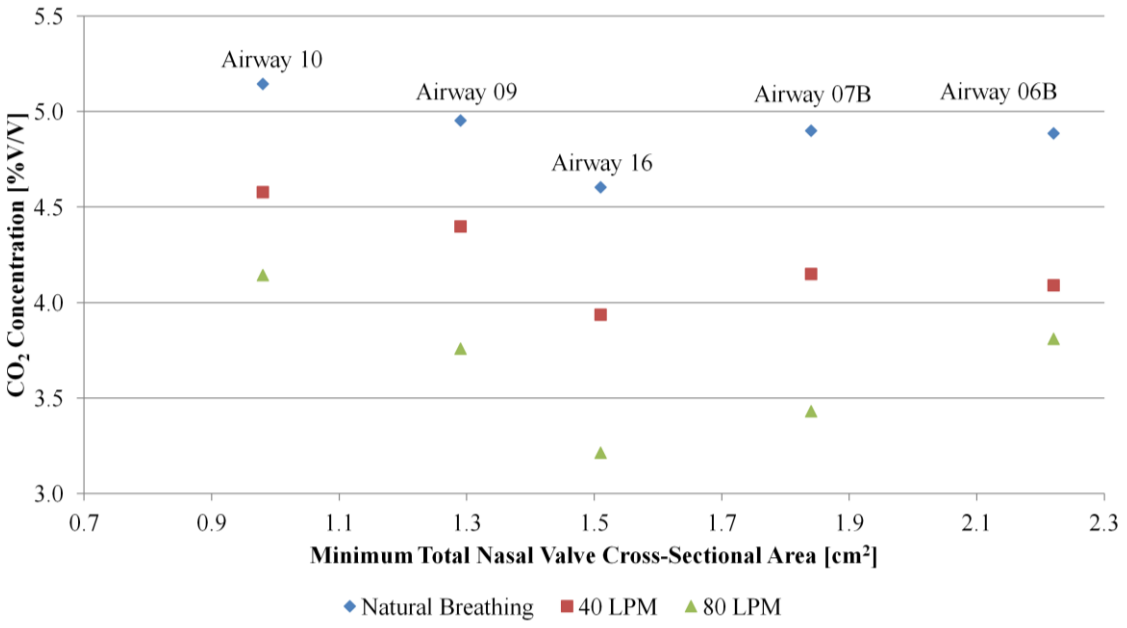

Figure 77: Average CO_2 concentrations as a function of the total minimum cross-sectional area of the nasal valves for natural breathing and breathing with two representative flow rates of Optiflow™ NHF therapy.

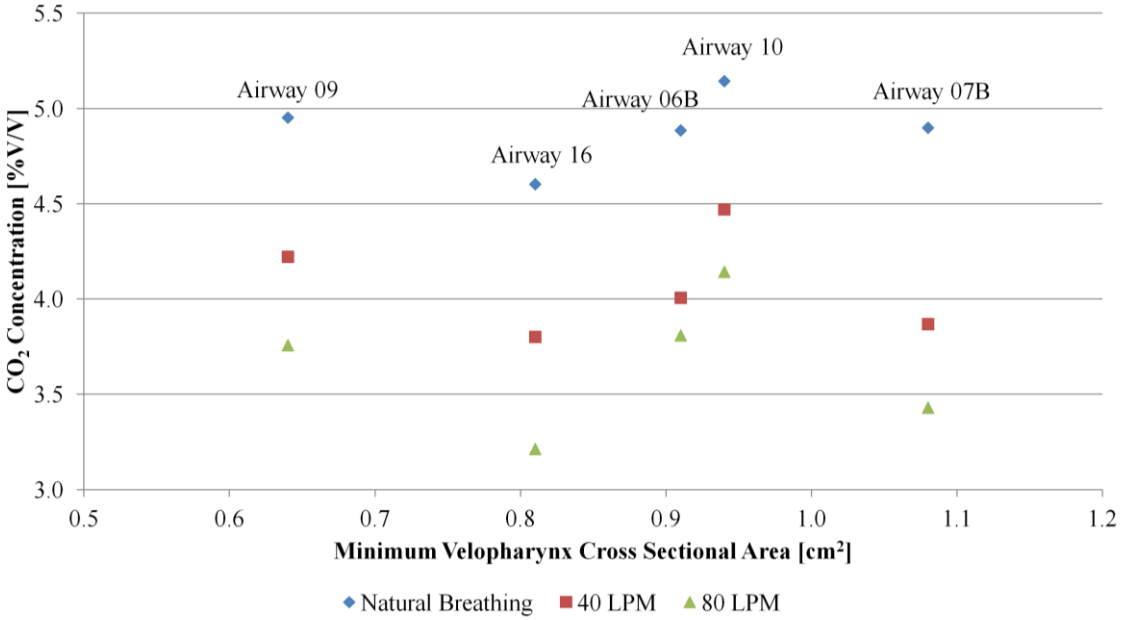

Figure 78: Average CO_2 concentrations as a function of the minimum cross-sectional area of the velopharynx for natural breathing and breathing with two representative flow rates of Optiflow™ NHF therapy.

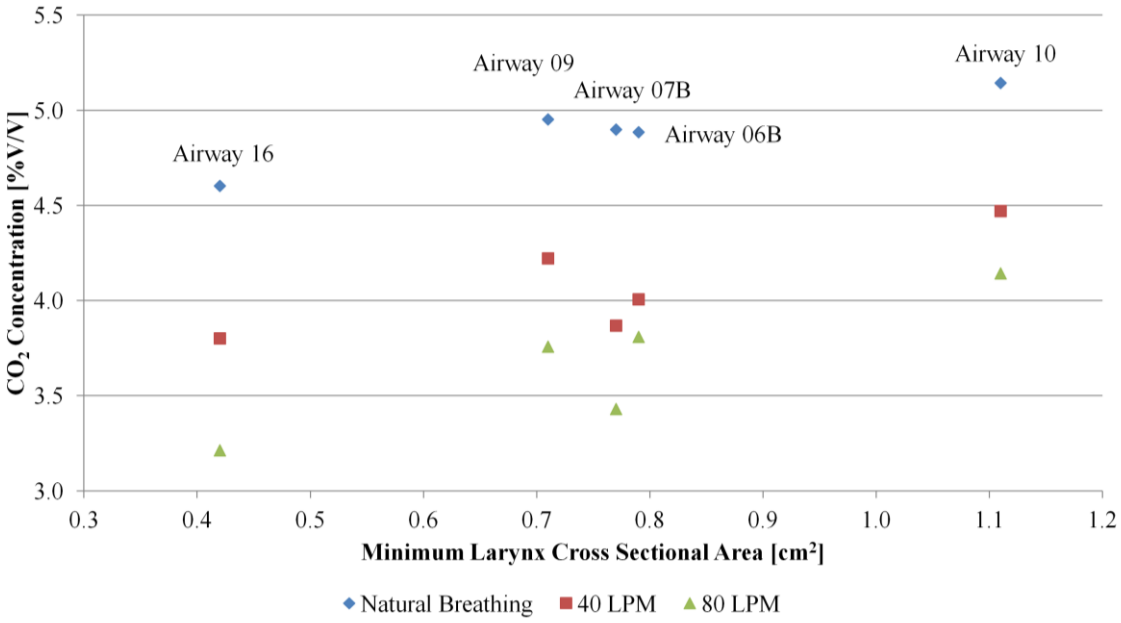

Figure 79: Average CO_2 concentrations observed exterior to the lung pump during natural breathing and breathing with two representative flow rates of Optiflow™ NHF therapy as a function of the minimum cross-sectional area of the larynx.

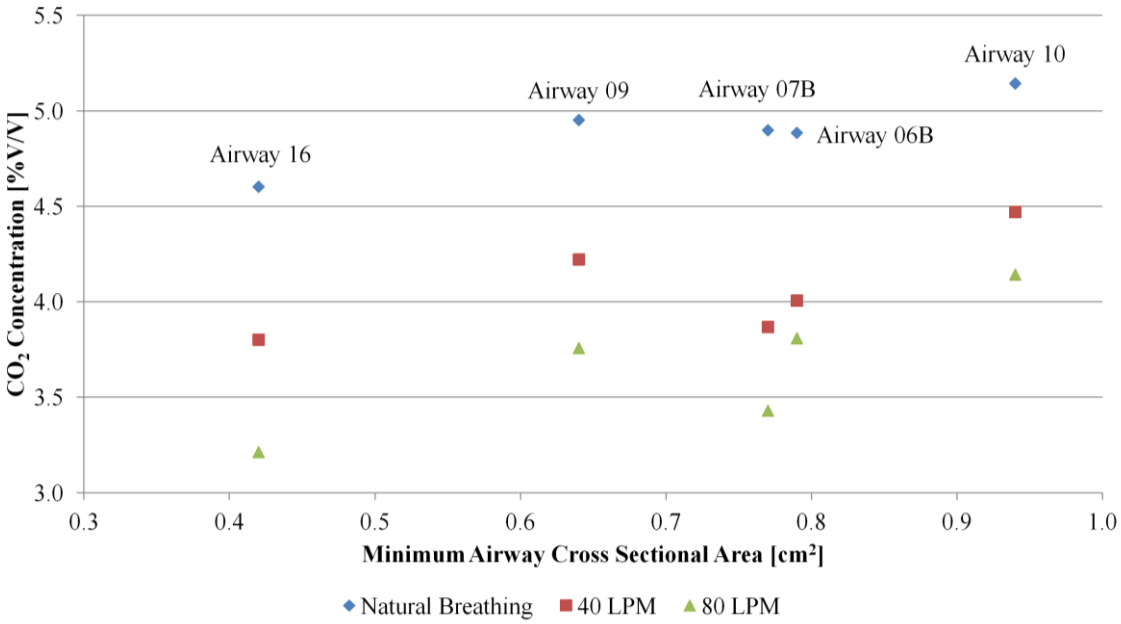

Figure 80: Average CO_2 concentrations as a function of the overall minimum cross-sectional area of the upper airway for natural breathing and breathing with two representative flow rates of Optiflow™ NHF therapy.

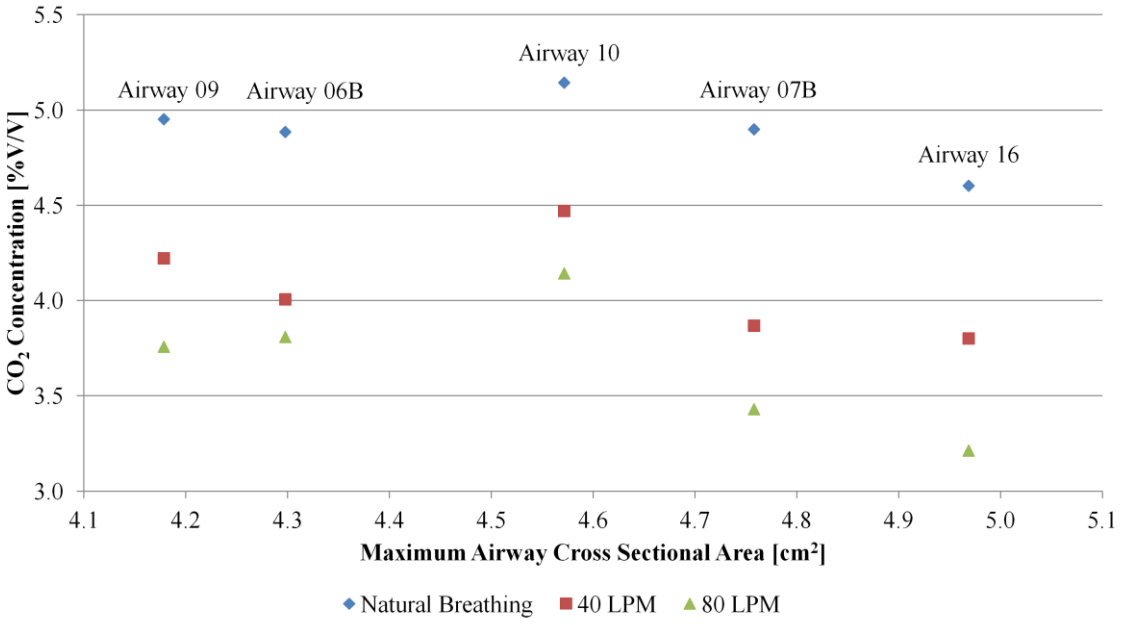

Figure 81: Average CO_2 concentrations as a function of the overall maximum cross-sectional area of the upper airway for natural breathing and breathing with two representative flow rates of Optiflow™ NHF therapy.

Though a reasonable relationship is seen between the larynx cross-sectional area and the average CO_2 concentration during natural breathing, this does not extend to the concentrations observed when Optiflow™ NHF therapy was in use. With increasing NHF flow rates the linear fit becomes increasingly less accurate with the worst fit occurring at 40 LPM, after which point the fit improves again to a maximum R-squared value of 0.81. This is also the case for all of the other four plots derived from the Table 8 measurements with Optiflow™ NHF therapy results producing worse fits than natural breathing. This implies that though there may be a simple geometrical feature which governs the average CO_2 concentration during natural breathing, the introduction of NHF therapy disturbs this relation.

The geometrical form of the upper airway is unique to each airway model and has a high level of complexity. As the differences seen in the CO_2 concentration measurements can only be attributed to the variation in the airway models it was thought that a relationship may be found from a characteristic length. This was defined as the ratio of airway volume to surface area, against which the CO_2 concentrations were plotted in Figure 82. Setting a linear fit to the natural breathing data provided a reasonable fit with a 0.84 R-squared value. This is not as strong as the fit found when plotting the CO_2 concentrations against the minimum cross-sectional areas at the larynx and only slightly worse than the linear fit for upper airway minimum cross-sectional area. However, when compared to the fits created when plotting the CO_2 concentrations against the upper airway volumes or surface areas alone, this fit which combines both factors is significantly more accurate.

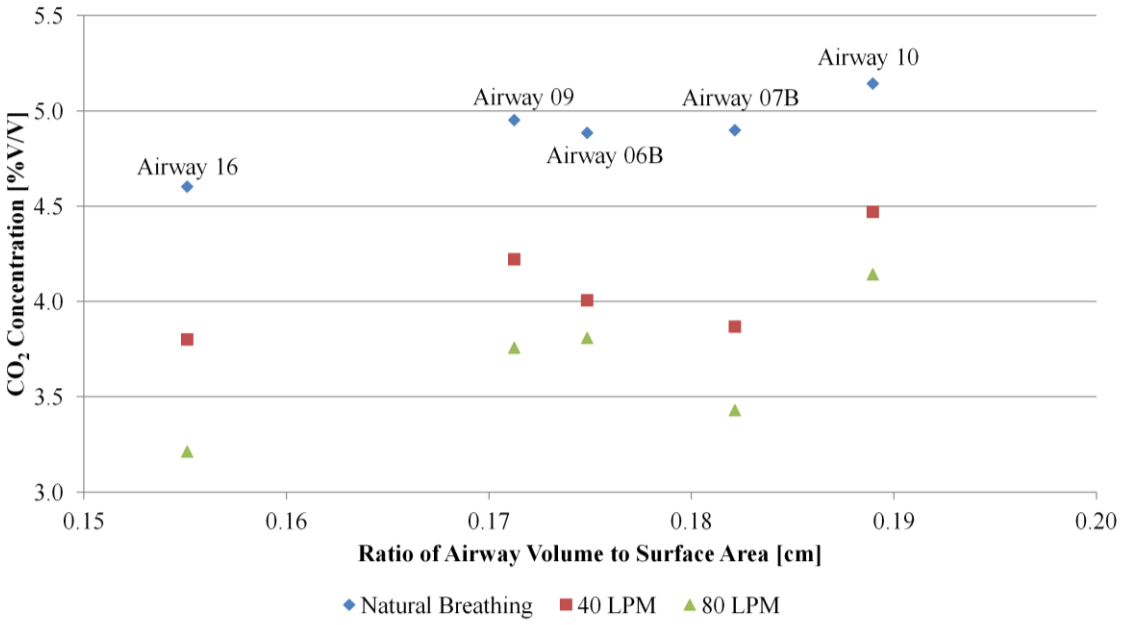

Figure 82: Average CO_2 concentrations as a function of the ratio of upper airway volume to surface area for natural breathing and breathing with two representative flow rates of Optiflow™ NHF therapy.

Another measure was developed in an attempt to define the uniformity and patency of each upper airway by using the ratio of minimum to maximum cross-sectional areas. The average CO_2 concentrations were then once again plotted against this ratio to determine if a relationship could be drawn between them. Figure 83 shows this plot that, for natural breathing, provides a reasonable linear relationship to the CO_2 concentration with an R-squared value of 0.85. This fit is therefore no better than that determined from the larynx cross-sectional area data and is in fact as good as the fit provided when plotting the CO_2 concentration against the minimum upper airway cross-sectional area alone. As for all previous plots of CO_2 concentration as a function of airway model measurements it was found that with the introduction of Optiflow™ NHF therapy the linear fit became less suitable.

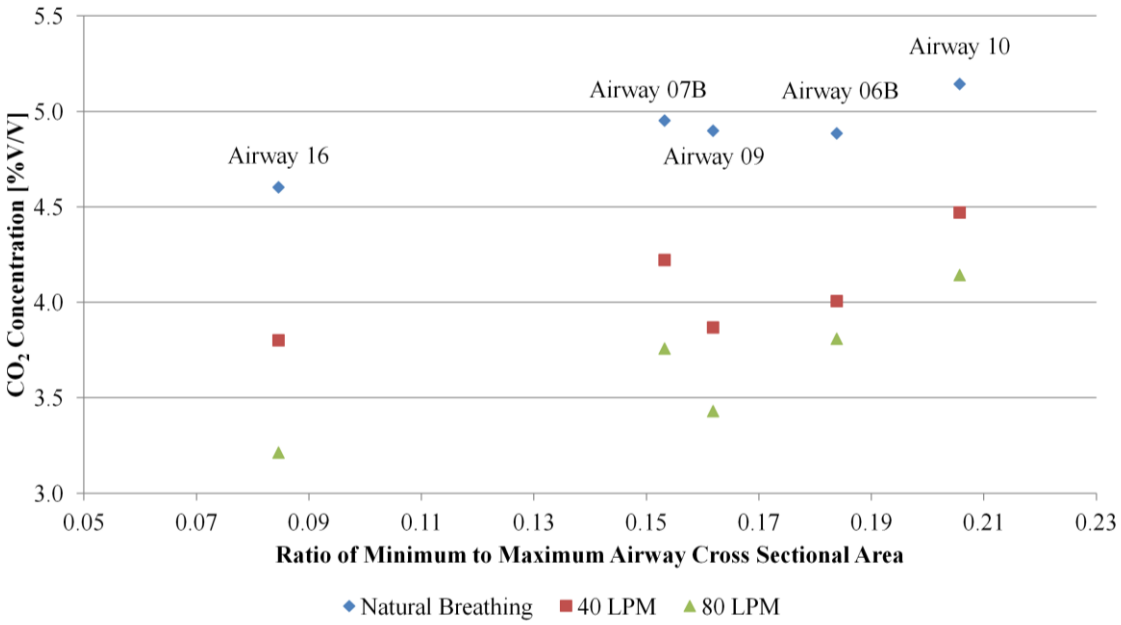

Figure 83: Average CO_2 concentrations as a function of the ratio of minimum to maximum upper airway cross-sectional areas for natural breathing and breathing with two representative flow rates of Optiflow™ NHF therapy.

By plotting the CO_2 concentration as a function of easily identifiable large-scale and local upper airway measurements some possible relationships have been uncovered for the case of natural breathing. The minimum cross-sectional area of the larynx provides the strongest linear fit to the data, while the overall minimum cross-sectional area of the upper airway and also the ratio of upper airway volume to surface area both provide reasonable linear trends. The upper airway volume to surface area is in particular of interest as the individual volume and surface area measurements showed no prevailing relation to the CO_2 concentration results until combined. Due to the small sample size it is not possible to be certain of these relationships without experimenting further with new airway geometries.

As a final investigation each airway was visually inspected in netfabb® Basic for any obvious geometrical differences which may explain the differences seen in the CO_2 concentrations. Initially airways were examined and compared as a whole to little effect. Subsequently the nasal cavities of each airway were broken down into sections perpendicular to the approximate central flow path to observe and compare the complexity of the meatuses. Figure 84 provides the three central nasal cavity cross sections taken from each airway with the positioning of the cutting planes illustrated in the left hand images of the airways. Though the airways presented many geometrical differences, as demonstrated by Figure 84, no pattern of differences which would explain the differences in CO_2 concentration could be elucidated.

This set of experiments determined that the individuality of the upper airway has a significant effect on the average concentration of CO_2 seen during both natural breathing and breathing with Optiflow™ NHF therapy when all other experimental parameters are kept constant. Some relationships were found between the average CO_2 concentration observed during natural breathing and the minimum cross-sectional area of the larynx, the overall minimum upper airway cross-sectional area and finally the ratio of upper airway volume to surface area. A greater number of unique airway geometries are necessary to determine the strength of these relationships. These trends did not extend to the cases in which Optiflow™ NHF therapy was in use. This combined with the impracticality of performing the same measurements on live patients receiving Optiflow™ NHF therapy means that there is limited use for this information for the cannula product design process or development of clinical protocol. The findings are however relevant as they show the use of Optiflow™ NHF therapy induces a reduction in the average CO_2 concentration observed during natural breathing for all upper airway geometries.

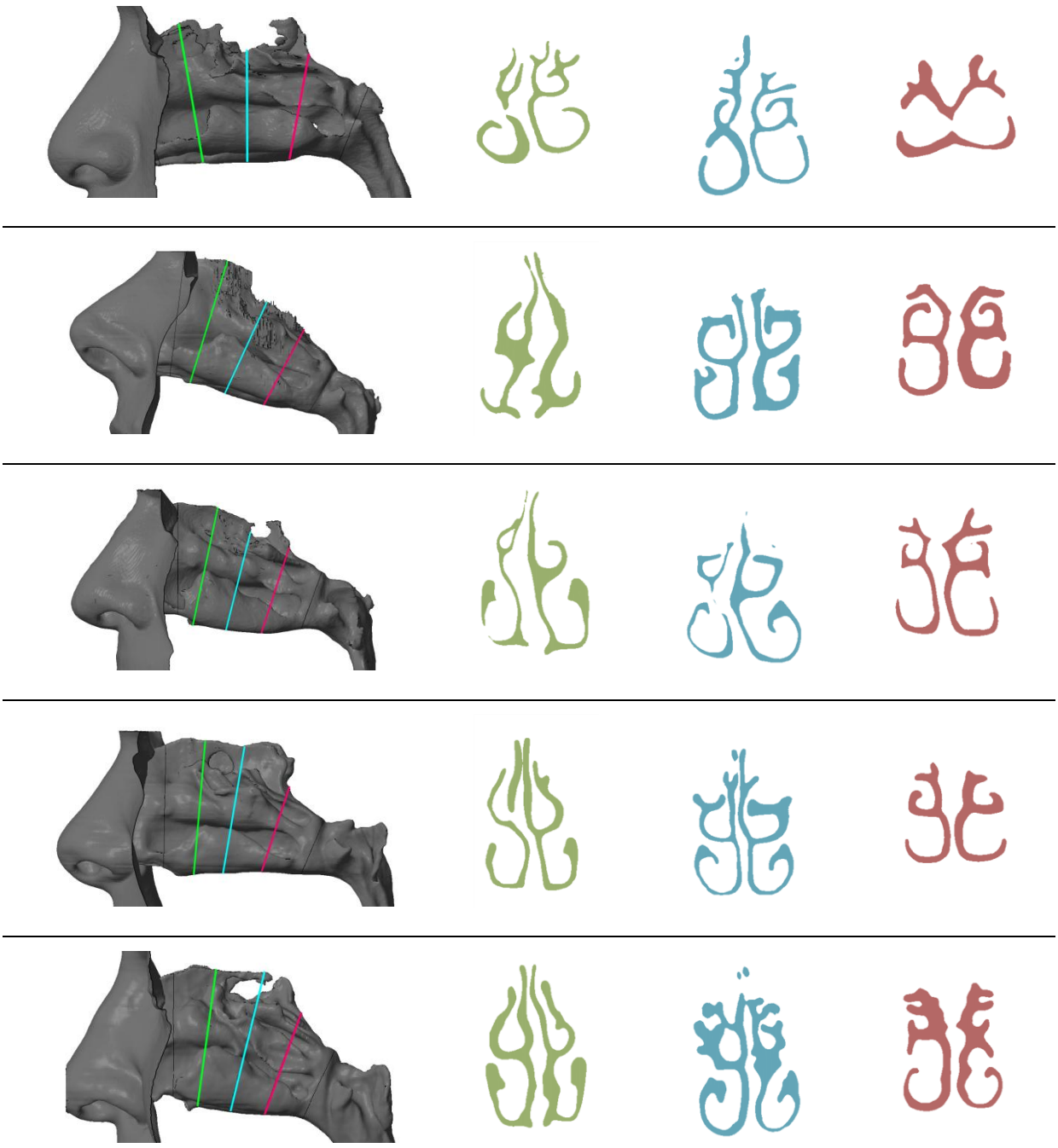

Figure 84: Nasal cavity cross sections of airways 06B, 07B, 09, 10 and 16 in order from top to bottom. The left hand column shows a side view of each airway with analogous cutting planes marked by green, blue and magenta lines with corresponding sections shown to the right. Sections are not to scale.

9.3 Conclusions

CO_2 washout of the anatomic dead space with the use of Optiflow™ NHF therapy was investigated with the use of two experimental methods. The first, Experimental Method Version One, found that an initial concentration of CO_2 introduced to the lung pump decayed to a reference value of 600 ppm for a fewer number of breath cycles when breathing with 30 LPM NHF flow in comparison to decay during natural breathing. However due to low repeatability of the experiments this method was abandoned.

Experimental Method Version Two was designed to replicate the physiological process of continuous CO_2 diffusion into the lungs during breathing with CO_2 measurement just exterior to the lung volume. With this method time-averaged CO_2 concentrations were able to be determined so that the efficacy of Optiflow™ NHF therapy could be assessed for a number of different airway geometries. At natural breathing a mean time-averaged CO_2 concentration of 4.88 ± 0.07 %V/V was determined over four experimental repetitions. Implementation of Optiflow™ NHF therapy was found to provide a significant reduction of 0.25 %V/V in the time-averaged CO_2 concentration at the lowest flow rate of 10 LPM in comparison to natural breathing. With increasing NHF flow rates CO_2 washout continued to increase, however only modest reductions in time-averaged CO_2 concentration were seen at the upper flow rates tested with a minimum of 3.81 ± 0.11 % V/V observed at 80 LPM. The average CO_2 concentration observed during natural breathing was found to vary significantly across five unique airway models examined as did the efficacy of Optiflow™ NHF therapy at flow rates of 10 to 80 LPM. As all other experimental parameters remained constant this was a result of anatomic differences alone and investigation found a reasonable relationship between natural breathing CO_2 concentration and the minimum larynx CSA. This relation did not however translate to the differences seen during NHF therapy. Though differences in therapy efficacy were seen across the five upper airway models, Optiflow™ NHF therapy provided significant CO_2 washout for all.

10 Conclusions and Future Work

Static pressure measurements at multiple positions within the upper airway 06B model during natural breathing flows revealed the transient nature of the pressure wave had a form similar to and in phase with the breathing flow wave. In general the peak inspiratory and expiratory static pressures were seen to increase in magnitude as the measurement position neared the trachea. Pressure measurements at the nasopharynx suggested that the nasal passage resistance was equal for both flow directions. At the most inferior measurement positions at the entrance to the trachea the pressures indicated greater upper airway flow resistance for inspiration. With the use of NHF therapy mean and peak static pressures were seen to increase with increasing NHF flow rates at all measurement positions. A mean static gauge pressure of 300 Pa was observed at the superior trachea when breathing with 70 LPM NHF therapy, the maximum NHF flow rate employed. At the same measurement position the peak inspiratory pressure first assumed a positive value for a NHF flow rate of 30 LPM inferring that for this flow rate the work required to overcome the upper airway flow resistance was fulfilled by the NHF therapy. It was demonstrated that the transient static pressure profile at any flow rate of NHF therapy between 10 and 70 LPM could be reasonably well approximated as a function of the NHF flow rate and the natural breathing profile observed at the same measurement position. It was determined that the beneficial increases in inspiratory pressure and thus reductions in inspiratory work were accompanied by greater increases in expiratory pressures and work. It is subsequently thought likely that above some flow rate, dependant on the individual user, the detrimental pressure effects during expiration will outweigh the beneficial.Hot wire anemometry was employed to investigate the turbulence intensities of natural breathing flows passing through the centre of the left and right nares of two in vivo subjects and five in vitro airway models. Turbulence intensities measured in vivo and in vitro were similarly small during peak inspiration (~ 2 %) whilst peak expiration produced a large range from low (5 %) to high (46 %). Mean peak velocities observed at the nares also showed a larger range during expiration, with maximum in vitro values of 3.47 m/s and 2.50 m/s seen for expiration and inspiration respectively. Hot wire anemometry was further utilised to map the velocity and turbulence intensity profiles along an anterior to posterior traverse of the velopharynx of airway 06B during natural breathing flows. Peak expiration and inspiration velocity profiles showed mean velocities increasing toward the posterior, with maximum values of 3.82 and 3.02 m/s seen respectively. Peak inspiration turbulence intensities were relatively uniform and low along the traverse; however, peak expiration turbulence intensities rose to a high maximum of 55% near the anterior wall and subsequently declined in the posterior direction. The introduction of NHF therapy did not greatly affect the mean peak velocity profiles along the traverse, causing small changes to the peak expiration and inspiration maximums. NHF therapy also had little influence on the form of the turbulence intensity traverse profiles yet did produce a triple fold increase in the average turbulence

intensity across the centre of the velopharynx during peak inspiration. The minimal increases to the turbulence intensities during peak expiration from the use of NHF implied minor contribution to the mechanism of CO_2 washout; however as only a single traverse was examined it is possible that in other regions the introduction of NHF therapy has a greater influence on turbulence intensity which does contribute to the washout effect.

Two experimental methods were developed to investigate CO_2 washout effects, the first mechanism of action proposed by Dysart et al. (2009) for the efficacy of NHF therapy. The first Experimental Method Version One took a non-physiologic approach, determining that the use of NHF therapy during breathing increased the rate of CO_2 decay within the experimental model; however results lacked repeatability and this method was subsequently abandoned. Experimental Method Version Two employed a more realistic system with volumes to match an average adult respiratory system and a continuous flow of CO_2 into the lung pump replicating the physiological process of CO_2 diffusion into the lungs. Measurements of CO_2 were taken just exterior to the lung volume, within the conducting airways, over many realistic breath cycles from which a time-averaged CO_2 concentration was determined for each experiment. During natural breathing an average CO_2 concentration of 4.88 ± 0.07 %V/V was observed, with introduction of the lowest NHF flow rate at 10 LPM resulting in a reduction of 0.25 %V/V. At the highest tested NHF flow rate of 80 LPM the time-averaged CO_2 concentration had further declined to 3.81 ± 0.11 %V/V. The greatest reductions in concentration occurred within the first 30 LPM of NHF therapy, accounting for a 0.76 %V/V decrease from natural breathing, an interesting detail when taken into account with the transient pressure results which determined upper airway resistance to be overcome by 30 LPM NHF therapy. The time-averaged CO_2 concentrations observed during natural breathing and breathing with NHF therapy were found to have significant variation across five unique airway geometries tested. A reasonable linear relation was found between the airways' minimum larynx cross-sectional areas and the natural breathing average CO_2 concentrations; however this relation did not extend to CO_2 concentrations observed during experiments with NHF therapy.

10.1 Future Work

Though this research has provided much new evidence to support the theories of positive airway pressure generation and CO_2 washout of the upper airway during the use of Optiflow™ NHF therapy there is still scope for further investigations. It is suggested that the following work may be beneficial in furthering the research presented in this thesis to gain greater understanding of the mechanisms by which Optiflow™ NHF therapy provides respiratory support.

The transient pressure effects observed within the rigid airway model infer the generation of significant positive airway pressure with the use of NHF therapy; however the true in vivo pressure effects may vary significantly due to the compliance of the upper airway. By repeating the transient pressure experiments in a compliant model the influence of airway distensibility on the pressures achieved could be determined. As airway compliance is heterogeneous and complex a partially rigid model which replicates the compliance of the velopharynx, as achieved during the steady-state research of Cressy et al. (2011), may be useful in initial investigations, followed by replication of the compliant nasal vestibule.

Use of multiple unique airway models during CO_2 washout measurements revealed a dependence of the average natural breathing CO_2 concentration and NHF washout efficacy on the upper airway geometry employed. For the case of natural breathing a tentative linear relation was found between the average CO_2 concentration and the minimum larynx cross-sectional area, whilst no strong relation could be found for the average CO_2 concentrations observed during NHF therapy. Further testing of CO_2 washout within a greater number of unique airway models is suggested to provide greater population coverage, to determine the validity of the natural breathing relations proposed in this research and perhaps to find new relations to explain the differences in NHF therapy efficacy.

Though this research has pioneered the measurement of CO_2 washout effects, much more could be learnt by capturing the time-dependant CO_2 concentration over a breath cycle with the use of a faster gas sensor. This would allow for more efficient experiments from which flow-averaged concentrations could be found. Concentration measurements within specific airway regions could then be performed from which the percentage washout of the upper airway and subsequently the effective reduction in dead space volume could be approximated.

The five airway models employed in the current research all simulated a nasal-breathing flow path with the mouth closed as this is the mode of breathing recommended by FPH during the use of Optiflow™ NHF therapy. It is proposed that a mouth-open breathing mode during NHF therapy may actually increase the level of washout achieved as NHF flow administered by the nasal cannula would continuously flush the nasal cavity, nasopharynx, oropharynx and oral cavity, theoretically removing their entire volume from the anatomic dead space. Examination of this theory is suggested by performing CO_2 washout experiments with a mouth-open upper airway model.

From the pressure and CO_2 washout results determined in this research the use of a NHF flow rate of 30 LPM seems to provide an optimum positive airway pressure for mitigating the upper airway inspiratory resistance whilst also providing a large percentage of the attainable CO_2 washout within the range of flow rates tested. Because of this it is suggested that a flow rate of 30 LPM may provide optimum respiratory support, particularly on account of the tradeoffs between the beneficial inspiratory and detrimental expiratory work effects caused by NHF therapy PAP generation. This

could be further investigated by in vivo examinations of the influence of different NHF therapy flow rates.

References

AKKERMANS, L. M. A. 1991. Esophageal manometry. *Digestive Diseases and Sciences,* 36**,** 14S-16S.

BARANIUK, J. N. & KIM, D. 2007. Nasonasal reflexes, the nasal cycle, and sneeze. *Current Allergy and Asthma Reports,* 7**,** 105-111.

BRÄUNLICH, J., BEYER, D., MAI, D., HAMMERSCHMIDT, S., SEYFARTH, H. J. & WIRTZ, H. 2013. Effects of Nasal High Flow on Ventilation in Volunteers, COPD and Idiopathic Pulmonary Fibrosis Patients. *Respiration,* 85**,** 319-325.

CAMPBELL, D. M., SHAH, P. S., SHAH, V. & KELLY, E. N. 2006. Nasal continuous positive airway pressure from high flow cannula versus Infant Flow for preterm infants. *Journal of Perinatology,* 26**,** 546-549.

CHATILA, W., NUGENT, T., VANCE, G., GAUGHAN, J. & CRINER, G. J. 2004. The effects of high-flow vs low-flow oxygen on exercise in advanced obstructive airways disease. *Chest,* 126**,** 1108-1115.

CHUNG, S.-K. & KIM, S. K. 2008. Digital particle image velocimetry studies of nasal airflow. *Respiratory Physiology & Neurobiology,* 163**,** 111-120.

CHURCHILL, S. E., SHACKELFORD, L. L., GEORGI, J. N. & BLACK, M. T. 2004. Morphological variation and airflow dynamics in the human nose. *American Journal of Human Biology,* 16**,** 625-638.

CRESSY, O., DEY, K., MACDONALD, S. & WINN, O. 2011. Airway Resistance: Investigation of the relationship between patient-specific external geometry and airway pressure loss. University of Canterbury, Christchurch.

CROCE, C., LOUIS, B., FODIL, R., DURAND, M., SBIRLEA-APIOU, G., CAILLIBOTTE, G., PAPON, J.-F., BLONDEAU, J.-R., COSTE, A. & ISABEY, D. 2006. In vitro experiments and numerical simulations of airflow in realistic nasal airway geometry. *Annals of Biomedical Engineering,* 34**,** 997-1007.

DE KLERK, A. 2008. Humidified high-flow nasal cannula: Is it the new and improved CPAP? *Advances in Neonatal Care,* 8**,** 98-106.

DOORLY, D., TAYLOR, D. J., FRANKE, P. & SCHROTER, R. C. 2008a. Experimental investigation of nasal airflow. *Proceedings of the Institution of Mechanical Engineers, Part H: Journal of Engineering in Medicine.* England.

DOORLY, D. J., TAYLOR, D. J. & SCHROTER, R. C. 2008b. Mechanics of airflow in the human nasal airways. *Respiratory Physiology & Neurobiology,* 163**,** 100-110.

DYSART, K., MILLER, T. L., WOLFSON, M. R. & SHAFFER, T. H. 2009. Research in high flow therapy: Mechanisms of action. *Respiratory Medicine,* 103**,** 1400-1405.

ELAD, D., WOLF, M. & KECK, T. 2008. Air-conditioning in the human nasal cavity. *Respiratory Physiology & Neurobiology,* 163**,** 121-127.

GAMBARUTO, A. M., TAYLOR, D. J. & DOORLY, D. J. 2009. Modelling nasal airflow using a Fourier descriptor representation of geometry. *International Journal for Numerical Methods in Fluids,* 59**,** 1259-1283.

GRGIC, B., FINLAY, W. H. & HEENAN, A. F. 2004. Regional aerosol deposition and flow measurements in an idealized mouth and throat. *Journal of Aerosol Science,* 35**,** 21-32.

GROVES, N. & TOBIN, A. 2007. High flow nasal oxygen generates positive airway pressure in adult volunteers. *Australian Critical Care,* 20**,** 126-131.

HAHN, I., SCHERER, P. W. & MOZELL, M. M. 1993. Velocity profiles measured for airflow through a large-scale model of the human nasal cavity. *Journal Applied Physiology,* 75**,** 2273-2287.

HASEGAWA, M. & KERN, E. B. 1978. Variations in nasal resistance in man: a rhinomanometric study of the nasal cycle in 50 human subjects. *Rhinology,* 16**,** 19-29.

HÄUßERMANN, S., BAILEY, A. G., BAILEY, M. R., ETHERINGTON, G. & YOUNGMAN, M. 2002. The influence of breathing patterns on particle deposition in a nasal replicate cast. *Journal of Aerosol Science,* 33**,** 923-933.

HOPKINS, L. M., KELLY, J. T., WEXLER, A. S. & PRASAD, A. K. 2000. Particle image velocimetry measurements in complex geometries. *Experiments in Fluids,* 29**,** 91-95.

HÖRSCHLER, I., BRÜCKER, C., SCHRÖDER, W. & MEINKE, M. 2006. Investigation of the impact of the geometry on the nose flow. *European Journal of Mechanics - B/Fluids,* 25**,** 471-490.

ISHIKAWA, S., NAKAYAMA T FAU - WATANABE, M., WATANABE M FAU - MATSUZAWA, T. & MATSUZAWA, T. 2006. Visualization of flow resistance in physiological nasal respiration: Analysis of velocity and vorticities using numerical simulation. *Arch Otolaryngol Head Neck Surg,* 132**,** 1203-1209.

JANSSENS, H. M., DE JONGSTE, J. C., FOKKENS, W. J., ROBBEN, S. G., WOUTERS, K. & TIDDENS, H. A. 2001. The Sophia Anatomical Infant Nose-Throat (Saint) model: A valuable tool to study aerosol deposition in infants. *Journal of Aerosol Medicine,* 14**,** 433-441.

JEONG, S.-J., KIM, W.-S. & SUNG, S.-J. 2007. Numerical investigation on the flow characteristics and aerodynamic force of the upper airway of patient with obstructive sleep apnea using computational fluid dynamics. *Medical Engineering & Physics,* 29**,** 637-651.

JONES, N. 2001. The nose and paranasal sinuses physiology and anatomy. *Advanced Drug Delivery Reviews,* 51**,** 5-19.

KELLY, J. T., PRASAD, A. K. & WEXLER, A. S. 2000. Detailed flow patterns in the nasal cavity. *Journal of Applied Physiology,* 89**,** 323-337.

KIM, S. K. & CHUNG, S. K. 2004. An investigation on airflow in disordered nasal cavity and its corrected models by tomographic PIV. *Measurement Science and Technology,* 15**,** 1090-1096.

KIM, S. K. & HAW, J. R. 2004. An investigation on airflow in pathological nasal airway by PIV. *Journal of Visualization,* 7**,** 341-348.

KOOK KIM, J., YOON, J.-H., HOON KIM, C., WOOK NAM, T., BO SHIM, D. & AE SHIN, H. 2006. Particle image velocimetry measurements for the study of nasal airflow. *Acta Oto-Laryngologica,* 126**,** 282-282.

KUBICKA, Z. J., LIMAURO, J. & DARNALL, R. A. 2008. Heated, humidified high-flow nasal cannula therapy: yet another way to deliver continuous positive airway pressure? *Pediatrics,* 121**,** 82-88.

LUMB, A. B. 2010. *Nunn's Applied Respiratory Physiology,* Elsevier Ltd.

MCCAFFREY, T. V. & KERN, E. B. 1979. Clinical evaluation of nasal obstruction. *Arch Otolaryngol,* 105**,** 542-545.

MCKIERNAN, C., CHUA, L. C., VISINTAINER, P. F. & ALLEN, H. 2010. High Flow Nasal Cannulae Therapy in Infants with Bronchiolitis. *The Journal of Pediatrics,* 156**,** 634-638.

MILÉSI, C., BALEINE, J., MATECKI, S., DURAND, S., COMBES, C., NOVAIS, A. R. B., CAMBONIE, G. & COMBONIE, G. 2013. Is treatment with a high flow nasal cannula effective in acute viral bronchiolitis? A physiologic study. *Intensive Care Medicine,* 39**,** 1088-1094.

MOINUDDIN, R., MAMIKOGLU, B., BARKATULLAH, S. & COREY, J. P. 2001. Detection of the nasal cycle. *American Journal of Rhinology,* 15**,** 35-35.

MÜLLER-WITTIG, W., MLYNSJI G FAU - WEINHOLD, I., WEINHOLD I FAU - BOCKHOLT, U., BOCKHOLT U FAU - VOSS, G. & VOSS, G. 2002. Nasal airflow diagnosis - Comparison of experimental studies and computer simulations. *Medicine meets virtual reality 02/10 series : Studies in health technology and informatics.*

MÜLLER, K. M., BUSSE, H. & OSMERS, F. 1978. Anatomy of the naso-lacrimal duct in new-borns: Therapeutic considerations. *European Journal of Pediatrics,* 129**,** 83-92.

MYLAVARAPU, G., MURUGAPPAN, S., MIHAESCU, M., KALRA, M., KHOSLA, S. & GUTMARK, E. 2009. Validation of computational fluid dynamics methodology used for human upper airway flow simulations. *Journal of Biomechanics,* 42**,** 1553-1559.

NAFTALI, S., SCHROTER, R. C., SHINER, R. J. & ELAD, D. 1998. Transport phenomena in the human nasal cavity: a computational model. *Annals of Biomedical Engineering,* 26**,** 831-839.

NAITO, K., IWATA S FAU - KONDO, M., KONDO M FAU - OHOKA, E. & OHOKA, E. 1989. Human respiratory airflow through an artificial nasal model: pressure/flow relationship. *Auris Nasus Larynx,* 16**,** 89-97.

NICOLET, J., POULARD, F., BANETON, D., RIGAL, J. C. & BLANLOEIL, Y. 2011. High-flow nasal oxygen for severe hypoxemia after cardiac surgery. *Annales Françaises d'Anesthèsie et de Rèanimation,* 30**,** 331-334.

PANTLE, I., HABERLAND, E. J., KNIPPING, S., KNOERGEN, M., STOCK, K. & NEUMANN, K. Applying Computational Fluid Dynamics Methods on Nasal Flow Investigations Based on a Real Domain Generated from CT Data. *In:* DÖSSEL, O. & SCHLEGEL, W., eds. World Congress on Medical Physics and Biomedical Engineering, September 7 - 12, 2009, Munich, Germany, 2010/01/01 2010. Springer Berlin Heidelberg, 797-800.

PARKE, R. L., ECCLESTON, M. L. & MCGUINNESS, S. P. 2011a. The effects of flow on airway pressure during nasal high-flow oxygen therapy. *Respiratory Care,* 56**,** 1151-1155.

PARKE, R. L., MCGUINNESS, S. P. & ECCLESTON, M. L. 2011b. A preliminary randomized controlled trial to assess effectiveness of nasal high-flow oxygen in intensive care patients. *Respiratory Care,* 56**,** 265-270.

PROETZ, A. W. 1953. Respiratory air currents and their clinical aspects. *The Journal of Laryngology and Otology,* 67**,** 1.

RELLO, J., PÉREZ, M., ROCA, O., POULAKOU, G., SOUTO, J., LABORDA, C., BALCELLS, J., SERRA, J. & MASCLANS, J. R. 2012. High-flow nasal therapy in adults with severe acute respiratory infection. *Journal of Critical Care,* 27**,** 434.

RITCHIE, J. E., WILLIAMS, A. B., GERARD, C. & HOCKEY, H. 2011. Evaluation of a humidified nasal high-flow oxygen system, using oxygraphy, capnography and measurement of upper airway pressures. *Anaesthesia and Intensive Care,* 39**,** 1103-1110.

RITTER, F. N. 1970. The vasculature of the nose. *Ann Otol Rhinol Laryngol,* 79**,** 468-474.

SASLOW, J. G., AGHAI, Z. H., NAKHLA, T. A., HART, J. J., LAWRYSH, R., STAHL, G. E. & PYON, K. H. 2006. Work of breathing using high-flow nasal cannula in preterm infants. *Journal of Perinatology,* 26**,** 476-480.

SCHRECK, S., SULLIVAN KJ FAU - HO, C. M., HO CM FAU - CHANG, H. K. & CHANG, H. K. 1993. Correlations between flow resistance and geometry in a model of the human nose. *Journal Applied Physiology,* 75**,** 1767-1775.

SHEPARD, J. W., JR. & BURGER, C. D. 1990. Nasal and oral flow-volume loops in normal subjects and patients with obstructive sleep apnea. *The American Review Respiratory Disease,* 142**,** 1288-93.

SHINNEEB, A. M. & POLLARD, A. 2012. Investigation of the flow physics in the human pharynx/larynx region. *Experiments in Fluids,* 53**,** 989-1003.

SHOEMAKER, M. T., PIERCE, M. R., YODER, B. A. & DIGERONIMO, R. J. 2007. High flow nasal cannula versus nasal CPAP for neonatal respiratory disease: a retrospective study. *Journal of Perinatology,* 27**,** 85-91.

SMITH, P. L., O'DONNELL, C. P., ALLAN, L. & SCHWARTZ, A. R. 2003. A physiologic comparison of nasal and oral positive airway pressure. *Chest,* 123**,** 689-694.

SPENCE, C. J. T., BUCHMANN, N. A. & JERMY, M. C. 2012. Unsteady flow in the nasal cavity with high flow therapy measured by stereoscopic PIV. *Experiments in Fluids,* 52**,** 569-579.

SPENCE, K. L., MURPHY, D., KILIAN, C., MCGONIGLE, R. & KILANI, R. A. 2007. High-flow nasal cannula as a device to provide continuous positive airway pressure in infants. *Journal of Perinatology,* 27**,** 772-775.

SPENTZAS, T., MINARIK, M., PATTERS, A. B., VINSON, B. & STIDHAM, G. 2009. Children with respiratory distress treated with high-flow nasal cannula. *Journal of Intensive Care Medicine,* 24**,** 323-328.

STRINGER, N. M., CATER, J. E., EATON-EVANS, J. & WHITE, C. 2010. Numerical Comparison of Air Flow Patterns in the Nasal Airways of Adults and Neonates. The University of Auckland, Auckland.

SWIFT, D. L. & PROCTOR, D. F. 1977. Access of air to the respiratory tract. *In:* BRIAN, J. D., PROCTOR, D. F. & REID, L. M. (eds.) *Respiratory Defense Mechanisms.* M. Dekker.

SZTRYMF, B., MESSIKA, J., BERTRAND, F., HUREL, D., LEON, R., DREYFUSS, D. & RICARD, J.-D. 2011. Beneficial effects of humidified high flow nasal oxygen in critical care patients: a prospective pilot study. *Intensive Care Medicine,* 37**,** 1780-1786.

TAN, J., HAN, D., WANG, J., LIU, T., WANG, T., ZANG, H., LI, Y. & WANG, X. 2012. Numerical simulation of normal nasal cavity airflow in Chinese adult: a computational flow dynamics model. *European archives of oto-rhino-laryngology,* 269**,** 881-889.

TAYLOR, D. J., DOORLY, D. J. & SCHROTER, R. C. 2010. Inflow boundary profile prescription for numerical simulation of nasal airflow. *Journal of the Royal Society Interface,* 7**,** 515-527.

TIRUVOIPATI, R., LEWIS, D., HAJI, K. & BOTHA, J. 2010. High-flow nasal oxygen vs high-flow face mask: A randomized crossover trial in extubated patients. *Journal of Critical Care,* 25**,** 463-468.

TOBIN, M. J., CHADHA, T. S., JENOURI, G., BIRCH, S. J., GAZEROGLU, H. B. & SACKNER, M. A. 1983. Breathing patterns. 1. Normal subjects. *Chest,* 84**,** 202-205.

TORTORA, G. J. & DERRICKSON, B. H. 2006. *Principles of anatomy and physiology,* Hoboken, NJ, J. Wiley.

TSILINGIRIS, P. T. 2008. Thermophysical and transport properties of humid air at temperature range between 0 and 100°C. *Energy Conversion and Management,* 49**,** 1098-1110.

VERIN, E., TARDIF, C., BUFFET, X., MARIE, J. P., LACOUME, Y., ANDRIEU-GUITRANCOURT, J. & PASQUIS, P. 2002. Comparison between anatomy and resistance of upper airway in normal subjects, snorers and OSAS patients. *Respiration Physiology,* 129**,** 335-343.

VERSTEEG, H. K. & HARGRAVE, G. K. Inhaled air and aerosol particle flow characteristics in a model of the human upper airway. 4th International Symposium on Particle Image Velocimetry, 2001.

WARD, J. J. 2013. High-flow oxygen administration by nasal cannula for adult and perinatal patients. *Respiratory Care,* 58**,** 98-120.

WAYMAN, E., ROSEN, M. & SEPPA, N. 2013. News in brief. *Science News,* 183**,** 20-20.

WEN, J., INTHAVONG, K., TIAN, Z. F., TU, J. Y., XUE, C. L. & LI, C. G. 2007. Airflow patterns in both sides of a realistic human nasal cavity for laminar and turbulent conditions. *16th Australasian Fluid Mechanics Conference.*

WIDMAIER, E. P., RAFF, H., STRANG, K. T. & VANDER, A. J. 2011. *Vander's human physiology: the mechanisms of body function,* New York, McGraw-Hill.

WILKINSON, D. J., ANDERSEN, C. C., SMITH, K. & HOLBERTON, J. 2007. Pharyngeal pressure with high-flow nasal cannulae in premature infants. *Journal of Perinatology,* 28**,** 42-47.